Title
Design and Fabrication of Nano-Bio Materials for Sensor and Device Applications

Author
Choi, Duyoung

Publication Date
2015

UNIVERSITY OF CALIFORNIA, SAN DIEGO

Design and Fabrication of Nano-Bio Materials for Sensor and Device Applications

A dissertation submitted in partial satisfaction of the
requirements for the degree Doctor of Philosophy

in

Materials Science and Engineering

by

Duyoung Choi

Committee in Charge:

Professor Sungho Jin, Chair
Professor Renkun Chen
Professor Ratneshwar Lal
Professor Vlado Lubarda
Professor Ying Shirley Meng

2015

The dissertation of Duyoung Choi is approved, and it is acceptable in quality and form for publication on microfilm:

Chair

University of California, San Diego

2015

DEDICATION

Dedicated to

my family

EPIGRAPH

“Seek first his kingdom and his righteousness, and all these things will be given to you as well.” (Matthew 6:33)

TABLE OF CONTENTS

LIST OF FIGURES

LIST OF TABLES

ACKNOWLEDGEMENTS

I really thank and praise God for helping and guidance me with your endless love, peace, and faithfulness.

I wish to acknowledge and deeply thank my advisor, Professor Sungho Jin for his steadfast encouragement, guidance, and support during the course of this research here at University of California, San Diego. I sincerely thank to my dissertation committee members for their precious time and helpful suggestions: Professor Renkun Chen, Professor Ratneshwar Lal, Professor Vlado Lubarda, and Professor Shirley Meng.

I wish to express my gratefulness to the JIN Group members for their numerous help, stimulating discussions, and invaluable contributions: Dr. Leon Chen, Dr. Seong Deok Kong, Dr. Hyunsu Kim, Dr. Young Oh, Dr. Chulmin Choi, Dr. Kyunbae Noh, Gary Johnston, Jeanne Khamwannah, Cihan Kuru, Justin Taekyoung Kim, Cyrus Rustomji, Calvin Gardener, Isaac Liu, Dong Won Chun, Alireza Kargar, Youngjin Kim, Elizabeth Caldwell, Gunwoo Kim, Erick Loran, Taewoo Kim, Serdar Yuvuz, Sarah Zhong, Dr. Kyungjun Hwang, and Prof. Jun-Hyun Han.

Finally, I wish to thank my family for their cares, supports, and sacrifices. I would also like to thank to the community members of the SDKUPC as one family in God for their love and dedication. Last but not least, I wish to express my infinite gratitude to my beloved wife, Jin Yu and my lovely kids, Yuna, Yunwoo and unborn baby. Their truly support and encouragement have been always fueled me up whenever I am tired, frustrated, and exhausted.

Chapter 2, in full, has been prepared for review publication in NANO written by Kunbae Noh, Karla Brammer, Tae-Yeon Seong, and Sungho Jin and in Nano Letters written by Seong Deok Kong, Weizhou Zhang, Jun Hee Lee, Karla Brammer, Ratnesh Lal, Michael Karin, and Sungho Jin

Chapter 3, in full, is a reprint of the material as it appears in Materials Research Letters, 2(3) 131-139 (2014) written by Duyoung Choi and Sungho Jin. The dissertation author was the primary investigator and author of this work.

Chapter 4, in full, is a reprint of the material as it was accepted in Small written by Duyoung Choi and Sungho Jin. The dissertation author was the primary investigator and author of this work.

Chapter 5, in full, is a reprint of the material as it appears in Journal of Nanoscience and Nanotechnology 15(3), 2464-2467 (2015) written by Cihan Kuru, Duyoung Choi, Chulmin Choi, Young Jin Kim, and Sungho Jin. The dissertation author was the primary investigator and author of this work.

Chapter 6, in full, has been submitted for publication, “Biodegradably Coated Magnetic Nanocapsules for On-Off Switchable Drug Release with Reduced Leakage”, by Duyoung Choi, Seong Deok Kong and Sungho Jin. The dissertation author was the primary investigator and author of this work.

VITA

1998 ~ 2003	B.S., Chemical Engineering, Inha University, Korea
2003 ~ 2005	M.S., Chemical Engineering, Inha University, Korea
2005 ~ 2008	Military Service (R.O.K. Army), Korea
2009 ~ 2015	Ph.D., Materials Science and Engineering, University of California, San Diego, U.S.A.

PUBLICATIONS

Journals Articles:

1. Cihan Kuru, Chulmin Choi, Alireza Kargar, **Duyoung Choi**, and Sungho Jin, “MoS2 nanosheet-Pd nanoparticle composite for highly sensitive room temperature detection of hydrogen”, accepted in press *Advanced Science* (2015).
2. **Duyoung Choi**, Cihan Kuru, Sungho Jin, Uniformly Nano-Patterned Graphene Field Effect Transistors with Enhanced Properties”, submitted to *Scientific Reports* (2014).
3. Cihan Kuru, Serdar Yavuz, Alireza Kargar, Chulmin Choi, **Duyoung Choi** and Sunhgo Jin, "Highly stable graphene/silicon heterojunction solar cells by NiO doping", submitted to *Nanoscale* (2014).
4. **Duyoung Choi** and Sungho Jin, “Unusually High Optical Transparency in Hexagonal Nano-Patterned Graphene with Enhanced Conductivity by Chemical Doping”, accepted to *Small* (2014).
5. **Duyoung Choi**, Cihan Kuru, Serdar Yavuz, Sungho Jin, "Fabrication and characterization of 3D graphene composited metal oxide for energy storage device", accepted to *SPIE NanoScience and Engineering* (2014)
6. **Duyoung Choi**, Seong Deok Kong and Sungho Jin, "Biodegradably Coated Magnetic Nanocapsules for On-Off Switchable Drug Release with Reduced Leakage”, submitted to *J. of Controlled Release* (2014).
7. Cihan Kuru, **Duyoung Choi**, Chulmin Choi, Serdar Yavuz, Sungho Jin, "Scalable nano-patterning of graphene by employing dewetted nickel thin film nano-bridges" accepted in press *Journal of Materials Science* (2014).
8. **Du Young Choi** and Sungho Jin, **“**Nano Patterned Graphene Field Effect Transistor Fabricated using Block Copolymer Lithography”, *Materials Research Letters*, **2**(3) 131-139 (2014).
9. Cihan Kuru, **Duyoung Choi,** Chulmin Choi, Young Jin Kim, and Sungho Jin, “Palladium Decorated Graphene-Nanoribbon Network for Enhanced Gas Sensing”, *J. Nanosci. Nanotechnol.* 15(3), 2464-2467 (2015).
10. Chulmin Choi, Soonkook Hong, Li-Han Chen, Chin-Hung Liu, **Duyoung Choi**, Cihan Kuru and Sungho Jin, "Deformation and electrical properties of magnetic and vertically conductive composite with chain-of-spheres structure”, *Electronic Materials Letters*, **10**(3) 585-589 (2014).
11. Chulmin Choi, Kunbae Noh, **Duyoung Choi**, Jirapon Khamwannah, Chin-Hung Liu, Daehoon Hong, Li-han Chen, and Sungho Jin “Geometrically Planar Ion-Implant Patterned Magnetic Recording Media Using Block Copolymer Aided Gold Nanoisland Masks”, *IEEE Transactions on Magnetics*, **48**(11), 3402-3405 (2012).
12. Long Mei Jin, **Du Young Choi**, Haiyan Liu and Kyung Ho Row, “Protein Binding Study of S-ibuprofen Using High-performance Frontal Analysis”, *The Bulletin of the Korean Chemical Society*, **26**(1), 1-5 (2005).
13. **Du Young Choi**, and Kyung Ho Row, “Estimation of Kinetic and Rate Parameters of Peptides by Moment Analysis”, *J. Ind. Eng. Chem.*, **10**(6), 1052-1057 (2004).
14. **Du Young Choi** and Kyung Ho Row “Whey Proteins, Anion-Exchange Separation” Encyclopedia of Chromatography, Marcel Dekker, Inc. (2003).

Patents / Technology disclosures:

1. **D.Y. Choi**, and K.H. Row, "Method for Extracting Glabridin from Licorice Root", Korea patent No. 10-0570803-0000 (2006).
2. **D.Y. Choi**, W.Y. Do, K.J. Lee and K.H. Row, "Method for Extracting Isoflavone from Soy Bean", Korea patent No. 10-0475129-0000 (2005).

Conference proceedings:

1. **Duyoung Choi**, Cihan Kuru, Serdar Yavuz, Sungho Jin, "Fabrication and characterization of 3D graphene composited metal oxide for energy storage device", accepted to SPIE NanoScience and Engineering (2014)
2. **Duyoung Choi**, and Sungho Jin, "Anodic Aluminum Oxide Guided Patterning of Graphene with Ni Islands", Intermag 2012.
3. **Duyoung Choi**, and Sungho Jin, "Di-block Copolymer Guided Patterning of Graphene", EIPBN 2012.

ABSTRACT OF THE DISSERTATION

Design and Fabrication of Nano-Bio Materials for Sensor and Device Applications

by

Duyoung Choi

Doctor of Philosophy in Materials Science and Engineering

University of California, San Diego, 2015

Professor Sungho Jin, Chair

In this thesis, various aspects of nano-bio materials have been discussed including novel design, fabrication and applications of nanopatterned graphene for sensor and device by using self-assembly techniques.

First, we demonstrate a successful fabrication of nano-patterned graphene (NPG) using a Poly(styrene-*b*-4-vinylpyridine) (PS-*b*-P4VP) polymer, which was never used previously for the graphene patterning. This work also demonstrates that block copolymer (BCP) lithography is a pathway for low-cost, high throughput large scale production of NPG with critical dimensions down to nanometer regime.

Second, Thin anodized aluminum oxide nano-mask was prepared by facile self-assembly technique without using polymer buffer layer, which was utilized as direct-contact template for oxygen plasma etch to produce near periodic, small-neck-width NPG. This work also demonstrates that our direct-contact, self-assembled mask lithography is a pathway for low-cost, high throughput, large scale nanomanufacturing of graphene nano devices.

Third, we demonstrate here a successful fabrication of optically highly transparent (~98%) graphene layer having a reasonable electrical conductivity by nano-patterning and doping. AAO nanomask prepared by simple self-assembly technique was utilized to produce an essentially hexagonally NPG. The results indicate that the NPG approach can be a promising route for simultaneously tuning the optical and electrical properties of graphene to make it more light-transmissible and suitable as a flexible transparent conductor.

Fourth, the fabrication of large-scale graphene-nanoribbon (GNR) network and its application for gas sensing are reported. GNR network shows significantly enhanced sensitivity to ammonia gas compared to pristine graphene. The detection sensitivity of the nanoscale GNR network is even further improved by decorating GNR network with palladium (Pd) nanoparticles, which shows a relative resistance response of 65 % to 50 ppm of ammonia in nitrogen at room temperature as well as good reversibility in air.

Fifth, we have successfully prepared PLGA-coated nanocapsules that allow a switchable drug release on remote RF magnetic field actuation, and are capable of tumor penetration with their powerful magnetic vector. The biodegradable PLGA-polymer-coating on the nanocapsule surface intentionally delays the diffusional leakage of the therapeutic drugs through the nanopores in the wall of the hollow capsules that contain the magnetic nanoparticles and the desired therapeutic drugs.

CHAPTER 1: Introduction

Several properties of graphene make it a promising candidate for use as an electrode. Besides their good conductivity, it also has high surface to mass ratio. Monolayer graphene possesses high crystallographic quality and ballistic electron transport on the micrometer scale with only 2.3% of light absorption.[1] Graphene is also emerging as a potential candidate in photo-voltaic applications as transparent electrodes[2] due to its high transparency (~ 97.7 % for monolayer) and relatively low sheet resistance (~ few hundred Ω/*sq*).[1] Graphene has shown its potentiality to be essential part of much future electronic circuits and devices utilizing high frequency and logic transistors and switches[3] Its structural and electrical properties make it an attractive material as the valence and conduction bands are separated by zero band gaps. The zero band-gap features of graphene and its property to exhibit large electric field effect allows doping with electrons or holes through electrostatic gating.[4] Theoretical investigations predict that the high saturation velocity of graphene can be as high as twice of GaAs and four times that of Si. As the size of the device shrinks to nanometer scale, saturated carrier velocity becomes a more significant measure of the transport properties.[5] Therefore, graphene can be an outstanding alternative to the miniaturization of electronic systems and devices[5] The gas sensing mechanism of graphene is attributed to the adsorption and desorption of gas molecules, acting as donors and acceptors, on the surface[6] Graphene is a better candidate for the electrically based sensor for mainly two reasons. In one hand, its two dimensional structure with one atom thickness allows a full exposure of all atoms for obtaining better adsorption of gas molecules[7, 8] On the other hand, it does not require high impedance and other special circuits to reduce the noise signal because of its high crystal quality and low resistance (typically few hundred ohms).[8]

In this thesis work, we have developed novel nanofabrication techniques for graphene nanostructure using self-assembled AAO and block copolymer (BCP). Various applications including flexible transparent conductor, field effect transistor and chemical-bio sensing devices have been investigated.

Chapter 1 gives a brief introduction on graphene and nanopatterned graphene.

Chapter 2 gives broad background on graphene synthesis, properties and its applications including flexible transparent conductor, field effect transistor and sensor.

Chapter 3 demonstrates fabrication and properties nanopatterned graphene by self-assembled template for transistor application.

Chapter 4 contains high optical transparency in hexagonal nano-patterned graphene with enhanced conductivity by chemical doping

Chapter 5 demonstrates novel graphene nanostructure network for bio and chemical sensor.

Chapter 6 gives biodegradably coated magnetic nanocapsules for on-off switchable drug release with reduced leakage

Chapter 7 gives a summary of the research results achieved, discusses the ongoing research, and makes suggestions as to what additional advances need to be made in the future.

CHAPTER 2: Background

2.1 Graphene

Graphene, since the demonstration of its easy isolation by the exfoliation of graphite in 2004 by Novoselov, Geim and co-workers, has been attracting enormous attention in the scientific community. Graphene has gained a great amount of attention recently for its electrical, physical, and chemical properties. Primarily driving this interest is graphene's potential for replacing silicon in electronic devices, which increasingly incorporate nanotechnology-enhanced advances. As reported by Geim's group in 2004, the carrier density in graphene can be controlled by the simple application of gate voltage. This effect can be used to tune the concentration and mobility of charge carriers in graphene based electronic devices.[4] As electronic and optoelectronic device dimensions shrink to atomic scales, material limitations become the impediment to further improvements in device performance; a narrow graphene strip with the length of only few nanometers has been successfully tested for the transportation of charge carriers.[9] Therefore, alternative materials such as graphene become candidates for incorporation into future electronic devices. Graphene is also being investigated as a possible replacement for transparent conducting oxides, which have applications in touch-screen devices and solar cells.

2.1.1 Graphene synthesis and properties

The pristine graphene has very low concentration of structural defects, which makes it interesting for fundamental studies. However, the flake thickness, size and location are largely uncontrollable. Several strategies are presently being pursued to achieve reproducible and scalable graphene on substrates. One example is covalent or non-covalent exfoliation of graphite in liquids.[10] A widely used technique to synthesize graphene is the thermal decomposition of hexagonal α-SiC (6H-SiC and 4H-SiC). It has the advantage that it is very clean because the epitaxially matching support crystal provides the carbon itself and no metal is involved. High quality wafer scale graphene with switching speeds of up to 100GHz[10] has been demonstrated using this technique. By far the most common route to synthesize graphene is chemical vapor deposition (CVD). There are many CVD variations. It is the most promising, inexpensive and readily accessible approach for deposition of reasonably high quality graphene. Thermal CVD is commonly applied to graphene formation over transition metals, including copper[11], nickel[12, 13], and iridium.[14] In particular, recent developments on uniform single layer deposition of graphene on copper foils over large areas have allowed access to high quality material. Large area graphene synthesis using Cu catalyst has received widespread attention since it was first reported in 2009.[15] Thermal CVD techniques can also be used for graphene synthesis over dielectrics, namely, sapphire [16] and various other oxides.[17, 18] Free-standing carbon nanosheets and planar graphite films with a few graphene layers have been successfully synthesized by plasma enhanced CVD (PECVD)[17, 18]. In this section, Cu catalysts were used for the deposition of graphene by CVD method. In what follows, we will describe our approach for the synthesis and properties of graphene on copper substrate by CVD method.

2.1.1.1 Synthesis and transfer

In CVD process, carbon-bearing gaseous species react at high temperatures (850- 1100 ℃) in the presence of metal catalysts, serving in the decomposition of the carbon species and in the nucleation of the graphene lattice. The mechanism of graphene growth on metals is presumably influenced by several factors, including the carbon solubility limit in the metal, its crystal structure, lattice parameters and thermodynamic parameters such as the temperature and pressure of the system. Compared to other metal substrate, copper has received widespread attention mainly due to three reasons: It has very low solubility with carbon; if the copper film is annealed to around its melting temperature, it experiences grain size growth needed for the achievement of large uniform graphene domains; It is more flexible in a foil of low thickness which can be used for the deposition of graphene with roll-to-roll technology.[19]

CVD graphene using Cu as a transition metal substrate for single layer graphene synthesis was first demonstrated by Rouff's group in 2009.[20] Graphene was synthesized using thermal chemical vapor deposition (CVD) of methane (CH_4) at 1000 ℃. A thin Cu foil (25 μm thickness) was purchased from Alfa-Aesar, USA and cut in 20 mm × 13 mm size and annealed at 1000 ℃ for 1 h in an inert gas atmosphere followed by hot acid treatment and cleaning. This step was necessary for the removal of any oxide layer on the copper substrate. After that the metal foil was placed inside a thermal CVD system which consists of a quartz tube furnace of 8 inch diameter placed into a furnace as shown in Figure 2.1, and the temperature was increased up to 1000 ℃ with a heating rate of 120 ℃ min^{-1}. This step is necessary for the removal of any native oxide layer left on the surface after the heat treatment with acetic acid. The atmosphere of the CVD furnace was maintained at 0.8 atmospheric pressure in the presence of an inert gas (Ar) and $CH_4 : H_2$ (1 : 4) was used as a precursor gas mixture for graphene growth. The gas composition was changed to hydrogen and argon immediately after the coating process was completed and the system was allowed to return to the room temperature. Figure 2.2 illustrates the proposed growth mechanism of graphene on Cu. The annealing at high temperature in H_2 environment is to remove the native oxide layer on the Cu surface, while Cu grains will also develop. With the exposure of Cu foil in CH_4/H_2 environment, nucleation of graphene islands start taking place randomly but preferentially at the grain boundary of Cu surface. As the exposure to CH_4 continues, the graphene domains grow in size to cover the whole area of Cu substrates and eventually aggregate into a continuous graphene film.

Compared to other metal substrate, copper has received widespread attention mainly due to three reasons: It has very low solubility with carbon; if the copper film is annealed to around its melting temperature, it experiences grain size growth needed for the achievement of large uniform graphene domains; It is more flexible in a foil of low thickness which can be used for the deposition of graphene with roll-to-roll technology.[19] In this research, Cu catalysts were used for the deposition of graphene by CVD method. In what follows, we will describe our approach for the synthesis of graphene on copper substrate by CVD method and transfer to the desired substrate. Cu is another transition metal that acts as a catalyst to deposit graphene on its surface by the surface adsorption mechanism rather than by segregation or precipitation like Ni.

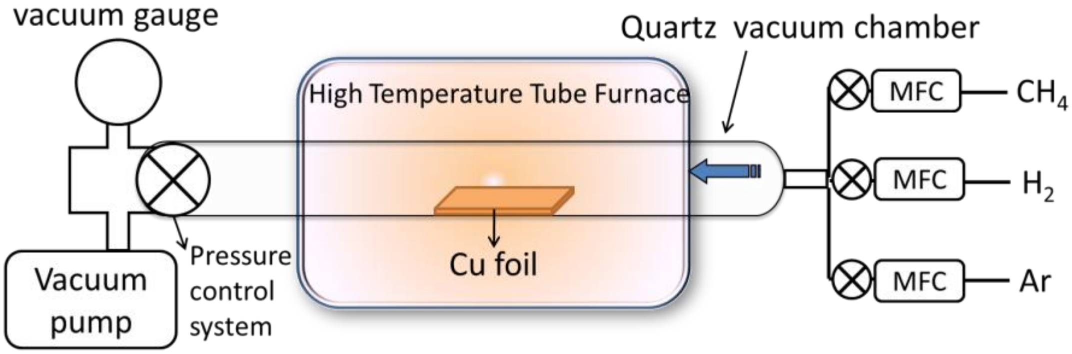

Figure 2.1: Schematic of a common setup for chemical vapor deposition of graphene.

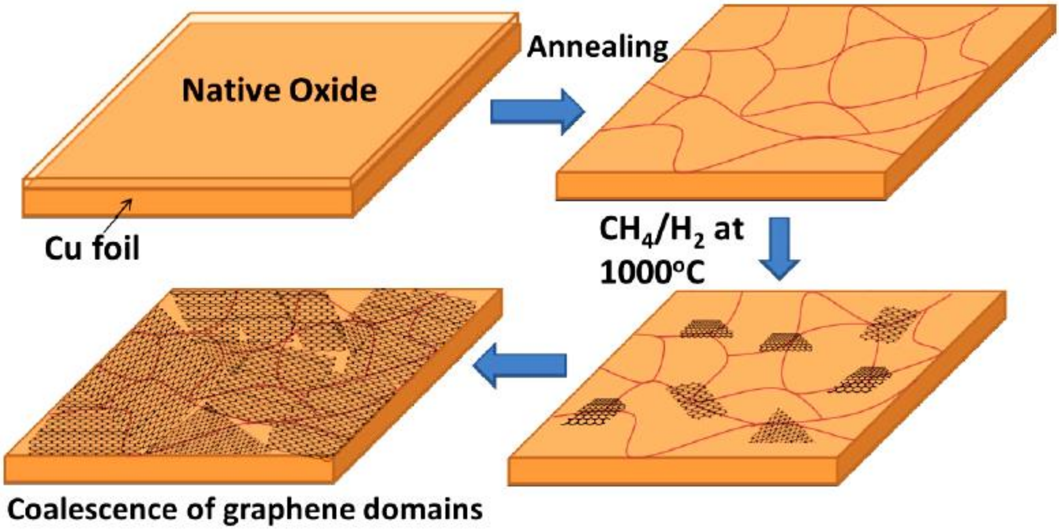

Figure 2.2: Schematic illustrating the proposed growth mechanism of graphene on Cu substrates by CVD: (a) copper foil with native oxide; (b) Native Cu oxide is reduced while Cu develops grains on the surface after annealing at high temperature in H_2 environment; c) The exposure of the Cu foil to CH_4/H_2 atmosphere at 1000 °C leading to the nucleation of graphene islands; (d) enlargement of the graphene flakes and coalescence of graphene domains with different lattice orientation.[20]

Ruoff and co-workers first reported the precipitation of graphene on a Cu surface at high temperature by the surface catalyzed process associated with the limited solubility of carbon in copper[15, 20] showed that by carbon isotope labeling, one can compare the graphene growth mechanism on Cu and Ni. Therefore, the graphene precipitation mechanism on a Cu surface differs from the Ni surface where deposition occurs due to the carbon segregation process or precipitation mechanism.

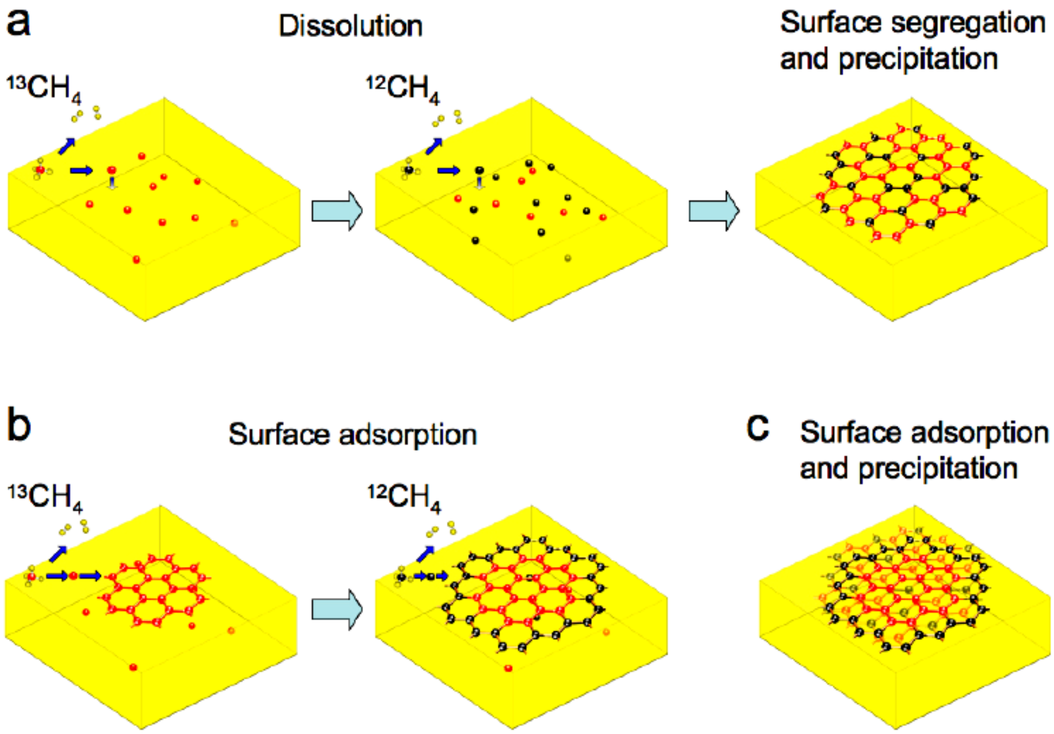

Figure 2.3: (a) Graphene formation mechanism by surface segregation and precipitation and (b) mechanism of surface adsorption as reported by Ruoff et al.[15, 20]

Li et al.(2009) proposed the mechanism shown in Figure 2.3, which illustrates the two-step process of graphene formation: (1) segregation and precipitation and (2) surface adsorption or surface-mediated growth. Figure 2.3 illustrates the step-by-step formation of graphene layers by the segregation process on a Ni substrate that consists of (1) the decomposition of CH_4 in the presence of hydrogen at elevated temperatures, (2) dissolution of carbon atoms in a metal matrix, (3) segregation of carbon atoms on a metal surface, and (4) precipitation during the cooling process. They also explained the mechanism of surface-mediated graphene growth on Cu as shown in Figure 2.3, which consists of the following steps: (1) carbon formation from methane decomposition, (2) surface nucleation and growth, (3) further spraying of nuclei throughout the entire surface, and (4) domain formation. As the surface is fully covered with graphene, the growth process terminates, which is described as the self-limiting process of graphene growth on a Cu surface.

Graphene grown on transition metals must be transferred onto insulating substrates for device fabrication and electronic characterization.[15, 21] Different methods have been demonstrated to transfer the as-grown graphene on metal substrates onto desired insulating substrates, such as polymeric foils (polyethylene terephthalate (PET)), glass and SiO_2/Si. A general transfer technique of CVD-graphene onto a target substrate is illustrated in Figure 2.4. Typically, the transfer is first conducted by spin-coating a thin polymeric layer, such as poly(methylmethacrylate) (PMMA) on top of the as-grown graphene. This polymer provides a supportive framework for graphene before the transfer. Before graphene on Cu was transferred to substrate, the back side graphene was removed by oxygen plasma. The underneath Cu substrate is then etch away by ammonium persulfate ($(NH_4)_2SO_8$) solution. After the Cu is completely dissolved, the floating membrane can be scooped and placed on a desired substrate. After that, the PMMA layer was removed by dissolving it in acetone. Furthermore, the rapid thermal annealing was carried out for graphene on the Si/SiO_2 substrate at 400 ℃ under a N_2 atmosphere to remove the residual PMMA and promote the adhesion between graphene and the oxide layer.

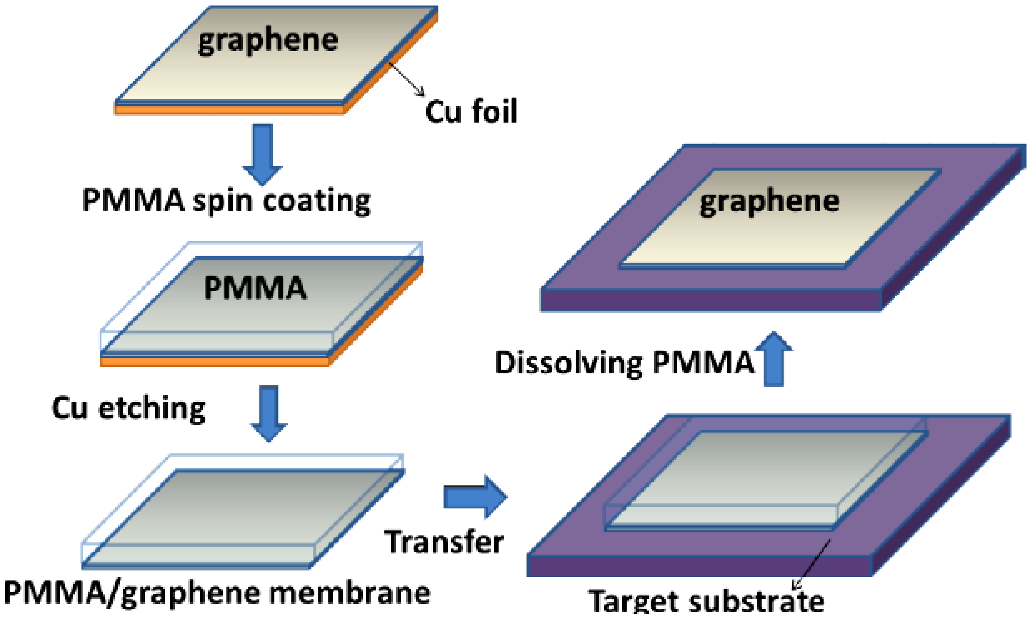

Figure 2.4: A cartoon showing the transfer process of graphene grown on Cu foil onto a target substrate.

2.1.1.2 Electronic properties of graphene

The carbon atoms in the structure of graphene are arranged in a hexagonal closed pack structure due to the sp^2 hybridization. The primitive cell of graphene is composed of two non-equivalent atoms, A and B, and these two sublattices are translated from each other by a carbon–carbon distance of 1.42 Å. Figure 1.2(a) shows the typical structure of honeycomb lattice. As labeled in Figure 2.5(a), the lattice point A has three nearest neighbors in north-east, north-west and south. Whereas, the lattice point B has three nearest neighbor in north, south-west and south-east. However, the lattices A and B together form a triangular Bravais lattices as the orientation of other lattice (AB) are equivalent. Therefore, lattice points A and B are called sub-lattices of the triangular Bravais lattice. A single carbon atom has four valence electrons with a ground-state electronic shell configuration of [He] $2s^2$ $2p^2$. In the case of graphene, the carbon–carbon chemical bonds are due to hybridized orbitals generated by the superposition of 2s with $2p_x$ and $2p_y$ orbitals. These are covalently bonded with the other atom with sigma bonding ($\sigma - bond$), and they are responsible for most of the binding energy and for the elastic properties of the graphene sheet. The lattice of this type is called a honeycomb lattice.[9] In sp^2 hybridization, the 2s state mixes with two of the 2p orbitals to form three different quantum mechanical states, called orbitals. These orbitals are oriented in the XY - plane with an angle of 120 degree.[22] The honeycomb lattice is not a Bravais lattice as the two neighboring atoms are not equivalent in position and orientation. The shaded region represents the first Brillouin zone (BZ), with its center Γ (Gamma point) and two inequivalent corners (K and K' points). Thicker lines are represented to avoid double counting. Therefore, the first Brillouin zone represents the shaded region with the thicker lines. For completeness, we have also shown the three inequivalent crystallographic points M, M' and M". The remaining free $2p_z$ orbitals present π symmetry orientation which has a weakly bonded electron with pi bonding ($\pi - bond$), and the overlap of these orbital states between neighboring atoms plays a major role in the electronic properties of graphene. For this reason, a good approximation for describing the electronic structure of graphene is to adopt an orthogonal nearest-neighbor tight-binding approximation assuming that its electronic states can be simply represented by a linear combination of $2p_z$ orbitals. Solving the Schrödinger equation, which reduces into a matrix secular expression, one can obtain the energy dispersion relation of π (bonding) and π* (antibonding) bands.[23]

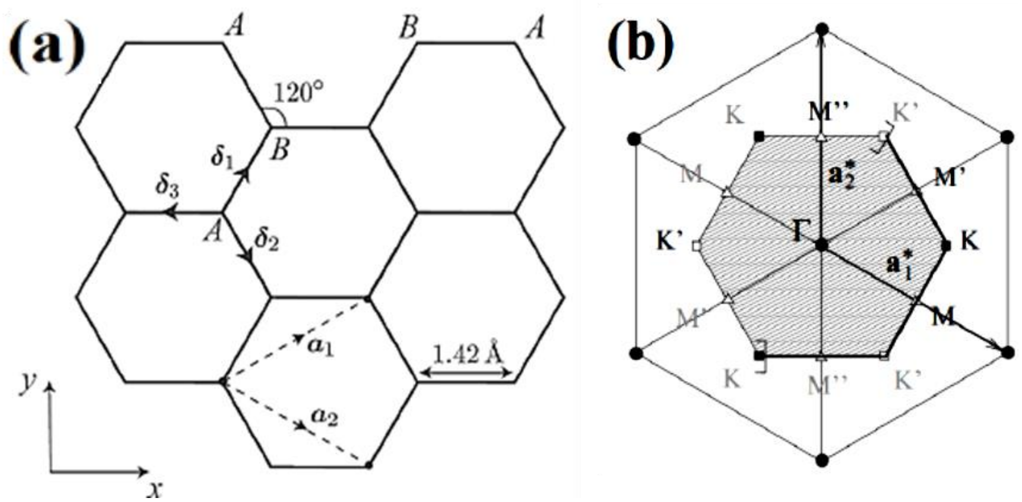

Figure 2.5: (a) Honeycomb lattice. The directions $\boldsymbol{\delta_1}$, $\boldsymbol{\delta_2}$ and $\boldsymbol{\delta_3}$ are the vectors connecting nearest sub-lattices B from sub-lattice A. The vectors $\boldsymbol{a_1}$ and $\boldsymbol{a_2}$ are the basis vectors for triangular Bravais lattice. (b) Reciprocal lattice of the triangular lattice. Its primitive lattice vectors are $\boldsymbol{a_1^*}$ and $\boldsymbol{a_2^*}$. Figure extracted from Ref. [23].

Electronic band structure can be explained by the reciprocal lattice of the triangular lattice as shown in Figure 2.5 (b). The electronic structure of graphene can also be represented by closed-form expression obtained analytically for the single-electron propagators written on a real-space basis.[24] Graphene valence and conduction bands are degenerate at 6 points located on the corners of the Brillouin zone, which form two inequivalent groups of K points, called K and K′. These points K and K′ are called Dirac points. Graphene is a zero-gap semiconductor because the conduction and valence band meet at the Dirac point. The Dirac points are locations on the edge of Brillouin zone in momentum space. Each set is not equivalent with other set of three. As reported by Wallace and Co-Workers, the wave function of graphene is a linear combination of Bloch functions of sub lattice A.[11] An equivalent function can be defined for sub lattice B. If we consider nearest neighbor interaction only, the energy Eigen values can be obtained as[22, 23]

$$E\left(k_x, k_y\right) = \pm\gamma_0\left[1 + 4\cos\frac{\sqrt{3}k_x a}{2}\cos\frac{k_y a}{2} + 4\cos^2\frac{k_y a}{2}\right]^{1/2} \tag{2-1}$$

Here, γ_0 is the transfer integral between nearest neighbor. k_x and k_y are the wave vectors in X- and Y- planes. The energy dispersion of two dimensional structure is shown in Figure 2.6, where E is plotted as a function of wave vector k_x and k_y.

The upper half of the curve is called π* band while the lower half is called π band. The two bands degenerate at K and K′. At these points, the dispersion of energy vanishes. This is also called the Fermi Energy level in intrinsic graphene. The region of Dirac points is of primary interest in studying electronic properties of graphene. In the regions near the Dirac points, we can see a linear dispersion relation. The linear dispersion relation can be seen within about 1 eV of the Dirac energy, makes the Fermions in graphene behave as massless photons or neutrinos. The existence of massless Dirac Fermions has made the study of graphene so exciting. The other important outcome of the tight-binding approximation is that the Dirac Hamiltonian can be used to describe the system rather than Schrodinger equations. The low-energy dispersion near the valleys exhibits a circular conical shape, as displayed in the inset of Figure 2.6, unlike the quadratic energy–momentum relation obeyed by electrons at the band edges in conventional semiconductors. Comparing this linear energy relation of graphene with the dispersion of massless relativistic particles obtained from the Dirac equation, one can see that graphene charge carriers can behave as Dirac fermions with an effective Fermi velocity that is around 300 times smaller than the speed of light.[4] This makes graphene a reliable system to study quantum electrodynamic phenomena, an area of investigation previously limited to particle physics and cosmology investigations.

In this sense, several research groups have already addressed a variety of unusual phenomena that are revealed by graphene materials, which are characteristic of Dirac relativistic particles, for instance, the absence of localization effects even when disorder elements can take place[1, 4], robust metallic conductivity even in the limit of nominally zero carrier concentration, and the half-integer quantum Hall effect.

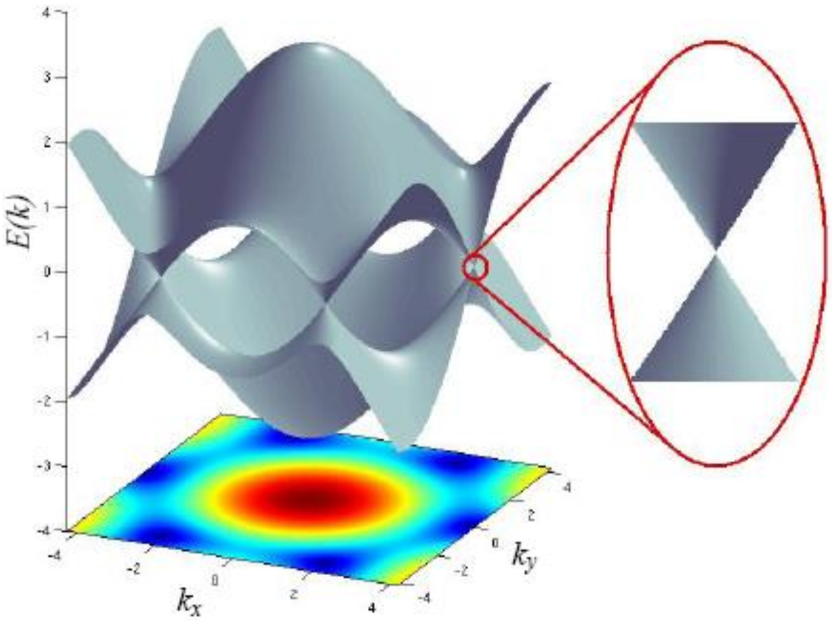

Figure 2.6: Energy dispersion relation for graphene drawn in the entire region of the Brillouin zone. Left: energy spectrum (in units of t) for finite values of t and t', with *t* = 2.7 eV and *t'* = -0.2t. Right: zoom in of the energy bands close to one of the Dirac points. Figure extracted from Ref.[22].

The amazing electronic properties of graphene have greatly motivated the scientific community to pursue a better understanding of their main physical features with the bonus of converting them into real technological applications. However, the absence of an energy band gap greatly restricts its use on digital devices. Thus, alternative strategies capable of inducing a band gap in graphene are being sought.

Several strategies have already been successfully adopted to modify the electronic structure of graphene and include chemical doping, interaction with substrates, and the application of mechanical forces or external electric/magnetic fields. Stacked graphene layers in the form of bilayers or graphite structures[25-27] also offer a promising route for band gap manipulation. Advanced lithographic techniques employed to tailor wide graphene samples into nanoscale structures have shown that lateral confinement of charge carriers can work as an efficient energy gap–tuning parameter. Such narrow graphene structures are known as graphene nanoribbons (GNR) and it has been demonstrated that their energy gap scales inversely with the width. The following section is dedicated to a review of the main physical properties of such confined graphene systems.

2.1.2 Graphene nanoribbons

Two-dimensional (2D) graphene sheets are nearly metallic, while ultrathin graphene nanoribbons (GNRs) can show semiconducting properties with the energy bandgap scaling inversely with the ribbon width.[28] The achievable energy bandgap, superior transport properties, and the planar manufacturability establish GNRs as promising cornerstones for the ‘beyond Si CMOS’ technology.[29] Although sub-10 nm GNRs have been demonstrated by chemical approaches[30, 31] the ability to form GNRs lithographically is important for the fabrication compatibility with the conventional planar integrated circuit (IC) manufacturing technology.

Besides the idealizations of graphene like 2D membranes, atomistic models of thin graphene strips were also addressed primarily to investigate the nature of edge dislocations and the appearance of defective dangling bonds in carbon networks.[32]

Such narrow graphene strips, known as graphene nanoribbons, were also not expected to exist in nature. The discovery that graphene materials can be fabricated in the free state and combined with modern lithography techniques has confirmed that confined graphene structures are experimentally feasible. Currently, the synthesis of graphene nanoribbon samples has advanced considerably beyond that possible with conventional lithographic methods. For instance, “ribbons” with widths smaller than 10 nm have been synthesized via crystallographic etching.[32, 33] An original fabrication process for graphene nanoribbons with atomic-scale precision has recently been realized through the controlled assembly of molecular precursors consisting of polycyclic aromatic hydrocarbon compounds.[34]

The physical properties of graphene nanoribbons are highly dependent on their width and the topology of the edge structures. There are two canonical types of graphene edges, referred to as armchair (AGNR) and zigzag (ZGNR) ribbons, and examples of their atomic structure can be seen in Figure 2.7. The atoms located on the edges are highlighted in green and W denotes the width of the ribbon. The width of an armchair ribbon can be defined in terms of the number of dimer lines: $W_a = (N_a - 1)a/2$ for armchair ribbons and $W_z = (N_z - 1)\sqrt{3a}/2$ for zigzag ribbons; N_a and N_z are their respective number of carbon chains.

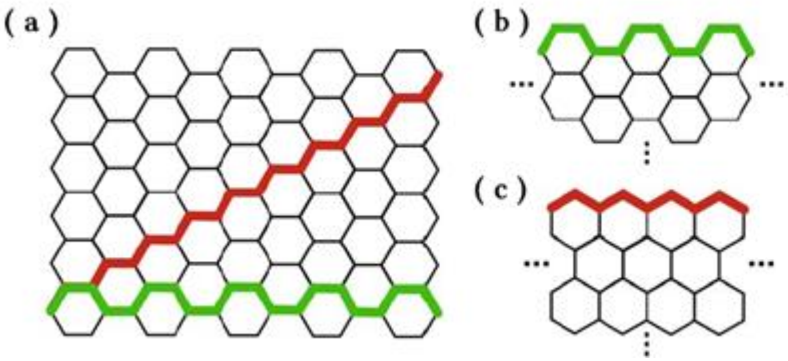

Figure 2.7: Honeycomb lattice of Graphene (a). Atomic structure of an (b) armchair- and a (z) zigzag- edge graphene nanoribbon. Green color atoms delineate the respective edge-shape and W denotes the width of the ribbon.[34]

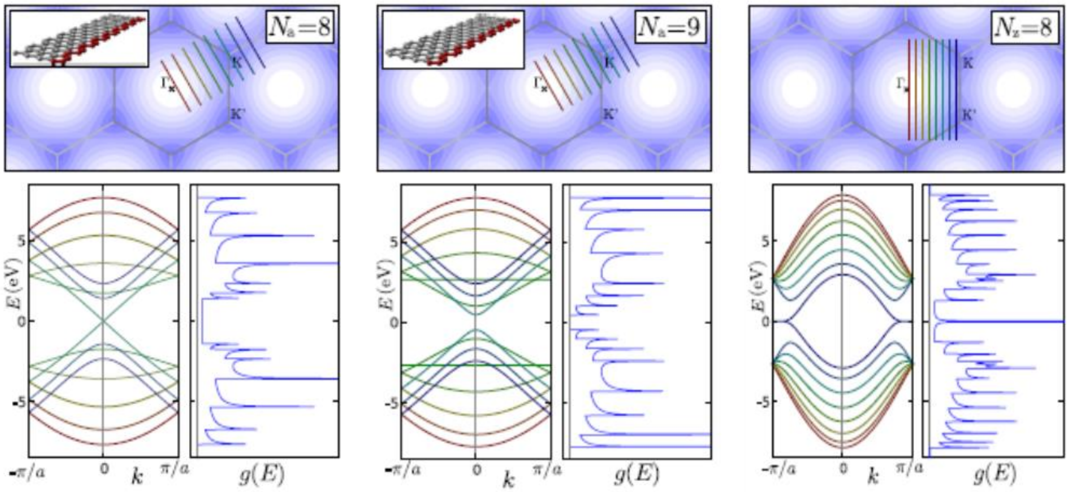

Figure 2.7: (Top panels) Zone-folding diagram for three different graphene nanoribbons: left, AGNR(8); middle, AGNR(9); and right, ZGNR(8). The parallel lines in the Brillouin zone represent the allowed quantized states of the ribbon projected in momentum space. Their respective energy band structures and density of states curves are displayed on the lower panels. (Adapted from N. Nemec, Quantum transport in carbon-based nanostructures.[34]

2.1.2.1 Quantum confinement in graphene nanoribbons

The band structure of armchair graphene nanoribbons can be derived if we consider that the electron wave vector in the y direction is quantized by hard-wall boundary conditions to be $k_y = n\pi/3W$ (n = ±1, ±2, ±4, ±5…)[35, 36] and the energy dispersion relation at low k values for the nth sub-band becomes

$$\varepsilon(k_x,n) = h\vartheta_F\sqrt{k_x^2 + \left(\frac{n\pi}{3W}\right)^2} \tag{2-2}$$

indicating that the conduction band (n > 0) and valence band (n < 0) split into a number of 1D sub-bands. The DOS for the nth sub-band is given by

$$\rho_{GNR} = \frac{2}{\pi\hbar\vartheta_F}\frac{\varepsilon}{\sqrt{\varepsilon^2-\varepsilon_n^2}} \tag{2-3}$$

Where

$$\varepsilon_n = \frac{n\pi\vartheta_F}{3W} = nE_G/2 \tag{2-4}$$

Adding this up for all sub-band leads to the total DOS, which can be used to calculate the carrier concentration; $n = \int_0^\infty \rho(E)f(E)dE$

$$n = \frac{2kT}{\pi\hbar\vartheta_F}\sum_n \int_{\varepsilon_n/kT}^{\infty} \frac{u}{\sqrt{u^2-(\varepsilon_n/kT)^2}}\frac{du}{1+e^{u-E_F/kT}} \tag{2-5}$$

Figure 2.9 is the plot of the 2D carrier concentration ($n_{2D} = n_{1D}/W$) for several ribbon widths on room temperature. The contribution of the individual sub-bands can be observed for the 2 nm ribbon. Though narrow GNRs exhibit large charge modulation due to the existence of a gap, they become similar to 2D graphene sheets when the Fermi level is deep inside the bands. As the width increases the intrinsic carrier concentration quickly increases to the value seen in 2D graphene. It implies that in a 2 nm GNR FET with perfect ohmic contacts many orders of magnitude room temperature current modulation can be achieved[36], but in a 10 nm GNR FET this modulation drops to the around 100x theoretical maximum already.

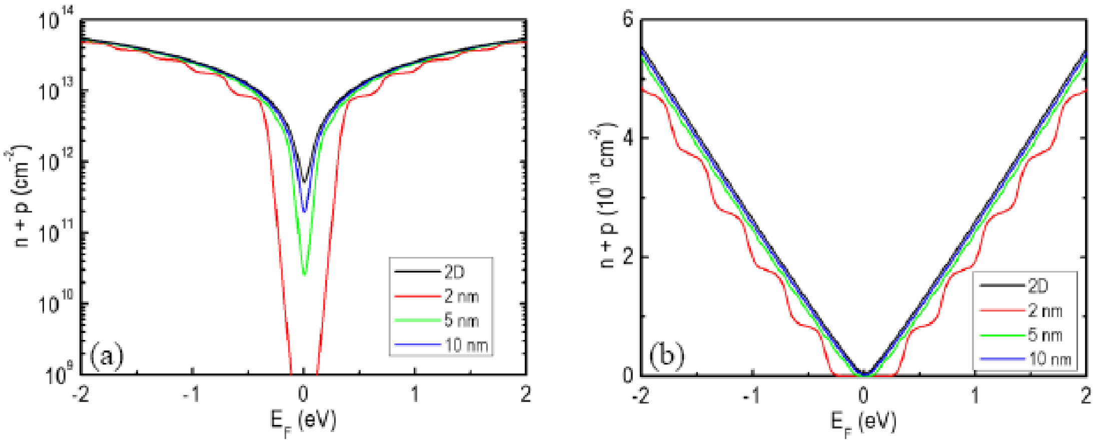

Figure 2.9: The carrier concentration of GNRs with various widths as a function of the channel potential at room temperature in logarithmic (left) and in linear (right) scale.

The sub-band separation (Eq. (2-4)) defines the bandgap of a GNR too. Consequently the bandgap as the function of the GNR width is

$$E_G = \frac{2\pi\hbar\vartheta_F}{3W} \cong \frac{1.38\ \text{eV}}{W(\text{nm})} \tag{2-6}$$

As indicated earlier, to have a lithographically designable parameter (*W*) with strong influence on the bandgap is very important from a device physics standpoint. It is not only allows us to fabricate graphene based digital switches or offers tremendous potential in optical applications, but also creates a completely new paradigm in bandgap engineering. This in-plane or lateral band-gap engineering means that device parameters such as on/off ratio or switching speed can be tailored within a chip without integrating different materials. FETs, p-n junctions, interconnects, digital- or analog transistors can be fabricated using the same material: 2D graphene or GNRs of different widths.

The quantum confinement in the quasi-1D GNR channel creates discrete sub-band energy levels, which are filled by carriers in sequence as the gate voltage increases. As a result, staircase-like features are expected in the transfer curve. In Eq. (2-4) we practically defined the sub-band separation of the 1D GNR channel $\Delta E = \Delta E_{n+1} - \Delta E_n$. At zero temperature, only the energy levels below the Fermi level E_F populated with electrons in the conduction band, or those above E_F populated with holes in the valence band, contribute to the conductance. Each 1D energy level (or mode) has a finite transmission probability. The overall device conductance at a finite temperature is the summation of all the available conducting modes, and is described by the well-known Landauer formula:

$$\mathrm{G} = \left(\frac{2e^2}{h}\right)\sum_i t_i(E)\left(-\frac{\partial F}{\partial E}\right)dE \tag{2-7}$$

where t_i is the transmission probability of the i-th mode and f is the Fermi-Dirac statistics.

Sub-band formation in 30 nm wide GNRs has been observed at low electric fields showing the sub-band energy spacing (ΔE) around 50 meV [37]. A larger ΔE is expected in thinner GNRs. However, a smaller ΔE was found in the 20 nm wide GNRs reported here. A GNR band structure equation is used to explain the observation taking into account the edge roughness, ribbon width fluctuation, and crystal orientation mixture. Besides, the carrier mean free path is estimated from the transmission probability extracted by fitting the experimental data with Landauer formula. At high electric fields, the current-carrying capacity of 1D semiconductors is determined by the longitudinal optical (LO) phonon energy in the limit of ultrafast electron-optical phonon interaction and diffusive transport.[37] Owing to the large LO phonon energy (~160 meV), GNRs are expected to be able to exhibit large saturation current while at the same time providing as-designed planar patterning which is currently not achievable with carbon nanotubes (CNTs). Field effect transistors fabricated on the GNRs reported here show current saturation tendency with the maximum current density reaching 2 A/mm at high electric fields (75 kV/cm).

Their respective energy dispersion relation and density of states curves calculated via nearest-neighbor tight-binding approximation are also shown in the lower panels. According to this simple description, one can predict that zigzag ribbons of any width show a singular edge state that decays exponentially into the center of the ribbon. Such edge states are twofold degenerate at the Fermi energy and reveal a nondispersive feature that lasts about 1/3 of the total size of the graphene Brillouin zone. As a consequence, the density of states of zigzag ribbons is characterized by a pronounced peak located at the charge neutrality point. Although there are still controversies concerning the associated energy eigenvalue of the edge state, the detection of such a peak has been accomplished through scanning tunneling microscopy measurements performed near zigzag edge sections of graphite.[36, 38] In stark contrast, no such localized state appears in nanoribbons having an armchair edge configuration. Moreover, this simple model shows that armchair ribbons can change their electronic character depending on their width. An armchair nanoribbon can behave as a metal when the number of atoms along its width is equal to 3j + 2, where j is an integer. This class of armchair ribbons exhibits semiconducting behavior when more sophisticated electronic structure models are applied or the edge atoms are parameterized to include the effects of hydrogen passivation. The remaining armchair ribbons in the 3j and 3j + 1 categories are all semiconductors independent of the adopted model.[36, 38]

The challenge of inducing a band gap in graphene seems to be solved by cutting it into ribbons. On the other hand, the edges bring additional problems. Graphene nanoribbons indeed possess a band gap, but their edges have inherent edge disorder [36, 38]. It turns out that their electronic properties are strongly reliant on the topological details of the atoms located on their extremities. Roughness, or even chemical groups bound to the edges, can also affect the electronic features of the ribbons. In this sense, studies focusing on disorder effects in graphene structures are of extreme relevance for envisioning the main mechanisms behind their electronic response.

2.1.3 Graphene device applications

Graphene, the thinnest elastic material, has attracted lots of attention due to its outstanding standing electrical, mechanical, optical, and thermal properties.[4, 39-41] Its superb carrier mobility (up to 200,000 cm2/V·s at room temperature)[39, 40] and low resistivity (up to 30 Ω/□)[39] suggest the potential to outperform established inorganic materials for certain applications in high-speed transistors and transparent conductive films, respectively. Many experts believe that graphene with a 2D film format, in contrast to 1D format carbon nanotubes, offers fabrication methods that are compatible with a batch microfabrication process, which is essential to realizing practical devices or systems. As a result, graphene is particularly suitable for unusual format electronic systems such as flexible, conformal, and stretchable electronic devices with demanding high mechanical requirements. In particular graphene has a molecular structure basically similar to that of organic electronic materials, and the strong interaction between graphene and organic materials could result in excellent interface contact. This suggests that graphene is a good candidate as a transparent electrode for flexible organic devices such as organic photovoltaics and sensors.

The electronic properties of graphene, the significant mobilities of massless electrons/holes (due to its linearly dispersive band structure), and real two dimensional electron/hole systems (due to the thin monolayer structure) are superior advantages beyond any other semiconductor materials.[4, 42, 43] Thanks to the linear dispersion relation, the density of states in graphene is proportional to the energy, which creates extremely high saturation density of electrons and holes. Sheet electron/hole density on the order of 10^{13} cm^{-2} is easily obtainable, which is more than one order of magnitude higher than those of conventional semiconductor materials. Furthermore, the saturation velocities of electrons and holes are quite high and optical phonon energy is high enough that the optical phonon scattering becomes weaker than scattering in conventional semiconductor materials. When graphene is introduced in field-effect transistors (FETs) as the channel material, it will exceed the limits on conventional planar transistor performance, so that it could become a booster technology for making short-channel-free ultimately fast transistors.

2.1.3.1 Flexible transparent conductor

The optical image contrast can be used to identify graphene on top of a Si/SiO_2 substrate.[28] This scales with the number of layers and is the result of interference, with SiO_2 acting as a spacer. The contrast can be maximized by adjusting the spacer thickness or the light wavelength.[28, 44, 45] The transmittance of a freestanding SLG can be derived by applying the Fresnel equations in the thin-film limit for a material with a fixed universal optical conductance[44, 45] $G_0 = e^2/(4\hbar) \approx 6.08 \times 10^{-5}\ \Omega^{-1}$, to give:

$$T = (1 + 0.5\pi\alpha)^{-2} \approx 1 - \pi\alpha \approx 97.7\% \tag{2-8}$$

where $\alpha = e^2/(4\pi\varepsilon_0\hbar c) = G_0/(\pi\varepsilon_0 c) \approx 1/137$ is the fine-structure constant [45]. Graphene only reflects <0.1% of the incident light in the visible region11, rising to ~2% for ten layers.[28] Thus, we can take the optical absorption of graphene layers to be proportional to the number of layers, each absorbing $A \approx 1 - T \approx \alpha\pi \approx 2.3\%$ over the visible spectrum. In a few-layer graphene (FLG) sample, each sheet can be seen as a 2D electron gas, with little perturbation from the adjacent layers, making it optically equivalent to a superposition of almost non-interacting SLG [28]. The absorption spectrum of SLG is quite flat from 300 to 2,500 nm with a peak in the ultraviolet region (~270 nm), due to the exciton-shifted van Hove singularity in the graphene density of states. In FLG, other absorption features can be seen at lower energies, associated with interband transitions.[46, 47]

Optoelectronic devices such as displays touch screens, light-emitting diodes and solar cells require materials with low sheet resistance R_s and high transparency. In a thin film, $R_s = \rho/t$, where t is the film thickness and $\rho = 1/\sigma$ is the resistivity, σ being the d.c. conductivity. For a rectangle of length L and width W, the resistance R is:

$$R = \frac{\rho}{t} \times \frac{L}{W} = R_s \times \frac{L}{W} \tag{2-9}$$

The term L/W can be seen as the number of squares of side W that can be superimposed on the resistor without overlapping. Thus, even if R_s has units of ohms (as R does), it is historically quoted in ‘ohms per square’ (Ω/□). The dominant material is indium tin oxide (ITO), a doped n-type semiconductor composed of ~90% $In_2O_3$and ~10% SnO_2.[48] The electrical and optical properties of ITO are strongly affected by impurities [46, 49]. Tin atoms function as n-type donors.[48] ITO has strong absorption above 4 eV due to interband transitions[48], with other features at lower energy related to scattering of free electrons by tin atoms or grain boundaries.[46, 48, 49] ITO is commercially available with T ≈ 80% and R_s as low as 10 Ω/□ on glass [46, 48, 49], and ~60−300 Ω/□ on PET. Note that T is typically quoted at 550 nm, as this is where the spectral response of the human eye is highest.[46, 48, 49]

An ever-increasing cost due to indium scarcity[50], processing requirements, difficulties in patterning[48, 51] and a sensitivity to both acidic and basic environments. Moreover, it is brittle and can easily wear out or crack when used in applications involving bending, such as touch screens and flexible displays.[50] This means that new transparent conductor materials are needed with improved performance. Metal grids[2, 52], metallic nanowires[50] or other metal oxides[2] have been explored as alternatives. Nanotubes and graphene also show great promise. In particular, graphene films have a higher T over a wider wavelength range than single-walled carbon nanotube (SWNT) films, thin metallic films and ITO (Fig. 2.10a). We now present a relation between T and R_s for FLG films of varying doping levels. From equation (3), T depends on the optical conductivity G_0:

$$\mathrm{T} = \left(1 + \frac{G_0}{2\varepsilon_0 c} N\right)^{-2} \tag{2-10}$$

where N is the number of layers. The sheet resistance R_s is linked to the bidimensional d.c. conductivity σ_{2D} by:

$$R_s = (\sigma_{2D} N)^{-1} \tag{2-11}$$

Combining equations (2-10) and (2-11) and eliminating N gives:

$$\mathrm{T} = \left(1 + \frac{Z_0}{2R_s}\frac{G_0}{\sigma_{2D}}\right)^{-2} \tag{2-12}$$

where $Z_0 = 1/\varepsilon_0 c = 377\ \Omega$ is the free-space impedance, ε_0 is the free-space electric constant and c is the speed of light. In graphene1 we can take $\sigma_{2D} = n\mu e$, where n is the number of charge carriers. Note that for $n \approx 0$, σ_{2D} does not go to zero, but assumes a constant value1 of approximately $4e^2/h$. Thus, an ideal intrinsic SLG would beat the best ITO only in terms of T, not R_s. However, real samples deposited on substrates, in thin films or embedded in polymers are never intrinsic. Exfoliated SLG typically has $n \geq 10^{12}$ cm^{-2} (see ref. 80, for example), and much smaller R_s. The range of T and R_s that can be realistically achieved for graphene layers of varying thickness can be estimated by taking $n = 10^{12}$–10^{13} cm^{-2} and μ = 1,000–20,000 cm^2 V^{-1} s^{-1}, which is typical for films grown by CVD. Figure 2b,c shows that graphene can achieve the same R_s as ITO, ZnO/Ag/ZnO, TiO_2/Ag/TiO_2 and SWNTs with a similar or even higher T. Figure 2c plots T versus R_s for ITO, Ag nanowires75, SWNTs77 and the best graphene-based transparent conductive films (TCFs) reported so far, again showing that the latter is superior. For instance, taking $n = 3.4 \times 10^{12}$ cm^{-2} and $\mu = 2 \times 10^4$ cm^2 V^{-1} s^{-1}, we get T = 90% and R_s = 20 Ω/□.

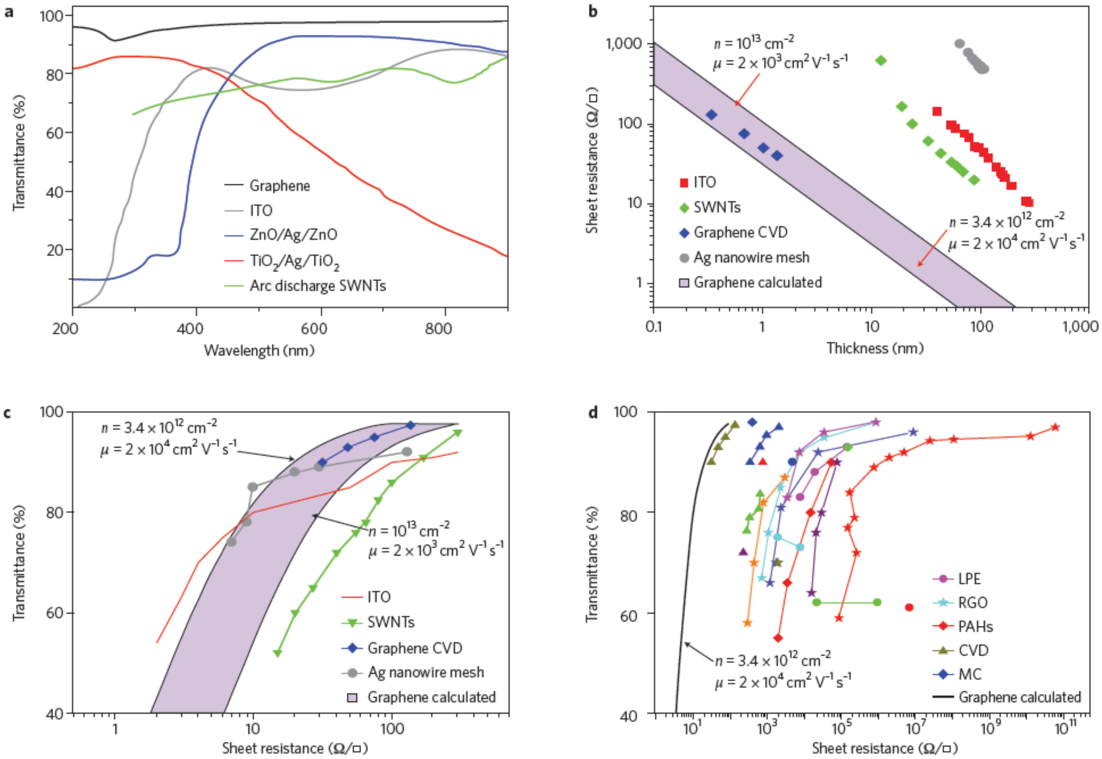

Figure 2.10: Graphene as transparent conductor. **a**, Transmittance for different transparent conductors: GTCFs, single-walled carbon nanotubes (SWNTs), ITO, ZnO/Ag/ZnO and TiO2/Ag/TiO2. **b**, Thickness dependence of the sheet resistance. The blue rhombuses show roll-to-roll GTCFs based on CVD-grown graphene; red squares, ITO; grey dots, metal nanowires75; green rhombuses, SWNTs. Two limiting lines for GTCFs are also plotted (enclosing the shaded area), calculated from equation (2.12) using typical values for *n* and *u*. **c**, Transmittance versus sheet resistance for different transparent conductors: blue rhombuses, roll-to-roll GTCFs based on CVD-grown graphene; red line, ITO; grey dots, metal nanowires; green triangles, SWNTs. Shaded area enclosed by limiting lines for GTCFs calculated using *n* and *u* as in **b**. **d**, Transmittance versus sheet resistance for GTCFs grouped according to production strategies: triangles, CVD; blue rhombuses, micromechanical cleavage (MC); red rhombuses, organic synthesis from polyaromatic hydrocarbons (PAHs); dots, liquid-phase exfoliation (LPE) of pristine graphene; and stars, reduced graphene oxide (RGO) [50, 53]. A theoretical line as for equation (2.12) is also plotted for comparison.

A key strategy to improving performance is stable chemical doping. Blake et al.[52] prepared GTCFs, produced by micromechanical cleavage, with $T \approx 98\%$ and R_s = 400 Ω/□, using a layer of polyvinyl alcohol to induce n-type doping. Bae et al.[39, 52] achieved $R_s \approx 30\ \Omega/\square$ and $T \approx 90\%$ by nitric acid treatment of GTCFs derived from CVD grown flakes — one order of magnitude lower in terms of R_s than previous GTCFs from the wet transfer of CVD films.[39, 52] Figure 2.10d is an overview of current GTCFs and GOTCFs. It shows that GTCFs derived from CVD flakes, combined with doping, could outperform ITO, metal wires and SWNTs. Note that GTCFs and GOTCFs produced by other methods, such as LPE, although currently having higher R_s at $T = 90\%$, have already been tested in organic light emitters[54] and solar cells.[2] These are cheaper and easier to scale than micromechanical cleavage or CVD films, and must be considered for applications in which cost reduction is crucial.

2.1.3.2 Field effect transistor

Graphene has been the subject of a lot of scientific research in recent years, due not only to their small size but to their remarkable electronic and mechanical properties and many potential applications. The problems associated with attempting to scale down traditional semiconductor devices have led researchers to look into graphene-based devices, such as graphene field effect transistors (GFETs), as alternatives. Because they are not subject to the same scaling problems as traditional semiconductor devices, GFETs are being studied for a wide variety of applications, including logic devices, memory devices, sensors, etc. The research on these devices typically involves determining various electrical parameters, which may include current-voltage (I-V), pulsed I-V, and capacitance (C) measurements. Characterizing the electrical properties of delicate nanoelectronic devices requires instruments and measurement techniques optimized for low power levels and high measurement sensitivity. When Novoselov *et al*.[4] first showed the existence of single layer graphene, they already extensively investigated the field effect behavior besides mobility and magnetoresistance. They fabricated back-gated Hall-bar structures, which were actually the first FETs demonstrated with graphene. Subsequent studies rapidly addressed issues central to FETs in the field of fabrication techniques[55], and modeling[56, 57]. The most important first steps were the investigation of the visibility of graphene on SiO_2[44, 52] and the experimental verification of band gap engineering of graphene nanoribbons.[33] High-field transport characteristics of graphene based devices are surprisingly not well studied yet. Early simulations predicted very clear drain current saturation at source-drain voltages as low as 0.1 V (~3 kV/cm). Experimentalists however had a difficult time to drive their 2D graphene FETs to clear saturation before breakdown and the necessary source-drain field was found to be 10-20 kV/cm[58]. The lack of bandgap restricts the on/off ratios to about 10x and prohibits saturation.

In Fig.2.11(a) a back-gate FET is shown that, depending on the gate potential, modulates the doping of its charge transfer regions (shaded in green for the case $V_G = 0$ in (b)), and therefore its access resistance R_{SD}. Because of the gapless property of graphene, typical GFETs exhibit ambipolar behaviour in which charge carriers change from electrons to holes and vice versa at a minimum conductivity point called Dirac neutrality point. In an ideal case, the transfer characteristic of GFET should be quasi ballistic. However, device fabrication and structure introduce limitations that make us to use drift-diffusion model to describe drain current. Also, some of these limitations such as source and drain contacts can be the origin of asymmetric transfer characteristics in some cases.[53]

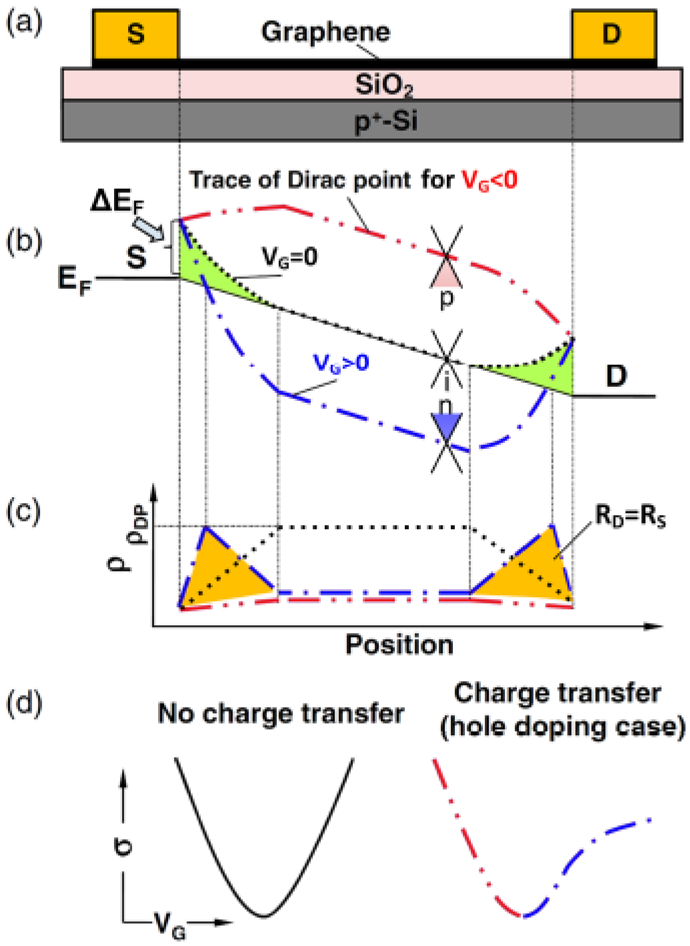

Figure 2.11: Potential and resistivity along the channel of a graphene FET. (a) structure of the back-gated FET; (b) Electrostatic potential represented as the trace of the Dirac point of graphene for $V_G > 0$ V (blue dash-dotted line), $V_G = 0$ V (black dotted line) and $V_G < 0$ V (red dash-double-dotted line); (c) Resistivity along the channel for various gate voltages. In yellow the area of the access resistances R_S and $R_D \cdot \rho_{DP}$ is the resistivity at the Dirac point in graphene.[53]

In recent years, several models for current-voltage characteristics of GFETs have been proposed.[59] For instance, a model tries to fit current voltage characteristics of GFET to that of conventional MOSFET. In this model, at low drain voltages ($V_{ds}<V_{gs}-V_0$), drain current can be described by equation (2.13) in which a constant charge carrier mobility is assumed.[59]

$$I_d = \frac{W}{L}\mu C_{ox}\left[\left(V_{gs} - V_0\right)V_{ds} - \frac{V_{gs}^2}{2}\right] \qquad (2\text{-}13)$$

This equation is the same as MOSFET drain equation except for V_0 which is the Dirac neutrality point in GFETs. In addition, there is always a minimum conductivity point much larger than the universal minimum conductivity ($4e^2/h$) due to inhomogeneity and thermal excitations.[9] Thus, the minimum conductivity should be considered in the transport model.

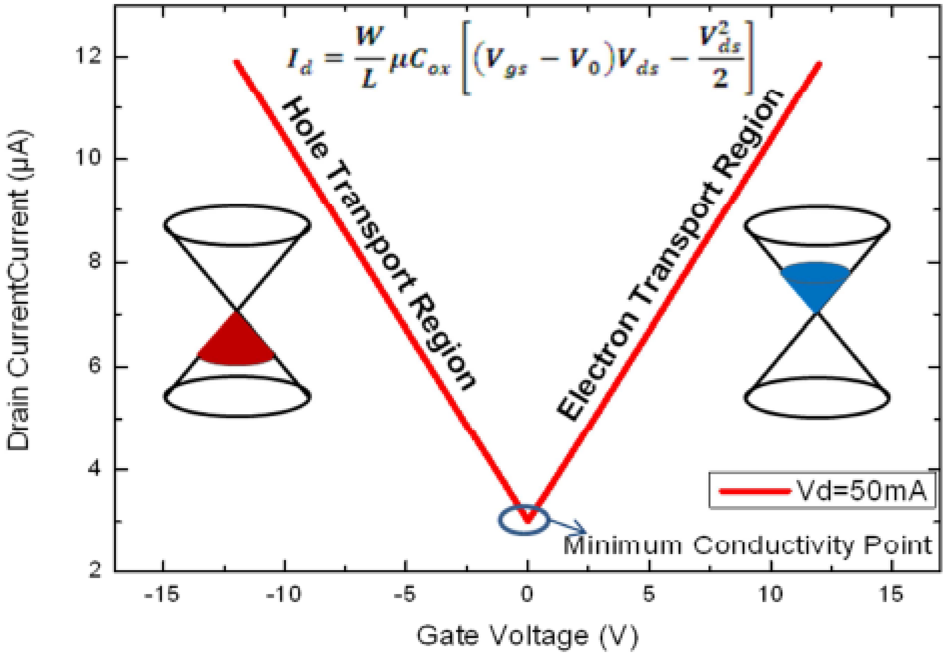

Figure 2.12: Simulated ideal drain current versus gate voltage using equation (2-13).[59]

Figure 2.12 shows the simulated transfer characteristic of graphene field effect transistor using equation 2-13, and a minimum conductivity. The V-shape of transfer characteristics reflects the ambipolar transport behaviour of GFETs. The ideal output characteristics of GFETs at low field ($V_{ds}<V_{gs}-V_0$) exhibits linear behaviour as shown in

Figure 2.13.

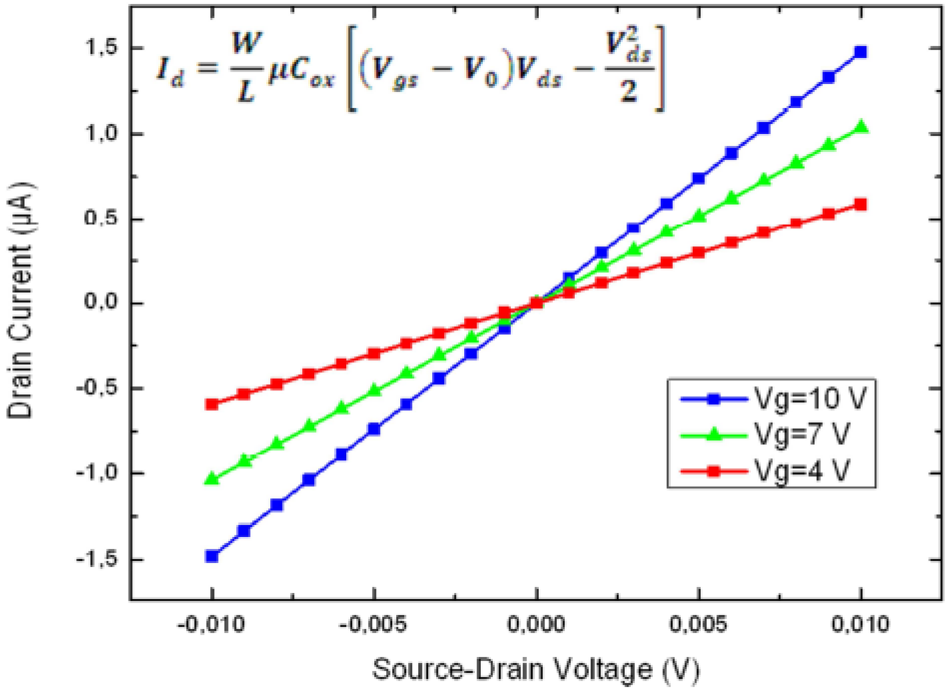

Figure 2.13:Simulated ideal drain current against source-drain voltage for different gate biases.[59]

It is well known that mobility is a function of carrier concentration in graphene and very high mobility values can be obtained only at very low carrier concentrations. We start with the equation for the drift current of a graphene FET

$$J = en\mu F \tag{2-14}$$

where n is the 2D carrier concentration, and F is the electric field along the channel. The conductivity is $\sigma = J/F$, and one can extract the mobility specifically for a 2D graphene field effect transistor geometry:

$$\mu_{CON} = \frac{\sigma}{en} = \frac{I_D}{V_{DS}}\frac{L_G}{W}\frac{1}{en} = \frac{I_D}{V_{DS}}\frac{L_G}{W}\frac{1}{C_{OX}(V_{GS} - V_0)} \tag{2-15}$$

where e is the electron charge, n is the 2D carrier concentration, L_G is the gate length, W is the channel width, V_{DS} is the source-drain bias, V_{GS} is the gate bias and V_0 is the threshold or Dirac-point voltage. This definition of the mobility is inversely proportional to carrier concentration therefore it gives extremely high mobility values for low carrier concentrations. This can be called conductance based mobility (μ_{CON}). We can also define a field-effect mobility (μ_{FE}) as the change in the sheet conductivity of graphene due to carrier density modulation Δn as

$$\Delta\sigma = \Delta n e \mu \qquad (2\text{-}16)$$

The expression can be modified to the form:

$$\mu_{FE} = \frac{\Delta\sigma}{\Delta n} e = \frac{L_G}{W} \frac{g_m}{C_{OX} V_{DS}} \qquad (2\text{-}17)$$

where $g_m = dI_D / dV_{GS}$ is the transconductance. As opposed to μ_{CON} the field-effect mobility μ_{FE} goes to zero at the lowest carrier concentrations at the Dirac point, since the drain current reaches a minimum when the gate bias equals the Dirac point, and by definition $g_m = dI_D / dV_{GS} = 0$. By comparing the result of the two calculation methods (Figure 2.14) for the same FET transfer measurement, we can conclude that the two versions of mobility are close for carrier densities $n > 10^{12}$ cm^{-2}. However, by analyzing many devices, we see that μ_{CON} is usually about twice as much as μ_{FE} even at high carrier densities. It can be shown that the two methods would give equivalent results in the limiting case when the source-drain current varies linearly with the gate voltage, i.e. if the mobility is not a function of the carrier concentration, which is true for graphene[57] only within a window of carrier concentrations.[57, 60]

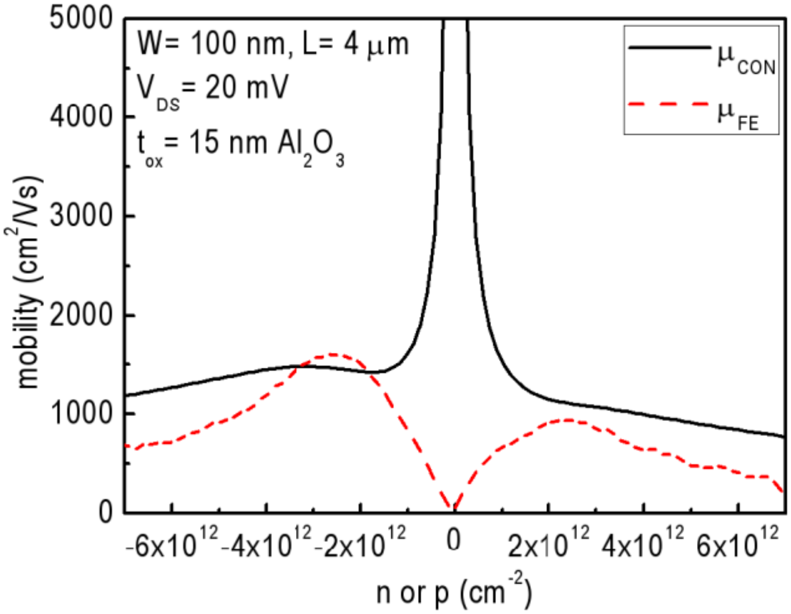

Figure 2.14: Calculated mobilities as a function of the carrier concentration of a back gated graphene FET. There is a significant deviation around n = 0 cm^{-2}, but above n = 10^{12} cm^{-2} the difference is acceptable and the trend is similar.[57, 60]

When graphene is applied in transistors, the mobility of charge carriers degrades significantly due to extrinsic scattering mechanisms. This degradation even increases significantly from back-gate devices to double-gate ones. In fact, scattering from charged impurities at the interface of graphene/dielectric and near the interface dominates among other mechanisms such as remote interfacial phonon (RIP) scattering.[61] These interface and near interface states can be charged and discharged via graphene channel if their energy levels are below or above the Fermi energy level in graphene respectively.[61]

Lowering the density and effect of charged impurities is critical to improve the mobility. Thus, replacing the dielectric material for both substrate and top gate with a high-k material can be solution. High-k materials can reduce the charged impurity scattering because of increased screening effect[61, 62], and also improves the gate charge control on the channel due to the higher gate capacitance. Using high-k material in GFETs is still a trade-off since it introduces more charged impurities than SiO_2, and it may also increase RIP at room and higher temperatures.[62]

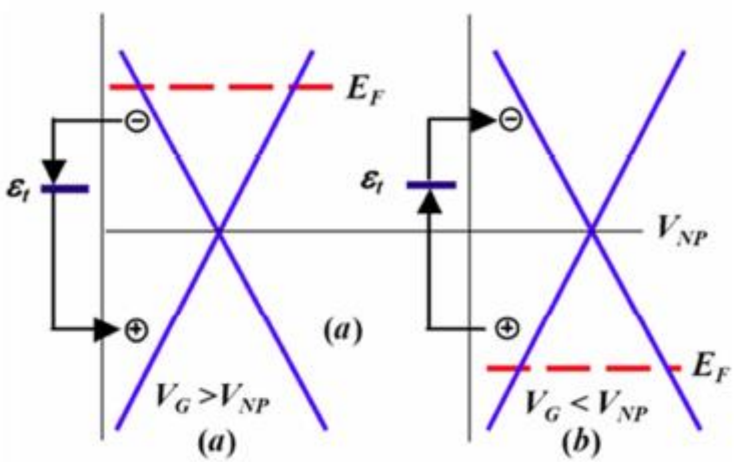

Figure 2.15: Traps fill and empty via tunneling [42]

On the other hand, the deposition of high-k may reduce mobility of carriers in GFETs due to the defects introduced into graphene sheet. Among different deposition methods for top gate dielectric, physical layer deposition results in more defects and lower quality, while atomic layer deposition (ALD) can provide high quality dielectric thin film with precise thickness with less damage into the graphene layer underneath.[63] Yet, the surface of graphene requires a functionalization[64] or buffer layer[63] in order to be able using ALD for top gate dielectric deposition. Significant research has been made not only to optimize ALD process, but also to find other deposition techniques such as recently developed “Physical assembly of freestanding dielectric nanostructures on graphene.[63]”

2.1.3.3 Sensor

In recent years, the global development of industrial and chemical activities has been very strong due to the increasing demand of high technology. The technologies are constantly evolving to meet the human standards and expectations. Although the rapid growth of industries in last century is a result of human demands, it has also caused radical changes in human life. In a notion of safe understanding, gases and vapors other than air can pose a threat to human life. According to the U.S. Environmental Protection Agency, acid rain is a broad term referring to a mixture of wet and dry deposition (deposited material) from the atmosphere containing higher than normal amounts of nitric and sulphuric acids.[67] Any industrial applications resulting in the primary emissions of sulfur dioxide (SO_2) and nitrogen oxides (NO_x) are responsible for acid rains, such as fossil fuel combustion, electrical power generation systems, oil refining plants and many more. Acid rain can contaminate drinking water, cause harm to vegetation and aquatic life, and erode buildings. The emission of toxic pollutants, such as nitro oxide (NO_x), Benzene, Carbon monoxide (CO), Ammonia (NH_3) into the air can have serious effects to human health and the environment. Toxic gases can get into human body through breathing, ingestion or skin absorption. They can stay inside the lungs, be exhaled or move into the bloods from the lungs, the digestive system or skins.

In these years, different studies have established various branches of gas sensing technology. The investigation of different kinds of sensors, research about sensing principles and fabrication techniques are some of the major areas receiving most attention in gas sensor developments. Depending on the sensing mechanism employed in gas sensors, the sensing technologies can be broadly divided into two different categories: sensing methods based on variation of electrical properties (solid state gas sensors) and other properties such as mass spectrometer, nuclear magnetic resonance

(NMR) and gas chromatography. Traditional analytical instruments (mass spectrometer, NMR, gas chromatography, calorimetric) are expensive, complex and large in size. In addition, most analysis requires sample preparation so that on-line, real-time analysis is difficult. On contrary, solid state gas sensors, are the best candidates to the development of commercial gas sensors for wide range of applications due to numerous advantages such as small sizes, high sensitivities in detecting low concentrations of a wide range gaseous chemical compounds Semiconductor gas sensors, known as chemo-resistive gas sensors, are typically based on metal oxides (MO) and are one of the widely studied groups. The metal oxide semiconductor (MOS) gas sensors are applied to detect target gases through redox reaction between the target gases and the oxide surface. These sensors are designed to interact with the target gas through surface adsorbed oxygen ions. The process of interaction results in the changes in the changes in the carrier concentration of the material. The changes in carrier concentration in turn change the conductivity or resistivity of the material, yielding a certain signal. The signals are thus the result of the process of oxidation and reduction in the metal oxide surface.[65, 66] In spite of the numerous advantages of metal oxide semiconductor gas sensors, they have some disadvantages too. Poor reproducibility, long-time stability due to aging, sensitivity to water vapor and lack of selectivity are some of the prominent issues in metal oxide semiconductor gas sensors. When the metal oxide semiconductor sensor works for long period, aging effect in the device appear as a non-linear drift of the baseline signal or a drift in the sensor response.[65] Metal oxide semiconductor gas sensors show poor selectivity. The property of being sensitive to different gases causes a real problem when different reactive gases are present simultaneously in the same atmosphere and interference effect between them can occur.

The gas sensing mechanism of graphene is attributed to the adsorption and desorption of gas molecules, acting as donors and acceptors, on the surface.[6] Graphene is a better candidate for the electrically based sensor for mainly two reasons. In one hand, its two dimensional structure with one atom thickness allows a full exposure of all atoms for obtaining better adsorption of gas molecules.[19] For instance, mechanically exfoliated graphene has shown a potential ability to detect gases down to single molecular level.[6] On the other hand, it does not require high impedance and other special circuits to reduce the noise signal because of its high crystal quality and low resistance (typically few hundred ohms).[11] In addition, its amenability for making devices using conventional lithography processes and a long term stability of the material has brought it as a potential candidate for gas sensors. In this chapter, we will describe the gas sensor characteristics of graphene surface for different target gasses at different temperatures. Due to the reactivity of metal oxide surface atoms, which lack binding partners, molecules from the gas phase are adsorbed at the surface. The first step of association of gas species with a solid surface is physisorption, afterwards the physisorbed species can be chemisorbed-often named ionosorption when the adsorbate acts as a surface state- if they exchange electrons with the semiconductor surface.

M. Alvisi et al. used a Quartz Crystal Microbalance (QCM) gas sensor coated with CNTs layered film for the detection of different vapors of ethanol, methanol, acetone, m-xylene, toluene and ethyl acetate in a wide range of concentration from 10 to 800 ppm. F. Schedin et al. used graphene field effect transistors (GFET) for the detection of ethanol at the room temperature.[6] However, the detection of organic vapors in terms of the changes in the resistance between the electrodes is yet to emerge as a reliable technique. In addition, the goals of solid state gas sensors are to be low cost, low-power consumption, reliable, smart and miniaturized sensing devices[6], requiring the sensor device to integrate with other electronic devices, to design at low cost and to operate at unheated conditions. On the other hand, the outstanding electronic properties of graphene and its amenability in making low-cost sensor devices have drawn our interests in using graphene as a sensing channel for organic vapors as well.

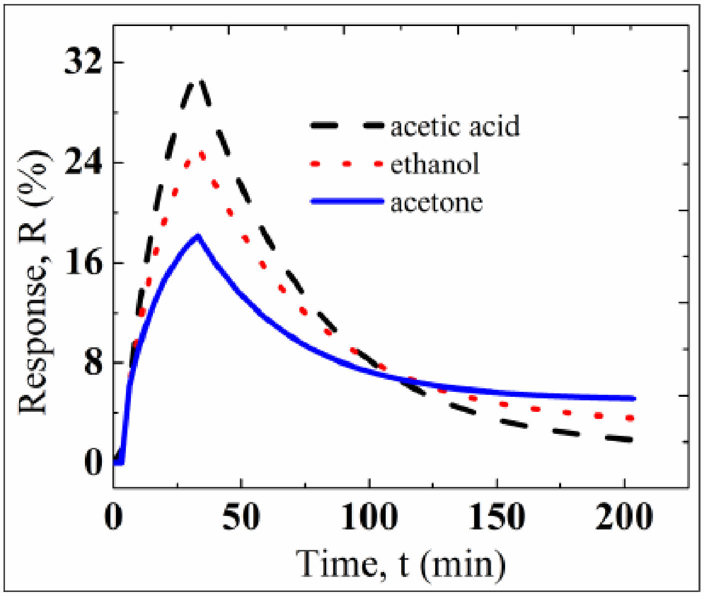

Figure 2.16: Dynamic response of sensor device with bare graphene as a sensing channel for three different organic vapors.[67].

In this work, the detection of organic vapors (ethanol, acetic acid and acetone) with lower concentrations (< 200 ppm) at the room temperature (RT) has been studied with CVD grown graphene surface as a sensing channel. Response of the graphene based devices can be further enhanced by functionalizing its surface with catalytic metals such as platinum (Pt), palladium (Pd), aluminum (Al) and gold (Au). Based on these reports, graphene surface integrated with metallic nanoparticles can be an attractive approach for the detection of organic vapors. In this work, the sensitivity of graphene based devices has been greatly enhanced by the decoration of metallic nanoparticles, such as Pt and Au. The results indicated that the organic vapors tested in this work interacted strongly with the graphene surface. With the adsorption of different oxygen species prior to the introduction of organic vapors, graphene might act as a Lewis acid, while the vapors could be Lewis base as they included an OH of carbonyl/carboxyl group.[67] As a result, an acid-base interaction might occur even at the room temperature. The adsorption of organic vapors on graphene surface occurs through the dissociation of the molecule to an $H^{\pm}$ or OH^{-} ions to form many different intermediate states. Ethanol may dissociate to an $H^{\pm}$ ion to form surface alcoxide or surface hydroxyl, which is further transformed to form aldehyde or a ketone.[51] Acetic acid can also be adsorbed in various forms in similar manner. Acetone may transfer to its isomer, enolate, which can further react with other acetone molecules to form mesityl oxide before being finally adsorbed.[67] The sensing mechanism of organic vapor is a complex process. However, the final reactions of ethanol and acetone with adsorbed oxygen species can be described in crude form:[67, 68] The exchange of charge carriers occurs between graphene and adsorbates as a result of the chemical reaction. As a result, the resistance of the graphene film increases.

$C_2H_5OH(ads) + 6O^{-}(ads) \rightarrow 2CO_2 + 3H_2O + 6e^{-}$

$(CH_3)CO(ads) + 8O^{-}(ads) \rightarrow 3CO_2(g) + 3H_2O(g) + 8e^{-}$

There are two important remarks from the detection of organic vapors in this process. One of them is the oxidation reaction of these adsorbates on the surface of graphene. As air is continuously passed to the chamber at a constant rate, oxygen species are adsorbed in different forms (O_2^-, O^{--}). The process of oxidation of organic molecules depends on the availability of the adsorbed oxygen species, which can be enhanced by operating the device at high temperature. The purpose of this work was to test the organic vapors at the room temperature under the ambient condition. Therefore, operating temperature of the device was not increased above the room temperature. Moreover, the flow of air was always kept constant to see the response behavior for different concentrations under similar conditions. Another important remark is that among the vapors tested, the sensitivity of acetic acid vapors was the highest while that of acetone was the lowest. It indicated that the graphene surface had different surface reactivity to different vapors. The process of oxidation begins with the dissociation of vapor molecules into different intermediate stages before it is finally adsorbed. The sensitivity of the device for acetic acid vapor was ~ 60-70% higher than acetone. It can be attributed to the fact that the acetic acid vapors tend to dissociate to H± ions easily with adsorbed oxygen species, while acetone has no formation of H^+ ions or OH^- groups that are easily reacted.[67] However, the true origin of physical and chemical implications of adsorption processes requires further theoretical investigations.

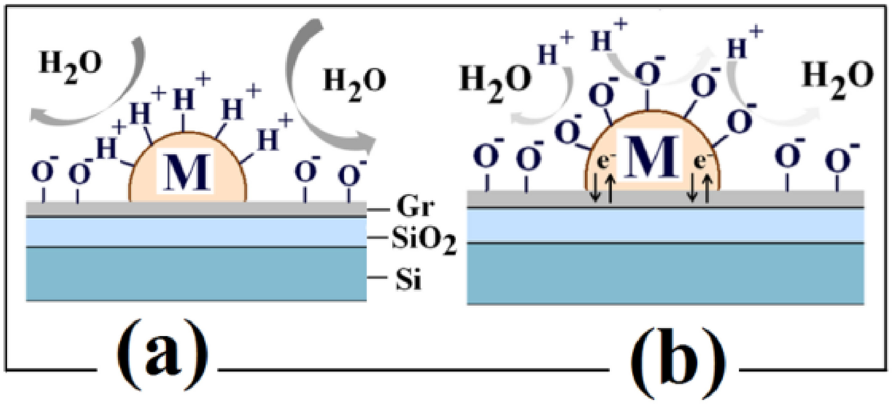

Figure 2.17: Schematic represntation of (a) chemical and (b) elecronic processes involved in gas sensing mechanism of graphene based sensor.[67]

2.2 Drug Delivery Systems

Drug delivery systems are formulations or devices that enable the introduction of a therapeutic substance in the body and improve its efficacy and safety by controlling the rate, time, and place of release of drugs in the body.[69] Drug delivery systems can improve the pharmacological properties of free drugs using particulate carriers, composed primarily of lipids and polymers.[70] Drug delivery systems may involve enhanced bioavailability, improved therapeutic index, or improved patient acceptance or compliance.

Drug Delivery Systems are designed to consider drug properties such as potency, stability, solubility, size, and charge. Polymer conjugated Drug Delivery Systems which can carry small amount of molecules needs drugs with higher potencies to deliver therapeutically effective amount of drugs.[71] Contrastively, because liposome can entrap large amount of therapeutic molecules, drug potency is less considerable for this carrier.[72] However, the size of therapeutic molecules is also very important issue for Drug Delivery Systems. Even the high capacity of liposomes becomes problematic for proteins which are large size molecules. Because drug solubility may be a limiting factor for drug retention, it can be also an important consideration in Drug Delivery System. Hydrophilic drugs can be readily delivered with carrier-drug conjugates, but hydrophobic drugs need the intermediate between hydrophobic drugs and hydrophilic media of bodies.[73]

A schematic illustration (Figure 2.18) illustrates the passive or ligand-targeted accumulation of Drug Delivery Systems in breast cancer tumors through the Enhanced Permeability and Retention (EPR) effect.[74] Drug Delivery Systems containing an anticancer molecule are injected through blood vessel, and extravasated from the blood through the leaky endothelial cells and accumulated in tumor tissue (dark green in Figure 2.18 A). The therapeutic molecules are released from Drug Delivery Systems by two different environments: (a) the molecules are released at extracellular environment and taken up into the cells. (b) Ligand-targeted Drug Delivery Systems containing anticancer molecules bind to cell surface receptors which can internalize Drug Delivery Systems into endosomes and the anticancer molecules escape the endosomes and perform its intracellular action.[70]

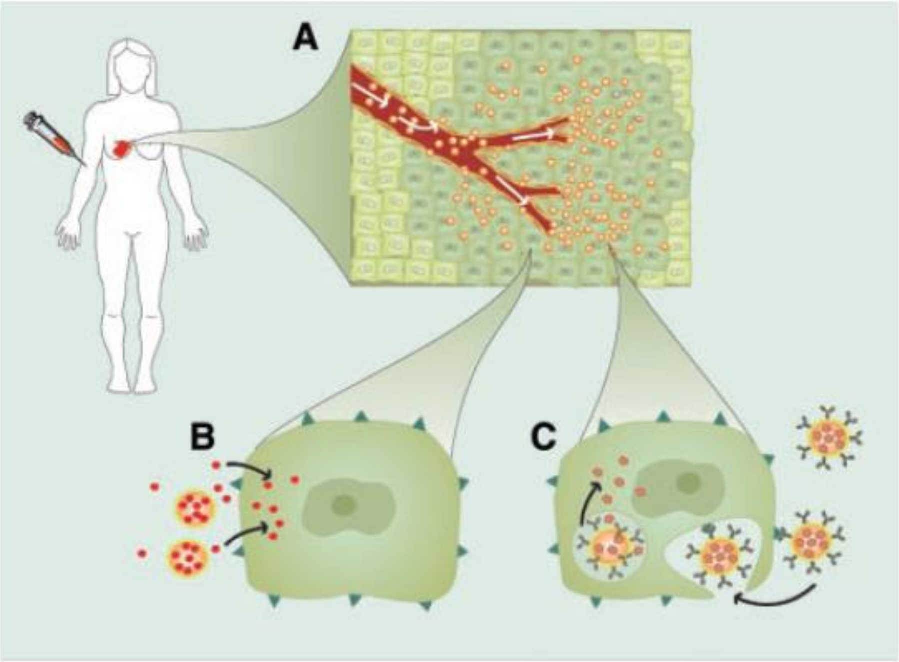

Figure 2.18: Schematic illustration showing the passive or ligand-targeted accumulation of Drug Delivery System in breast cancer tumors through the Enhanced Permeability and Retention (EPR) effect[70].

Table 2.1 summarized the non-ideal properties of free drugs and their therapeutic implication. Drug delivery systems (DDSs) provide the ideal properties to maximize the therapeutic efficacy with free drugs. For example, the poor solubility of hydrophobic drugs (most of pharmaceutical drugs are hydrophobic.) makes them precipitate in aqueous media in the body. Using drug delivery system such as lipid micelles or liposomes provides both hydrophobic and hydrophilic environment, enhancing drug solubility. Drug delivery systems decrease the tissue toxicity and side effect. Drug delivery systems also protect the drug from premature degradation and functions and reduce clearance. Drug delivery systems can increase drug concentrations in disease tissues such as tumor through a triggered release mechanism-by changes in pH, temperature, or magnetic fields or by engineered sensitivities to biocompatible chemicals and enzymes, light, or radiofrequency.[75, 76]

Table 2.1: Non-ideal properties of drugs and their therapeutic implications [70].

Problem	Implication	Effect of DDS
Poor solubility	A convenient pharmaceutical format is difficult to achieve, as hydrophobic drugs may precipitate in aqueous media. Toxicities are associated with the use of excipients such as Cremphor (the solubilizer for paclitaxel in Taxol)	DDS such as lipid micelles or liposome provide both hydrophilic and hydrophobic environments, enhancing drug solubility.
Tissue damage on extravasation	Inadvertent extravasation of cytotoxic drugs leads to tissue damage, e.g., tissue necrosis with free doxorubicin.	Regulated drug release from DDS can reduce or eliminate tissue damage on accidental extravasation.
Rapid breakdown of the drug in vivo	Loss of activity of the drug follows administration, e.g., loss of activity of Camptothecin at physiological pH.	DDS protects the drug from premature degradation and functions as a sustained release system. Lower doses of drug are required.
Unfavorable pharmacokinetics	Drug is cleared too rapidly, by the kidney, for example, requiring high doses or continuous infusion.	DDS can substantially alter the PK of the drug and reduce clearance. Rapid renal clearance of small molecules is avoided.
Poor biodistribution	Drugs that have widespread distribution in the body can affect normal tissues, resulting in dose-limiting side effects, such as the cardiactoxicity of doxorubicin.	The particulate nature of DDS loweer the volume of distribution and helps to reduce side effects in sensitive, nontarget tissues.
Lack of selectivity for target tissues	Distribution of the drug to normal tissues leads to side effects that restrict the amount of drug that can be administered. Low concentrations of drugs in target tissue will result in suboptimal therapeutic effects.	DDS can increase drug concentrations in diseased tissue such as tumors by the EPR effect. Ligand-mediated targeting of the DDS can further improve drug specificity

2.2.1 Nanotechnology on Drug Delivery

The application of nanotechnology toward drug delivery is widely expected to achieve (a) improved delivery of poorly water-soluble drugs, (b) targeted delivery of drugs in a cell- or tissue-specific manner, (c) transcytosis of drugs across tight epithelial and endothelial barriers, (d) delivery of large macromolecule drugs to intracellular sites of action, (e) co-delivery of two or more drugs or therapeutic modality for combination therapy, (f) visualization of sites of drug delivery by combining therapeutic agents with imaging modalities, and (g) real-time read on the *in vivo* efficacy of a therapeutic agent [77]. In order to develop the current clinically approved nanotechnology products, many parameters are considered for the successful development and manufacturing of targeted drug delivery vehicles including (a) the use of biocompatible materials with simple robust processes for biomaterial assembly, conjugation chemistry, and purification steps; (b) the ability to optimize in parallel the myriad of biophysicochemical parameters of targeted drug delivery vehicles important for pharmacokinetic properties and possible cell uptake; and (c) developing scalable unit operations amenable to manufacturing large quantities of targeted drug delivery systems needed for clinical translation. Figure 2.19 shows that the efficacy of nanoparticles as delivery vehicles is highly size- and shape-dependent. The size of the nanoparticles affects their movement in and out of the vasculature, whereas the margination of particles to vessel wall is impacted by their shape [77].

After particles extravasate out of the vasculature into the tumor tissue by Enhanced permeability and retention (EPR) effects, specific uptake by cancer cells is facilitated by active targeting and receptor-mediated endocytosis (Figure 2.20). Figure 2.20 presents passive *vs.* active targeting: (Right) Particles tend to passively extravasate through the leaky vasculature, which is characteristic of solid tumors and inflamed tissue, and preferentially accumulate through the Enhanced permeability and retention (EPR) effect. In this case, the drug may be released in the extracellular matrix and diffuse throughout the tissue for bioactivity. (Middle) Once particles have extravasated in the target tissue, the presence of ligands on the particle surface can result in active targeting of particles to receptors that are present on target cell or tissue resulting in enhanced accumulation and cell uptake through receptor-mediated endocytosis. This process, referred to as “active targeting”, can enhance the therapeutic efficacy of drugs, especially those which do not readily permeate the cell membrane and require an intracellular site of action for bioactivity. (Left) The particles can be engineered for vascular targeting by incorporating ligands that bind to endothelial cell-surface receptors. While the presence of leaky vasculature is not required for vascular targeting, when present as is the case in tumors and inflamed, this strategy may potentially work synergistically for drug delivery to target both the vascular tissue and target cells within the diseased tissue for enhanced therapeutic [77].

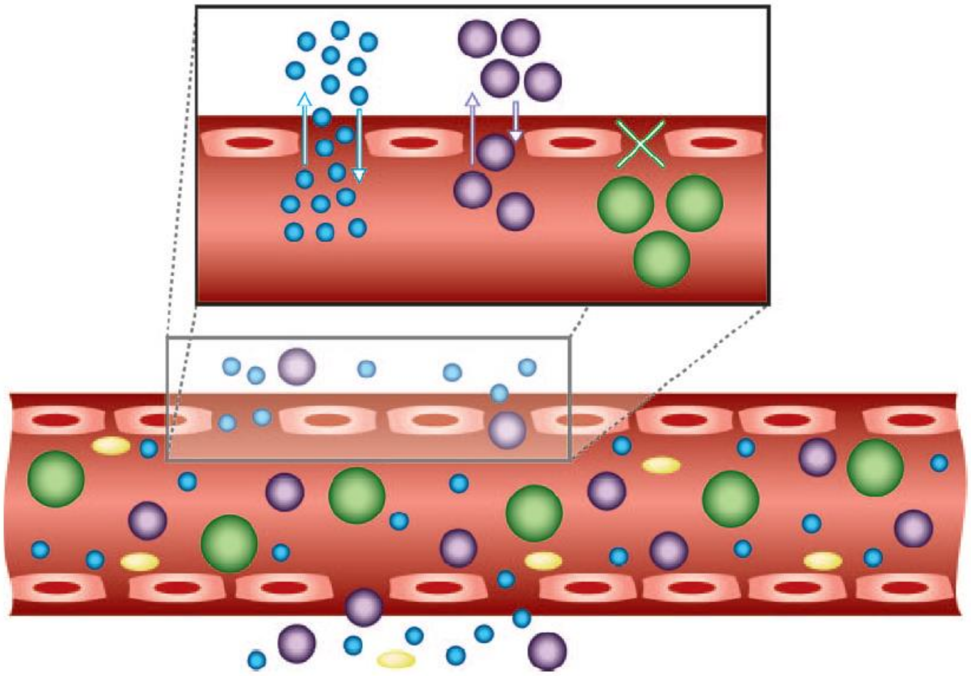

Figure 2.19: Efficacy of nanoparticles as delivery vehicles is highly size- and shape-dependent[77].

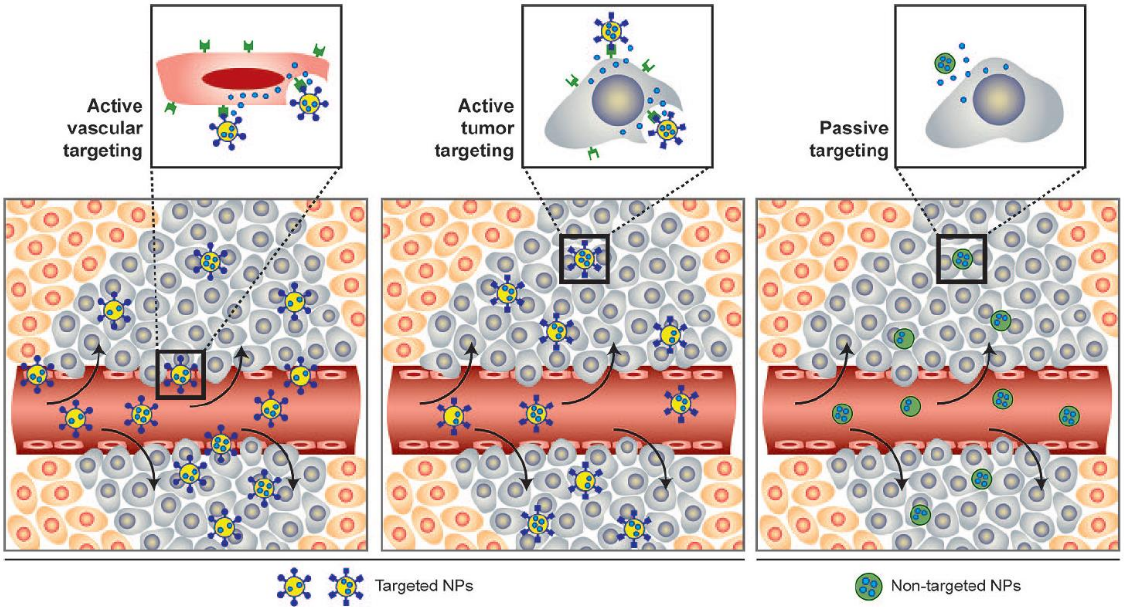

Figure 2.20: Passive *vs* active targeting [77].

2.2.2 Magnetic nanoparticles and its triggered drug Release

Iron oxide is one of the most commonly employed materials for nanoparticle synthesis, having long history of biomedical applications [78]. Iron oxide magnetic nanoparticles are smaller than approximately 20-30 nm in size containing a single magnetic domain with a single magnetic moment exhibiting superparamagnetism [79]. Their relatively small size provides greater surface area-to-volume ratios which improve their binding kinetics and biodistribution for *in vitro* assay and *in vivo* imaging, respectively. Applying external magnetic field causes the alignment of magnetic moment of the entire particles yielding a fixed magnetization direction which gives imaging application such as magnetic relaxation switching (MRS).

The common aqueous syntheses of superparamagnetic iron oxide nanoparticles (typically less than 20 nm) are alkaline coprecipitation and microemulsion-based precipitation/oxidation of ferrous and ferric salts (Fe^{+2} and Fe^{+3}). Nanoparticle size is controlled by solution ionic strength, pH values, and reactant stoichiometries [80]. Another way to synthesize superparamagnetic iron oxide nanoparticles is the base-induced precipitation and oxidation of iron salt-surfactant complexes within the cores of nanoscale emulsions. This method is influenced by reactant stoichiometry, solvent systems, and surfactants-all of them give the significant influence of the complex dynamics of particle formation [81]. On synthesized iron oxide nanoparticles, selected hydrophobic surface ligands can be used as surfactants. For this purpose, the surface of nanoparticles needs to be modifided for biological applications in order to solubilize them in aqueous solutions.

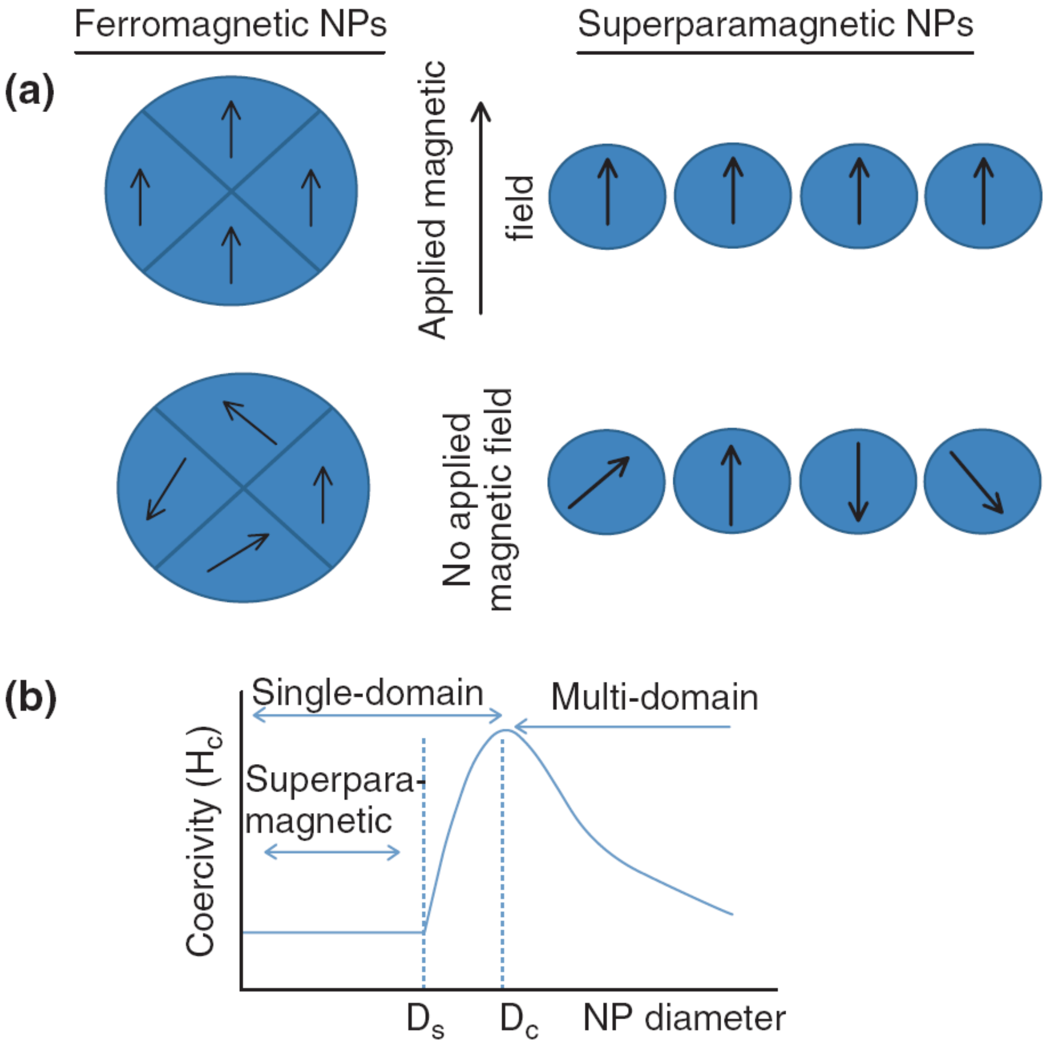

Figure 2.21: Magnetization behavior of ferromagnetic and superparamagnetic nanoparticles under an external magnetic field (D_s and D_c are the superparamagnetism and critical size thresholds.) [78].

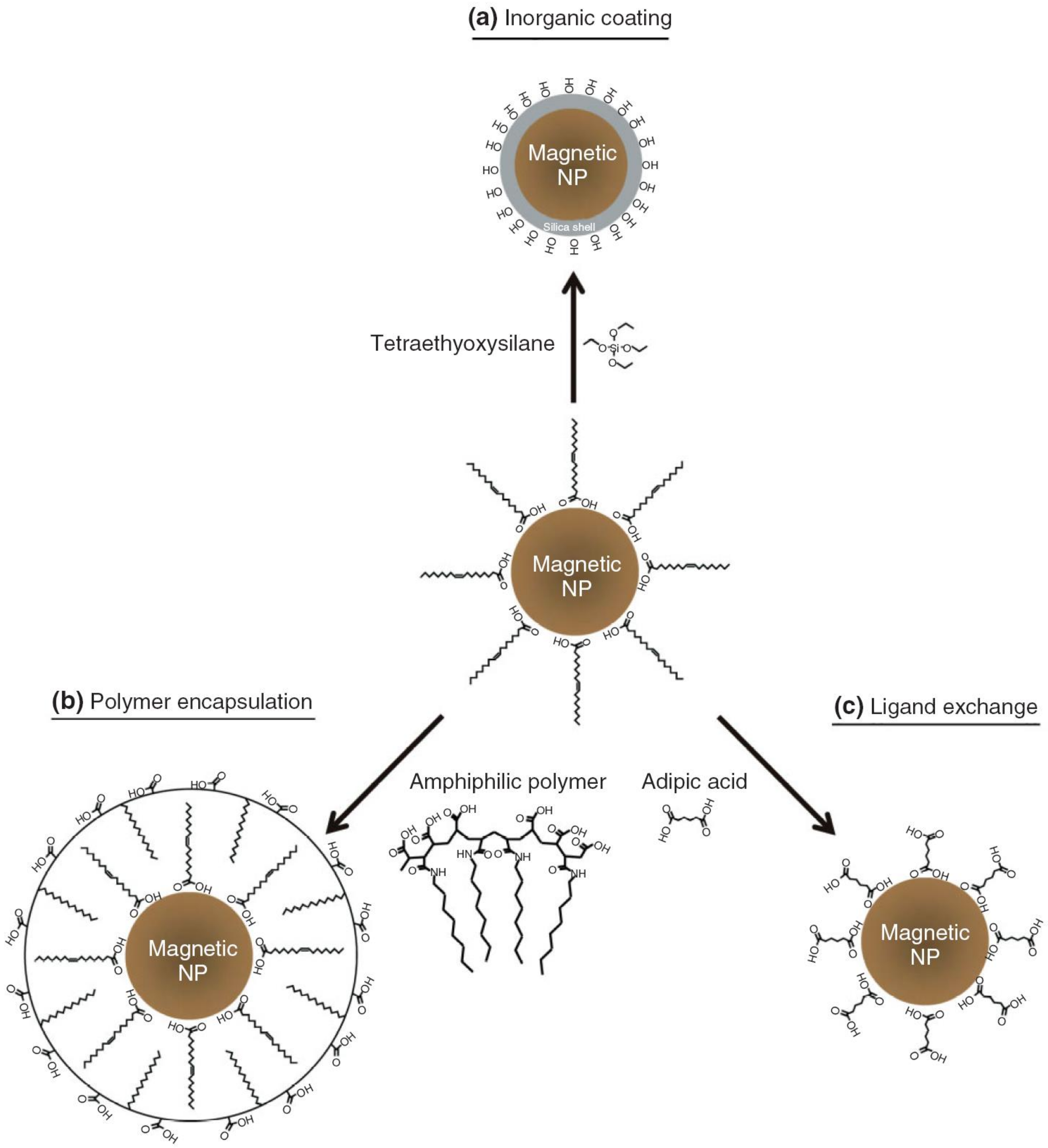

Figure 2.22: General surface modification schemes of magnetic nanoparticles [78].

The properties of both the particles and the applied field influence the heating of magnetic nanoparticles. Figure 2.22 shows the device to create an alternating current (AC) magnetic field using electric coil to focus the magnetic field within. Thermal infrared images are shown to collect temperature data (Figure 2.22 b). In order to generate heat with alternating current (AC) magnetic field, the applied frequency is very important (the usual range of pulsed frequencies to generate heat is from 50 kHz to 10 MHz.).

The hyperthermia as a cancer treatment technique has been using the application of heat to preferentially kill cancer cells while having a lesser effect on healthy cells with magnetic fluid [8]. The temperature for hyperthermia is about 45 ℃, as higher temperature causes whole cell necrosis in both healthy tissue and cancerous tumors [82]. The first investigation of magnetic fluid hyperthermia treatment using magnetic nanoparticles to be heated by an alternating current (AC) magnetic field was by Gilchrist *et al.* in 1957 [83]. Each magnetic nanoparticle (superparamagnetic nanoparticles which sizes are typically below 10 nm) is heated by applied field through the mechanism of Neel relaxation or rotation of the magnetization. Using the targeted ligands which conjugate the receptors overexpressed in many types of cancer cells, magnetic nanoparticles are localized at the cancerous tissue and then give heat to localized small tissue and potentially even individual cells by external magnetic field.

Externally triggered drug release is a highly desired mean for drug delivery systems. Specially, magnetothermally-triggered drug delivery systems can release drugs by external stimulus, alternating current (AC) magnetic field, to the body. The controlling drug release offers the benefit to patient by reducing the total amount of drugs required to reach an effective dose, reducing the frequency of administration, and assisting in sophisticated devices that include targeting, imaging and multiple modes of therapy [82]. Magnetically triggered release can be achieved by the oscillatory motion of magnets to mechanically open polymers resulting in drug diffusion [84], or magnetic heating of nanoparticles to give stimulus to thermally-responsive polymer [85].

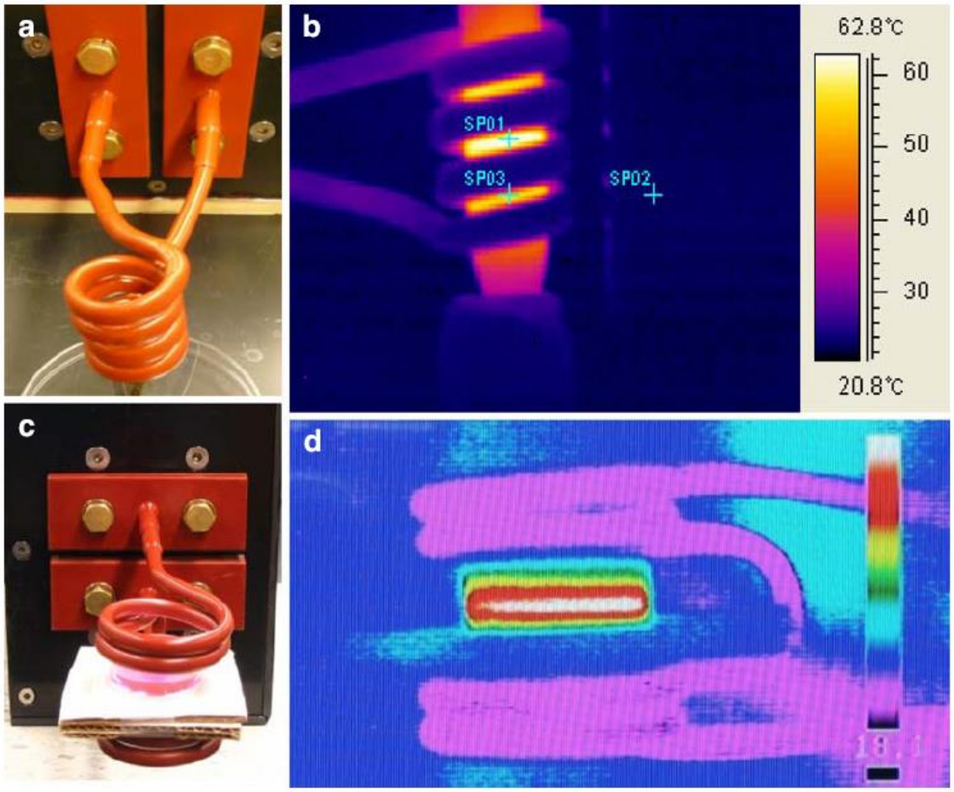

Figure 2.23: Magnetic coil for creating AC magnetic field and infrared temperature images of nanoparticle solutions [82]

These methods for magnetically-triggered releases are used for several biomedical and biological applications. Superparamagnetic iron oxide nsnoparticles can be combined with a biodegradable gel to prolong the local delivery of dexamethasone as an anti-inflammatory agent [86]. Magnetic nanoparticles can be also used in tissue engineering by attaching to cell membranes and applying an oscillating field to condition the cells for tissue growth [87].

Figure 2.20 shows magnetothermal responsive drug delivery systems using hydrogel structure. Magnetic nanoparticles are represented by rectangles, molecularly dispersed drug by circles, and thermoresponsive grafts are shown attached to the base network in the third depiction. Magnetic nanoparticles designed with the proper composition and size to accomplish heating using an alternating current (AC) magnetic field place the interior of thermally-responsive hydrogel and the pores of hydrogel are opened to release drugs, once heated. The nanoparticles are embedded directly in polymer or self-assembled to encapsulate nanoparticles resulting in new structures such as micells, liposomes, or polymersomes [68, 88].

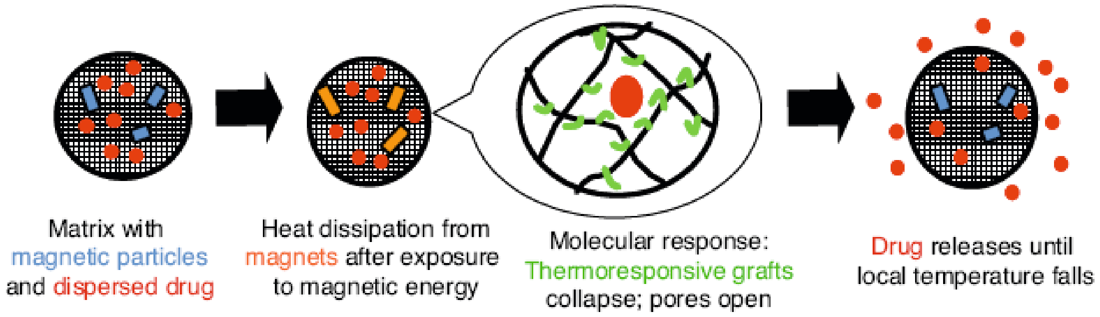

Figure 2.24: Depiction of magnetothermal responsive delivery system using a grafted hydrogel structure[82].

2.3 Self-assembly technique for devices fabrication

2.3.1 Aluminum anodization

2.3.1.1 Self-organized AAO

Anodizing, an electrolytic passivation process, is often used to increase natural oxide thickness on the surface of metal such as Ti, Zr, Al, Hf and other metals or alloys. Oxide formed in such a process tends to be readily dissolved preferentially in electric-field concentrated area, i.e. on the concave surface region where electric field is stronger than that in the flat or convex area. Multiple pores thus nucleate and grow at these concave sites that are initially provided by the random surface corrugation. In the same way, oxide growth is also electric-field dependent, basically assisted by field-assisted migration of anions (O^{2-}, OH^-) and cations (Al^{3+}), and reaction among them. The balance between the electric field enhanced oxide dissolution at the electrolyte/oxide interface and oxide formation at oxide/metal interface is essential to the formation of proper nanoporous AAO because it enables the barrier thickness to be constant over the entire anodizing process resulting from constant anodic current flow, and thus leading to a steady-state vertical pore propagation into underlying Al substrate as schematically illustrated in Figure 2.25.[89-91]

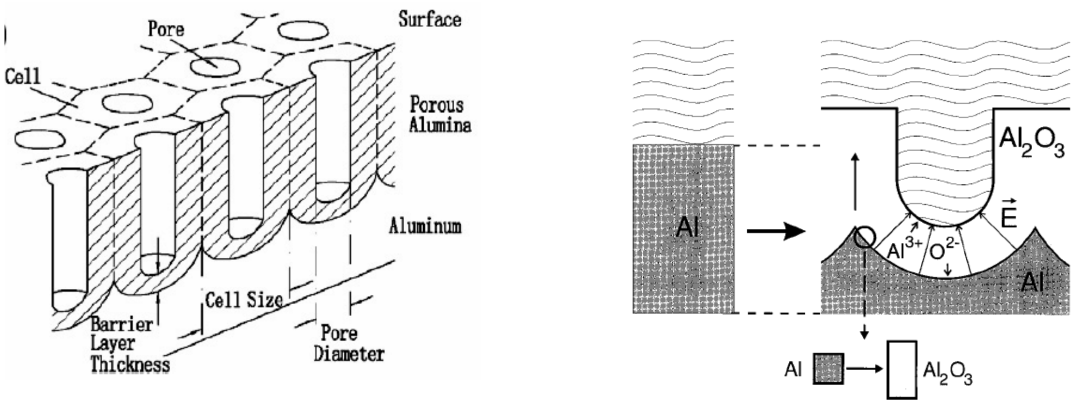

Figure 2.25: Schematic diagram of (a) porous alumina with structural parameters[92] and (b) volume expansion of Al during anodic oxidation. Existing pore walls are pushed upwards.[91]

Either bulk Al or Al thin film can be anodized in principle. However, deposited thin Al films usually have much smaller grain sizes compared with polycrystalline bulk foils, and the anodization order development is often disrupted by the randomly-distributed, densely-spaced grain boundaries from the initial stage of pore formation. As such, a high-quality growth of well-ordered pore arrays on thin film aluminum has remained as one of the major challenges, especially as the pore size gets smaller toward further nano-dimensions.[93]

It is well known that ordered porous AAO can be obtained in various processing windows.[94-102] Masuda and co-workers reported ordered porous AAO in several self-ordering regimes, i.e., 25V in sulfuric acid, 40V in oxalic acid, 195V in phosphoric acid as shown in Figure 2.26. In addition, Gösele and co-workers recently reported new self-ordering regime as shown in Figure 2.27: 110~140V in malonic acid and 110~150V in oxalic acid, which drew renewed attention to hard anodization (HA) process typically associated with high anodic currents[98-102] and often leading to formation of unique nano-array structures, which will be further discussed in Chapter 2.1.3 and 2.1.4.

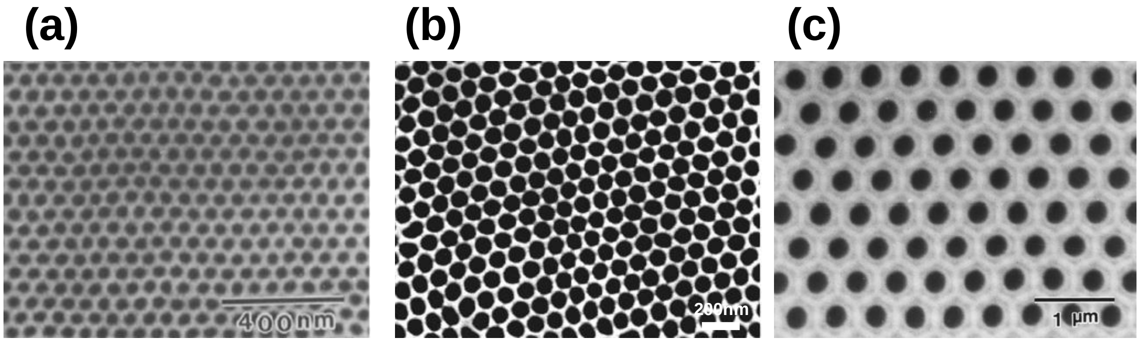

Figure 2.26: SEM micrographs of self-ordered porous AAO (mild anodization) in various dimension anodized at: (a) 25V in sulfuric acid,[95] (b) 40V in oxalic acid,[97] and (c) 195V in phosphoric acid.[96]

In the case of conventional porous AAO, hexagonally ordered AAO pores are vertically grown in the underlying Al substrate under the well-known self-assembly condition as discussed above. The pore channels are straight and parallel to each other, and the bottom of each vertical pore is closed with hemispherical end (Figure 2.27(a)) that forms continuous oxide layer over the whole anodized area, which is known as a "barrier layer".[103] Shown in Figure 2.27(c) are well-summarized self-ordering regimes of AAO reported so far.

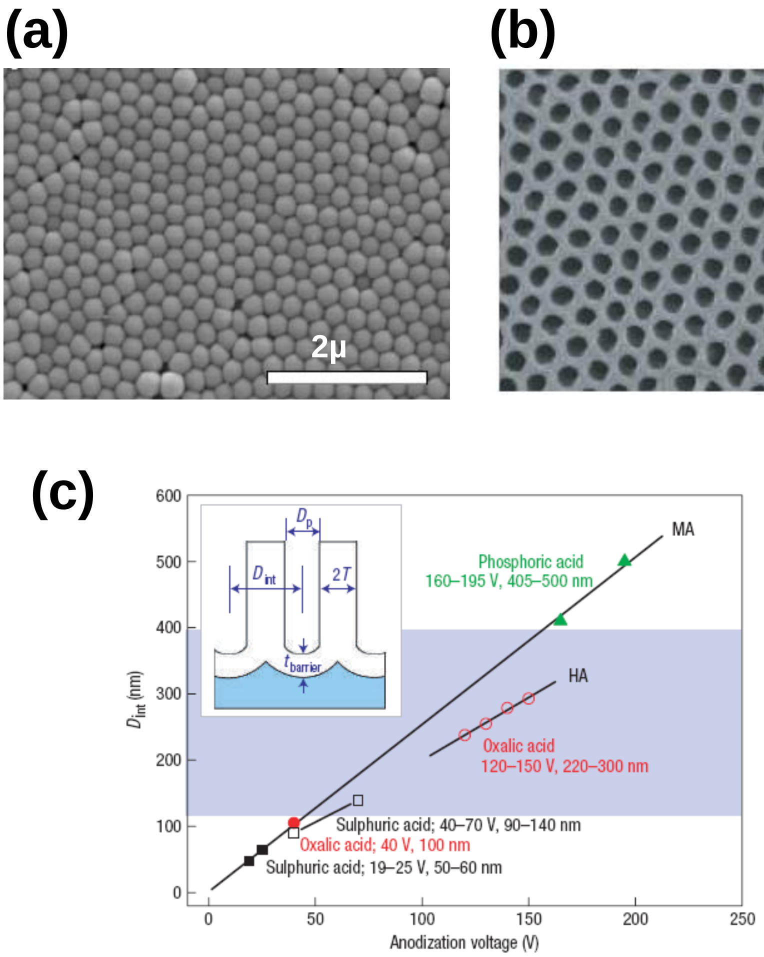

Figure 2.27: SEM micrographs of recently found self-ordered porous AAO (hard anodization) in various dimension anodized at: (a) 140V in malonic acid (barrier layer),[98] (b) 140V in oxalic acid,[99] and (c) graphical summary of self-ordering regime reported.[99]

2.3.1.2 Self-ordering phenomena

Most commonly cited factors for self-organized AAO are anodizing voltage, current density, species of electrolyte used and its concentration, and anodizing temperature. Since these factors are correlated each other, the role of each parameter should be taken into consideration to understand the underlying overall nanopore formation mechanism.

Applied voltage is one of the most important parameters to determine geometric AAO dimensions such as pore diameter and interpore distance (or cell size). The effect of applied voltage has been shown empirically and theoretically[89, 103] and the valid relationship between applied voltage, V_{app} and interpore distance, D_{int} or pore diameter, D_p can be expressed as:

$$D_{int} = 2.5V_{app} \tag{2-18}$$

$$D_{int} = 2\,D_p \tag{2-19}$$

This relationship is valid as long as a relatively small anodic current is evolved. However, if the high current evolves under unstable anodic process conditions such as high electrolyte concentration, elevated temperature and high applied voltage, the effect of current density should be taken into account. In addition, it is noteworthy that a pore widening step after anodization can change pore diameter while maintaining the cell size constant.

Highly ordered AAO could be associated with high current evolution, directly related to high electric field across barrier layer near the pore bottom. The current density during anodization is dependent on various parameters and the applied electric field, i.e.,

$$j = j_0 \exp(\beta E) \tag{2-20}$$

where both j_0 and β are temperature- and material-dependent parameters and E is the effective electric field.[104] Increasing applied voltage at a given electrolyte raises effective electric field at the pore bottom, which accelerates more ionic species movement through dielectric barrier and, in turn, current flows catastrophically at those areas, thus leading to dielectric breakdown.[105] Therefore, these aspects should be taken into account especially in hard anodization, which typically involves high current flow during ordered AAO formation.

As experimentally demonstrated by Lee et al., current density, i.e. the electric field strength at the pore bottom, is an important parameter governing self-ordering phenomena, specifically in hard anodized AAO.[98, 99] They proposed that repulsive forces between oxide cells under high electric field strength, associated with high mechanical stress at the metal/oxide interface due to volume expansion, are the main driving force for the well developed self-organized formation of ordered hexagonal pore arrays.

The selection of proper electrolyte is important and oxygen element containing acids are generally under consideration for porous type AAO formation. Depending upon pore dimension and morphology, frequently utilized electrolytes are sulfuric acid, oxalic acid, phosphoric acid and the mixed solution of these.[106] Other electrolytes such as malonic acid and citric acid were also reported.[98]

Electrolyte temperature controls not only oxide growth rate (kinetics) but also influences uniform oxide formation (morphology). As temperature decreases, growth rate decreases but more uniform oxide layer forms. To reduce Joule heating owing to large current evolution specifically under hard anodization, negative temperature below 0℃ with ethanol addition in aqueous electrolyte is often used for efficient heat dissipation, since the freezing point of ethanol is lower than that of water so that aqueous electrolyte can be cooled down somewhat below 0℃. Moreover, latent heat dissipation occurred when ethanol evaporates further preventing or minimizing local event which otherwise would be often encountered in HA. Therefore, it is important to determine the appropriate anodizing temperature window range to balance the growth rate and the quality of oxide film.

The porosity in AAO, generally considered as constant (10% porosity rule) in mild anodization condition regardless of electrolyte and anodizing voltage,[107] can be a factor in modified anodizing conditions in the course of releasing mechanical stress accumulated due to fast oxide growth. Moreover, stirring of the electrolyte helps AAO to be better ordered since the concentration profile along pore axis is influenced by electrolyte agitation.[108]

Also, an addition of Al-containing salts or aging of electrolyte prior to the main anodization steps might be a factor in certain process conditions as demonstrated by Chu et al. although its effectiveness is still being debated.[99, 109]

On the other hand, the effect of alloying element in pure Al is of interest for economic point of view since Al alloy is easier to obtain and cheaper than pure Al in industrial point of view. For some applications, Al alloys with other physical or chemical properties are preferred to pure Al. In these aspects, anodization of Al alloys should be also investigated further for spontaneous self-ordered AAO formation.

2.3.2 Block copolymer

Block copolymers (BCPs) comprise two or more homopolymer subunits linked by covalent bonds. The most important applications of block copolymers are based on the thermoplastic elasticity created by microphase separation in triblocks and multiblocks and the surfactant-like behavior of diblocks and graft blocks when blended with homopolymers.

The phase behavior of BCP is primarily determined by the following parameters: the overall degree of polymerization *N*, the magnitude of the Flory-Huggins segment-segment interaction parameter χ, the volume fraction of type-A repeat units *f*, and combined parameter χN, which controls the degree of segregation.[110]

Order-disorder transition occurs depending upon χN product, as shown in Figure 2.28.[111] For χN <<10, entropic factors dominate and diblock copolymers exist in a spatially homogeneous state.[112] Increasing *N* or χ shifts the free energy balance and leads to the development of local composition fluctuations[113] as depicted in Figure 2.28. When $\chi N = 10$, a delicate balance exists between entropic and energetic effects. Increasing this parameter further induces a first-order transition to an ordered state.[112, 113] In the limit χ *N* >>10, energetic factors dominate and the ordered microstructures are characterized by narrow interfaces and nearly flat composition profiles.

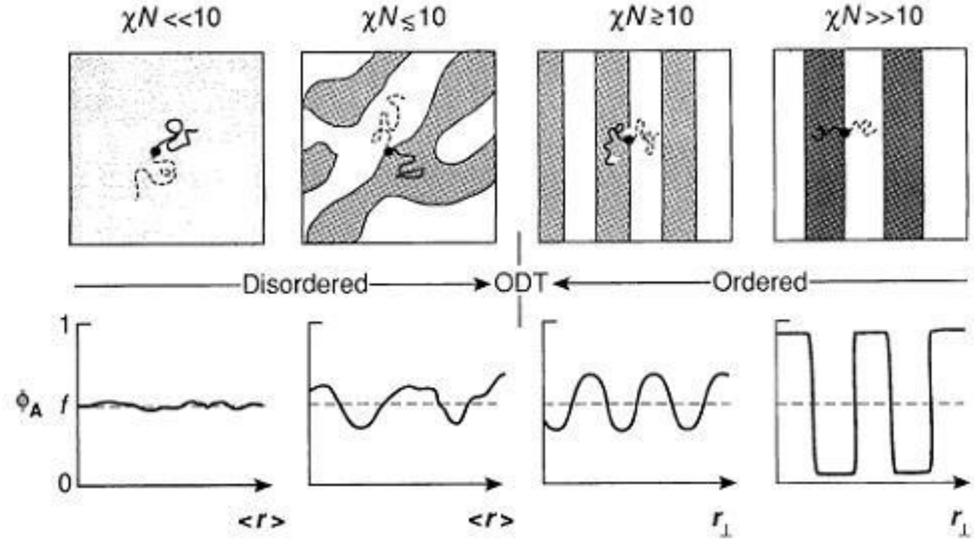

Figure 2.28: Evolution of structure with the combined parameter χN for a symmetric, di-block copolymer with $f = 0.5$. When $\chi N \sim 10$, small variations in system entropy (~ N^{-1}) or energy (~χ) leads to ordered ($\chi N \geq 10$) or disordered ($\chi N \leq 10$) states. A homogeneous composition profile (Φ_A vs r) results when entropic factors dominate (χN << 10), whereas a strongly microphase segregated pattern characterizes the limit where energetic factors prevail (χN >> 10).[111]

2.3.2.1 Self-organized BCP

For the fabrication of devices on the nanometer scale, self-organized macromolecular materials can provide an alternative pathway to conventional lithography. When necessary conditions for ordered phase segregation are met, BCPs spontaneously phase segregate and self-assemble into microphase-separated, nanometer-sized domains that exhibit ordered morphologies at equilibrium.[110, 111] The relative chain lengths of the blocks determine the corresponding BCP morphology and commonly encountered ordered morphologies in bulk samples are periodic arrangements of lamellae, cylinders, and spheres. The chains can self-assemble to form micrometer-scale domains whose size and geometry depend on the molecular weights of the types of polymer and their interaction.

One of the advantageous features of the BCP thin films is that they spontaneously form nanometer-scale patterns over a large area (albeit with some microdomain boundaries unless guiding and anchoring mechanisms are utilized), which is desirable for the applications requiring high throughput manufacturing.

2.3.2.2 Directed BCP

The self-ordered BCP film provides highly ordered pore arrays; however, micrometer-sized domain boundaries are present, which is not desirable for applications such as patterned magnetic media where perfectly arranged patterns are required to function properly. In this regard, considerable attention has been paid to lithographically directed BCP self-assembly for the realization of long-range ordered nano arrays. These directed processing offers several advantages such as cost-effectiveness, large area coverage and high throughput that stems from the inherent parallel patterning nature of self-assembly in addition to its compatibility with pre-established top-down patterning technologies. Nevertheless, the pre-patterning method is an extra step that introduces a lithographic step, nominally at the same feature density as that achieved by the block copolymer.

Recently, Ruiz et al. reported successful demonstration of directed BCP self-assembly with advantageous features of both pattern rectification and multiplication on substrate pre-patterned by e-beam lithography as shown in Figure 2.29.[114] They claimed that nonuniform e-beam patterns could be further improved in terms of pattern uniformity as shown in Figure 2.29(b) (E, G) and, furthermore, sparsely defined e-beam patterns acted as anchors for the subsequent BCP pattern orientation, thus leading to increased pattern density and dimensional uniformity over large area.

On the other hand, Park et al. found macroscopic ordering of PS-b-PEO self-assembly on a faceted sapphire substrate as shown in Figure 2.30.[115] They used surface reconstructed sapphire single crystal as a substrate formed upon heating and the successive cooling. Perfectly aligned BCP thin films were formed in a relatively various M_n values, which is advantageous for tailoring of the pattern density.

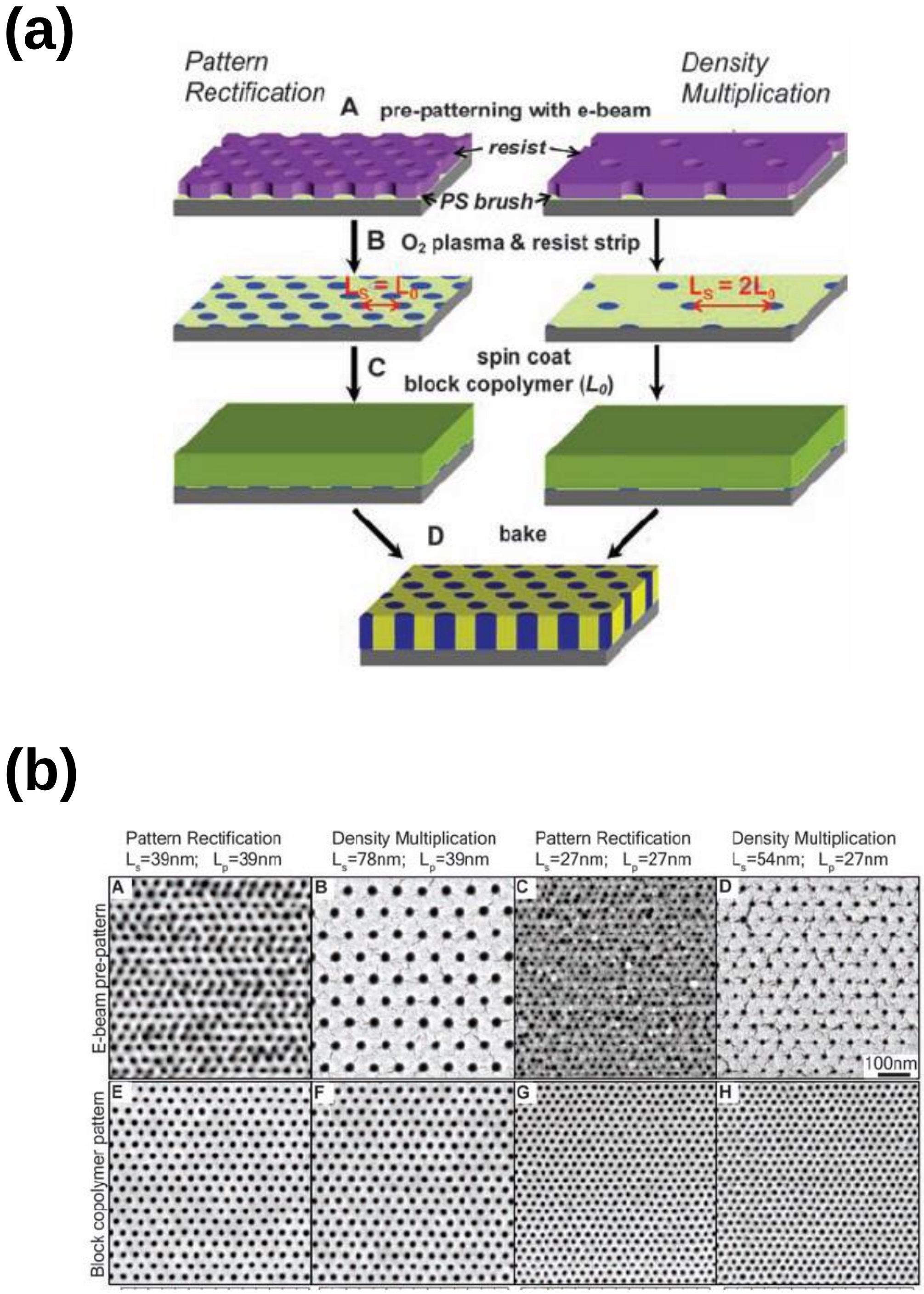

Figure 2.29: Representative guided BCP array of PS-*b*-PMMA on an e-beam patterned PS/SiO$_x$ substrate: (a) schematic fabrication process (A-D) and SEM images of e-beam pre-patterns (E) and BCP patterns by means of density multiplication (F), and (b) SEM images of developed e-beam resist (A-D) and the block copolymer film (E-H) on top of the prepattern defined by the corresponding e-beam pattern above.[114]

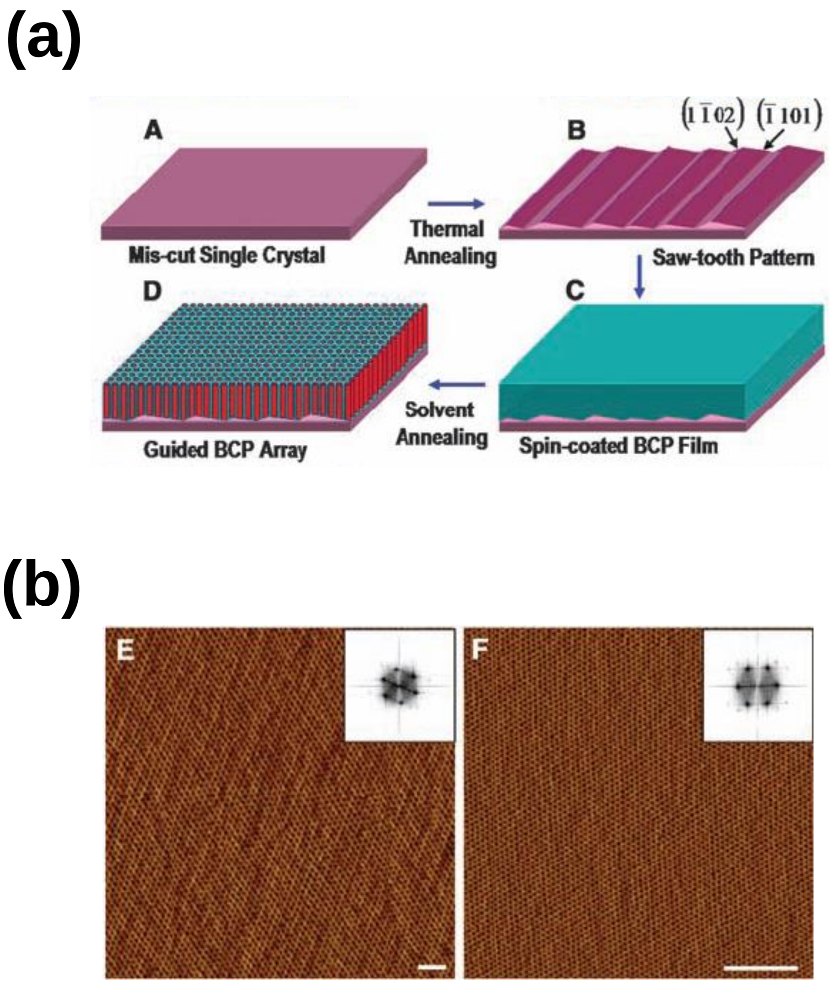

Figure 2.30: Representative guided BCP array of PS-*b*-PEO on highly oriented crystalline facets on a single crystal sapphire: (a) schematic fabrication process (A-D) and (b) AFM phase images of BCP having different M_n, (E) 25.4kg/mol and (F) 7.0kg/mol.[115]

CHAPTER 3:

Fabrication and properties of nano-patterned graphene by self-assembled template for field effect transistor application

3.1 Introduction

Recently, graphene has emerged as a new material for its remarkable electronic properties [116]. Besides single layer graphene (SLG), two and few layers graphene (FLG) are of interest for future device applications [117]. Electronic transport in graphene is dramatically different from that of a conventional 2D material since energy dispersion of electrons linearly scales with momentum near Dirac point [42]. A high electron mobility value such as 200,000cm^{2}V^{-1}s^{-1} was observed in suspended graphene sheets [5]. Thus, its superior mobility over silicon makes it a promising candidate for the future electronic devices. However, due to the semi-metallic nature of graphene it lacks a bandgap, which is necessary for technological applications such as field effect transistors (FETs). Hence, this results in a very low on/off ratio in graphene field effect transistor (GFET) devices. For practical applications, an on/off ratio on the order of 10^5 is needed. One way to open a bandgap in graphene is to create geometrical constrictions of graphene material. This will lead to confinement of electrons, thus opening a bandgap. A bandgap opening up to 200 meV has been observed in graphene nanoribbons (GNRs) fabricated by lithographic methods [33]. However, this requires expensive fabrication methods and the driving current is very low in such nanoribbon structure.

In order to increase the driving current for practical applications, the fabrication of dense, ordered nanoribbon arrays is required, which has been achieved by electron-beam lithography [64, 118]. Although conventional lithographic methods can provide precisely located nanoarrays, the size of the area that can be patterned is often limited to the micrometer scales due to its intrinsic time-consuming nature of serial processing in addition to the limited processing resolution. Sinitskii and Tour [119] used nanosphere lithography to prepare a porous metal film, which was then employed as an etch mask for fabrication of graphene nanomesh (GNM), however it had unsatisfactory geometrical dimensions. As an alternative, self-assembly nanoarrays have been extensively investigated, such as block co-polymer (BCP), anodized aluminum oxide (AAO). One of the most fascinating properties of self-ordered nanoarrays lies in the readiness of its fabrication on length scales that are difficult to obtain by standard semiconductor lithography technique [120]. Liang et al. combined the self-assembly of block-copolymers and nanoimprint lithography to prepare GNM with neck width (*w*) down to less than 10 nm, but the template preparation process is complicated [121].

Recently, Kim et al. reported the fabrication of nanoperforated graphene materials with sub-20-nm features using cylinder-forming BCP [122]. In that work, the nanoperforated graphene is semiconducting in behavior with an effective energy gap of 100 meV, but a 10 nm thick cross-linked P(S-*r*-MMA-*r*-GMA) neutral layer between P(S-*b*-MMA) template and graphene is additionally needed. Moreover, P(S-*b*-MMA) is well known to undergo phase separation in thin films when annealed only at temperatures above the glass transition temperature (T_g) of both polymers [123, 124]. However, sometimes annealing causes the problem of macrophase separation in BCP, which reflects that small molecules crystallize out of BCP [125]. Ikkala and co-workers pointed out that extensive annealing at elevated temperatures can cause macrophase separation in their BCP [126]. The Poly(styrene-*b*-4-vinylpyridine) (PS-*b*-P4VP) has high Flory-Huggins interaction parameter, which is expected to minimize edge roughness and scalable for producing densely periodic arrays and highly selectivity between the two blocks. Thermal annealing or solvent vapor annealing can induce ordered micro-phase separated structures in PS-*b*-P4VP. Solvent annealing process is useful in the processing of BCP films because orientation can be controlled by evaporation rate and the high residence time of solvent in the film, which can provide enough polymer mobility to attain long-range structural order.

Here, we report the production of a graphene nanostructure that can open up a bandgap in a large sheet of SLG and FLG. While extensive studies have been carried out on the physical properties of SLG, less is known about the electrical properties of FLG structures. We focus on experimental investigations in SLG and FLG FETs and the implications for the device performance. The patterned graphene is prepared using a block copolymer lithography using PS-*b*-P4VP which is the first ever demonstrated for graphene application to our knowledge. Such nanostructuring process can effectively open up a conduction bandgap in a large piece of graphene. The fabrication of nanopatterned graphene (NPG) using block copolymer approach allows easier and scalable fabrication of nanoscale pores in graphene on a SiO_2-coated Si substrate. The block copolymer lithography fabrication of patterned graphene can therefore enable a continuous semiconducting graphene thin film for flexible electronics, nanoelectronics, and optoelectronics [38].

3.2 Methods

3.2.1 Synthesis of large scale graphene

Graphene was synthesized using thermal chemical vapor deposition (CVD) of methane (CH_4) at 1000 °C. A thin Cu foil (25 μm thickness) was purchased from Alfa-AESAR, USA and cut in 20 mm × 13 mm size and annealed at 1000 °C for 1 h in an inert gas atmosphere followed by hot acid treatment and cleaning. After that the metal foil was placed inside a thermal CVD system and the temperature was increased up to 1000 °C with a heating rate of 120 °C min^{-1}. The atmosphere of the CVD furnace was maintained at 0.8 atmospheric pressure in the presence of an inert gas (Ar) and CH_4 : H_2 (1 : 4) was used as a precursor gas mixture for graphene growth. Before graphene on Cu was transferred to substrate, the back side graphene was removed by oxygen plasma. The top side graphene was protected by a Poly methyl methacrylate (PMMA) layer during the O_2 plasma etching. The graphene film was then transferred onto a 300 nm SiO_2 coated Si substrate (Si/SiO_2) using a chemical process. The chemical process for graphene transfer consists of the etching of Cu foil and then transferring the floating graphene onto a Si/SiO_2 substrate, followed by washing with water, acetone, and isopropyl alcohol as described elsewhere [117]. After that, the PMMA layer was removed by dissolving it in acetone. Furthermore, the rapid thermal annealing was carried out for graphene on the Si/SiO_2 substrate at 400 °C under a N_2 atmosphere to remove the residual PMMA and promote the adhesion between graphene and the oxide layer.

3.2.2 DBCP Film Fabrication

The patterned structure was made by di-block copolymer self-assembly. Poly(styrene-b-4-vinylpyridine) (PS-*b*-P4VP) (number-average molecular weight, $M_{n,PS} = 41.5$ kg/mol, $M_{n,P4VP} = 17.5$ kg/mol, Mw/Mn = 1.07, where Mw is the average molecular weight) was purchased from Polymer Source (Montreal, Canada) and used without further purification. A 20 nm thick silicon oxide film was deposited onto graphene as the protecting layer and also as the grafting substrate for the subsequent block copolymer nanopatterning. Then, 0.5 wt. % PS-*b*-P4VP copolymer solution dissolved in toluene was spin-coated at 2,000 rpm for 60 sec on substrate. This film was then exposed to tetrahydrofuran (THF) vapor in a closed glass vessel for 3 h to induce mobility and allow phase separation to occur. The film was then immersed in pure ethanol for the poly(4-vinylpyridine) (P4VP) phase to swell, thus leading to a porous structure. The PS-*b*-P4VP block copolymer thin film with cylindrical domains normal to the surface was then fabricated and used as the etching template, and a reactive-ion etch (RIE) process is used to punch holes into the graphene layer.

3.2.3 Preparation of AAO Membrane

A 0.5mm thick annealed Al foil purchased from Alfar aesar (99.99%) was used as the starting material. The Al foil was successively degreased by acetone and isopropyl alcohol with ultrasonication, followed by deionized (D.I.) water rinse and nitrogen gas blow. The Al foil was slightly etched in 1M NaOH aqueous solution to remove any possible surface contaminations prior to surface smoothing electropolishing process conducted at 20V in a solution of perchloric acid (70%) and ethanol (99.9%) (1:4 volume ratio) at 5℃ for 15 minutes, using a Pt counter electrode. Then, a two-step anodization process of the Al foil was carried out by incorporating the Al foil as the working electrode and Pt as the counter electrode, immersed in 0.3 m oxalic acid. The electrolyte temperature was maintained at 1℃ during anodization process using a powerful refrigeration bath (RTE7, Thermo Scientific) in which the coolant circulates double-wall glass chamber. After the first anodizing process, which took about 3 hours at an operating voltage of 40 V, the anodized Al foil was immersed for 1 hour in a mixed solution of phosphoric acid (6 wt%) and chromic acid (1.8 wt%) kept at 75℃ to remove the alumina layer formed in the first anodizing step. The second anodizing step was implemented for 10 minutes while other experimental conditions were unchanged compared with the first anodizing step, in order to form an ordered porous alumina membrane on the Al foil. Then, the Al metallic substrate underneath the AAO layer was selectively removed with a mixed HCl and $CuCl_2$ solution for 10 minutes. Any residual Cu debris adhered to the bottom of the AAO barrier layer was removed by placing the sample in nitric acid for a few seconds and washed in D.I. water immediately after. The barrier layer in the bottom of the AAO holes was then removed by 5 wt% phosphoric acid etching for 10 minutes to two hours.

3.2.4 Formation of the Porous Graphene

For efficient nanopatterning, two consecutive RIE processes were applied. As a shallow depth hole generation in graphene, no additional deposition to enhance RIE resistance was applied prior to the RIE process. The first RIE etching was for P4VP residual layer removal located at the bottom of holes. RIE process parameters were empirically determined by using CF_4 gas (Oxford Plasmalab 80 RIE) and optimized at 50 mTorr under 65 W, plasma power for 30 s. The latter was to create shallow prepatterns on SiO_2 thin film exposed to air formed at the previous RIE step and optimized at 40 mTorr under 200 W with CHF_3 and Ar gases. An O_2 plasma process was then used to remove remained copolymer. CHF_3 and Ar plasma was then used to punch holes into the evaporated SiO_2 to expose the underlying graphene layer. The prepared AAO template floating in water was placed on the graphene as an etch mask by lifting up the Si/SiO_2 substrate from underneath. After that, the sample was annealed in vacuum at 180℃ for 2 h, in order to allow the AAO membrane to stick tightly on the graphene surface. Then, oxygen plasma (30 W, 150 mTorr) was applied through the AAO template holes to etch and create pores on the graphene. The details of recipes and procedures for formation of NGP were explained in previous study [127]

3.2.5 Characterization

The sample microstructure was characterized by ultra-high resolution scanning electron microscopy (UHR SEM; FEI XL30). Raman spectroscopy was used as a nondestructive tool for probing the edge structure and the crystallinity of sp^2-bonded graphene [128, 129] Raman Spectra was collected using a Renishaw Raman Spectrometer inbuilt with Ar^+ laser of wavelength of 514 nm for quantifying the degree of structural order and charge transfer characteristics.

3.3 Results and discussion

3.3.1 NPG FET using BCP

Figure 3.1 illustrates the present approach for fabricating NPG. For initial demonstrations, the CVD grown graphene layer on Cu foil was used as the starting material. After Cu was etched away by 1M $FeCl_3$, the floating graphene was transferred onto SiO_2 on Si. A 20-nm thick silicon oxide film is first evaporated onto graphene as the protecting layer and also as the grafting substrate for the subsequent block copolymer nanopatterning. The PS-*b*-P4VP block-copolymer film with cylindrical domains normal to the surface is then fabricated and used as the etching template, and a CHF_3 based RIE process followed by oxygen plasma etch is employed to punch holes into the graphene layer. We present the first experimental study on nanopatterning with PS-*b*-P4VP in SLG and FLG FETs.

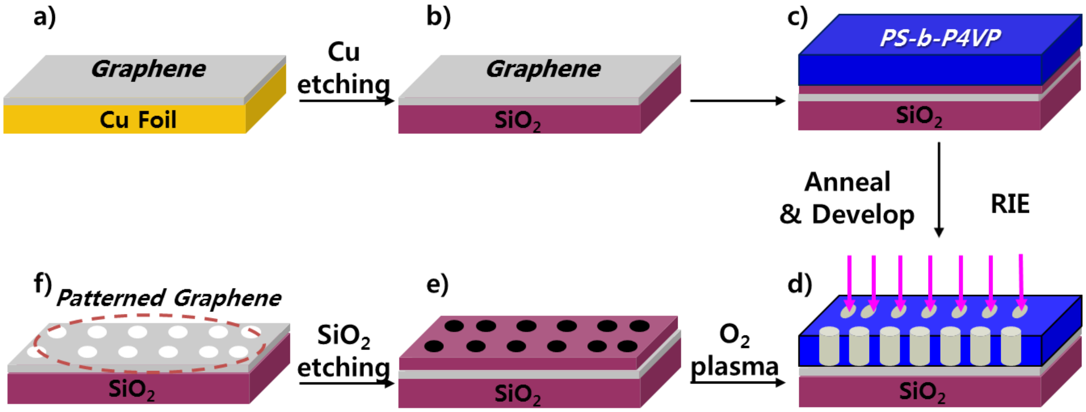

Figure 3.1: Schematic of fabrication of a nanopatterned graphene. (a) CVD grown graphene on Cu foil, used as a starting material of the nanopatterning process. (b) After Cu was etched by using 1M $FeCl_3$, the graphene was transferred onto a SiO_2/Si substrate (c) A thin layer of SiO_2 is deposited on graphene followed by the spin-coating of the block-copolymer PS-b-P4VP on top of it. (d) The PS-b-P4VP block-copolymer film is annealed and developed, leaving the porous PS matrix as the template for further patterning. (e) Fluoride-based reactive ion etching (RIE) to penetrate the oxide layer, partially degrade the PS film, and form the SiO_2 hard mask. (f) Graphene in the exposed area was etched away by O_2 plasma and then SiO_2 was removed. Finally, porous graphene on SiO_2 was obtained.

Raman spectroscopy was used as a nondestructive tool for probing the edge structure and the crystallinity of sp^2-bonded graphene. Figure 3.2 demonstrates the Raman spectra of pristine graphene, and NPG. The Raman data was taken from different spots on graphene. Prior to patterning, the G (～1580 cm^{-1}) and 2D (～2680-2700 cm^{-1}) bands were prominent. Raman spectroscopy can also be used to determine the number of layers of multilayer graphene and to discriminate between single and few layers using the intensity ratios of G band and 2D band. For a single layer graphene, I_G/I_{2D} intensity ratio is ~0.24 which increases with the number of graphene layers thus making it possible to estimate the thickness of graphene layers [117, 130]. In this regard, it is well known that the I_G/I_{2D} ratio increases up to 6–8 layers. Figure 3.2 shows that the ratio of I_G/I_{2D} in our graphene is around 0.7 and it can be estimated to 4~7 layers of graphene [130]. In addition to the differences in the I_G/I_{2D} ratio, the full width half maxima (FWHM) of 2D band increases as the graphene thickness increases [131]. The shape of the 2D mode evolves significantly with the number of layers. The 2D band becomes broader when the graphene thickness increases from single to multilayer graphene. As the 2D band originates from a two phonon double resonance process, it is closely related to the band structure of graphene layers. Ferrari et al. [129] have successfully used the splitting of the electronic band structure of multilayer graphene to explain the broadening of the 2D band. For mono and bi layer graphene, the FWHM of 2D band is ~30 [7] and for FLG in our data, it is ~63.24. We believe that the 2D peak broadening can be attributed to the number of layer increases in graphene structure [132]. The D peak at ~1330 cm^{-1} is related to defects and disorder. This is forbidden in perfect graphitic systems and requires a defect for its activation, and so is observed at the edges of graphene samples [58, 133]. The integrated intensity ratio of the D band and G band (I_D/I_G) is a parameter sensitive to defect density [134, 135]. In Figure 3.2, the high D peak was observed on porous graphene, which suggests that defects in our sample are significantly formed by nanopatterning. After nanopatterning, there is a systematic upshift in the position of G band. The G band position for porous graphene was observed at ~1586 cm^{-1}, which can be compared with the G position of pristine graphene (~1580 cm^{-1}). This upshift in the G band position further confirms the hole-doping in the NPG by the formation of oxygen dangling bonds with graphene as reported earlier [132]. We also note that there is a increase in intensity ratio of the I_G/I_{2D} with more defects. The increase in I_G/I_{2D} in NPG is due to the alteration of its electronic transformation from semi-metallic to semiconducting with successive opening of band-gap [131, 136]. The detail explanations of change in electronic structure of NPG by band gap opening is discussed in the latter section of this manuscript.

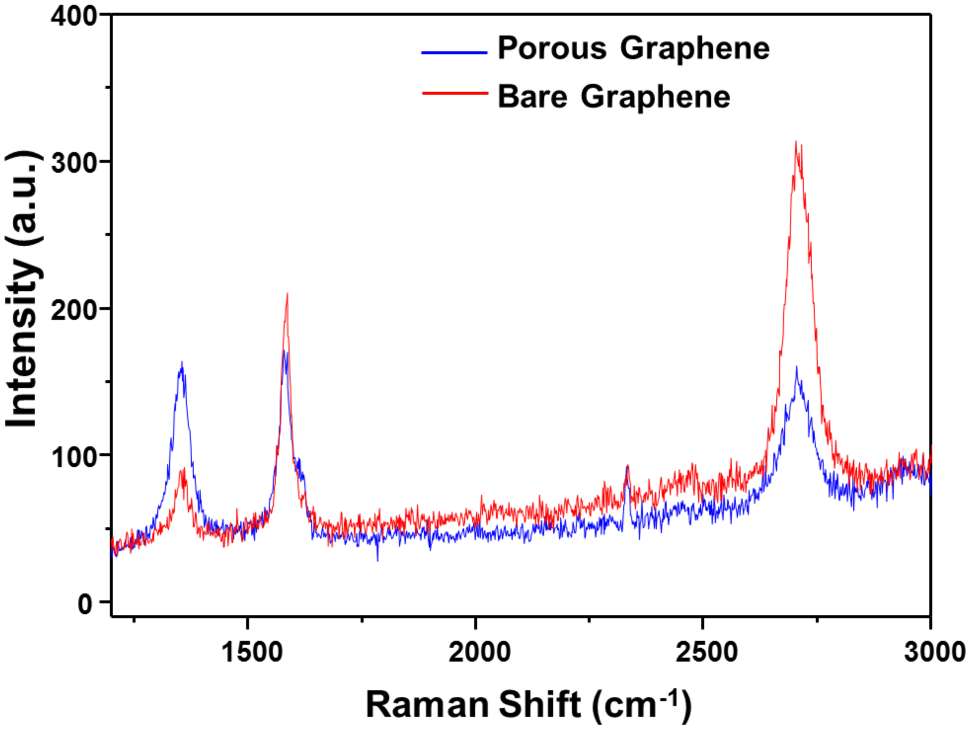

Figure 3.2: Comparison of Raman spectra of pristine and nanopatterned graphene with their characteristic D, G, and 2D bands at the respective positions.

Figure 3 shows the image of the steps of nanopores fabrication on graphene. Scanning electron microscope (SEM) image of the annealed block-copolymer film on graphene shows the hexagonal-packed P4VP domains in the PS matrix. The sample was immersed into ethanol for 20 min to develop the porous structure (Figure. 3a). The domain center-to-center distance is approximately 48.3 nm ± 2.7 nm by using PS-*b*-P4VP with number-average molecular weight, $M_{n,PS} = 41.5$ kg mol^{-1}, $M_{n,P4VP} = 17.5$ kg mol^{-1}. Changing the molecular weight while keeping the volume ratio constant can result in vertical aligned domains with variable center-to-center distance. We used RIE in order to remove P4VP domains, which causes a porous structure of PS matrix with hexagonally arranged nanoholes vertically penetrating through the film as shown in Figure 3a.

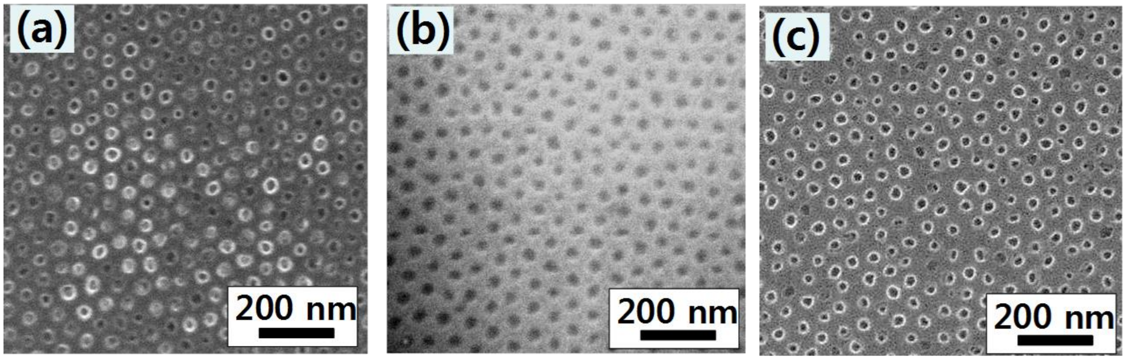

Figure 3.3:. Images illustrating the steps of the nanopatterened graphene fabrication process. (a) SEM image of the annealed block-copolymer film on graphene, showing hexagonal-packed P4VP domains in the PS matrix. The sample was immersed into ethanol for 20 min to develop the porous structure. (b) SEM image of the SiO_2 mask after reactive ion etching with the PS mask. (c) SEM image of the NPG surface after removing the top SiO_2 mask (high magnification). The pores have 29.14 nm ± 2.54 nm diameters and 19.16 nm ± 2.25 nm neck widths after removing the top SiO_2 mesh mask.

The following etching process begins to drill holes into the underlying SiO_2 layer, leaving a SiO_2 nanomesh that can serve as the mask for subsequent oxygen plasma etch to form porous graphene (Figure 3.3b). The oxide mask can be easily removed by dipping the sample into etching solution for a short period of time and the NPG structure can be seen under SEM. Figure 3.3c show the SEM images of a porous graphene with average neck width (*w*) of ca. 19.1 nm, but a neck width as small as 5.6 nm were also observed. Furthermore, it is possible to tune the mesh periodicity by using block copolymer of different molecular weight [137]. By applying longer etching time to remove graphene, neck width can be further reduced for creating the quantum confinement effect to open up an effective band gap [138]. As the neck width represents the smallest dimension that controls charge transport through the system, we have carried out statistical analysis of the neck widths of the NPG obtained after SiO_2 etching (Figure 3.3c).

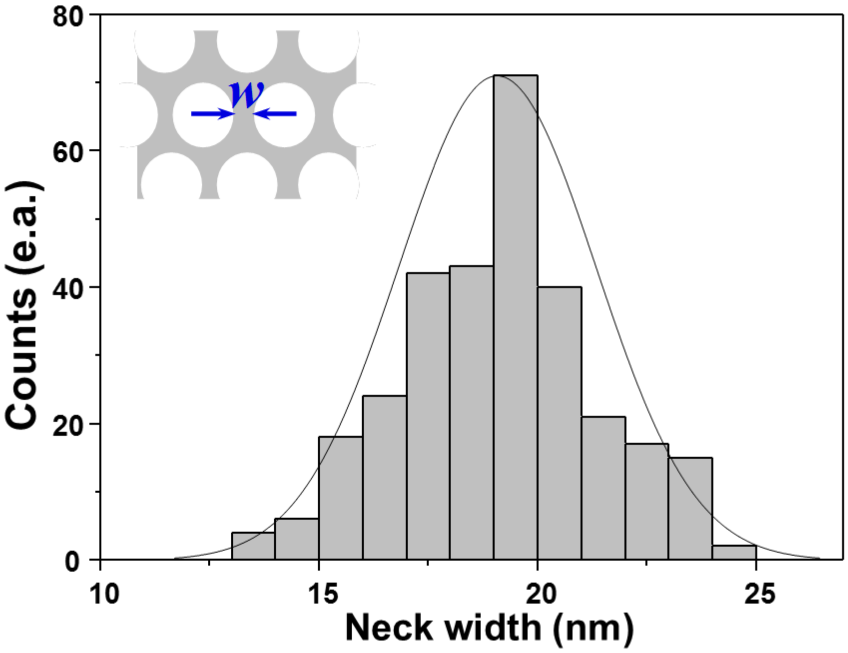

Figure 3.4: Histogram of the neck width. This plot shows a distribution of graphene neck width in the NPG of with average neck widths of 19.162 nm (*std. dev. ±2.250 nm*).

The histogram plot (Figure 3.4) resulted from the statistical analysis shows that the NPGs exhibit an average neck width of 19.1 nm and the standard deviation of the neck width is found to be less than 3 nm. However, we note our block copolymer assembly process is not yet optimized to the best it can offer, and the optimization of the block copolymer self-assembly can lead to more uniform porous graphene, as well as a further reduced neck width. It is envisioned that a pore widening process, such as utilizing a controlled oxygen plasma etch, could be utilized, which can lead to a substantially reduced neck width and associated interesting change in the degree of bandgap opening. These SEM studies together with previous studies [115] clearly demonstrate that highly uniform porous graphene can be obtained with controllable periodicities and neck widths by using the block copolymer nanolithography.

Figure 3.5 displays the electrical characteristics of field effect transistors (FETs) in NPG at room temperature. Figure 3.5a schematically illustrates the structure of patterened graphene FET device, in which a rectangular-shaped patterened graphene with neck width *w*, total channel width *W*, and channel length *L* serves as the conduction channel. A pair of metallic pads (Ti/Au) serves as drain and source contacts, similarly, a 300-nm thermal oxide SiO_2 layer and degenerated (p^{++}) Si wafer are used as the gate dielectric and the back gate, respectively. Figure 3.5c and d show the electrical transport characteristics of a typical patterned graphene transistor with averaged neck width of ~19 nm. Drain current (I_d) versus gate voltage (V_g) characteristics for the transistor show a typical p-channel transistor behavior (Fig. 3.5c and d). The increase in p-doping is likely due to increase in oxygen plasma exposure, resulting in dangling bonds on the edges of the holes [138]. In all the devices fabricated using the buffer layer process, the unintentional severe doping by CHF_3 RIE processes observed is reported in other studies [138]. The hole doping observed in the NPG is similar to that of graphene nanoribbon devices, and can be attributed to edge oxidation in the O_2 plasma process or physisorbed oxygen from the ambient and other species during the nanofabrication process.

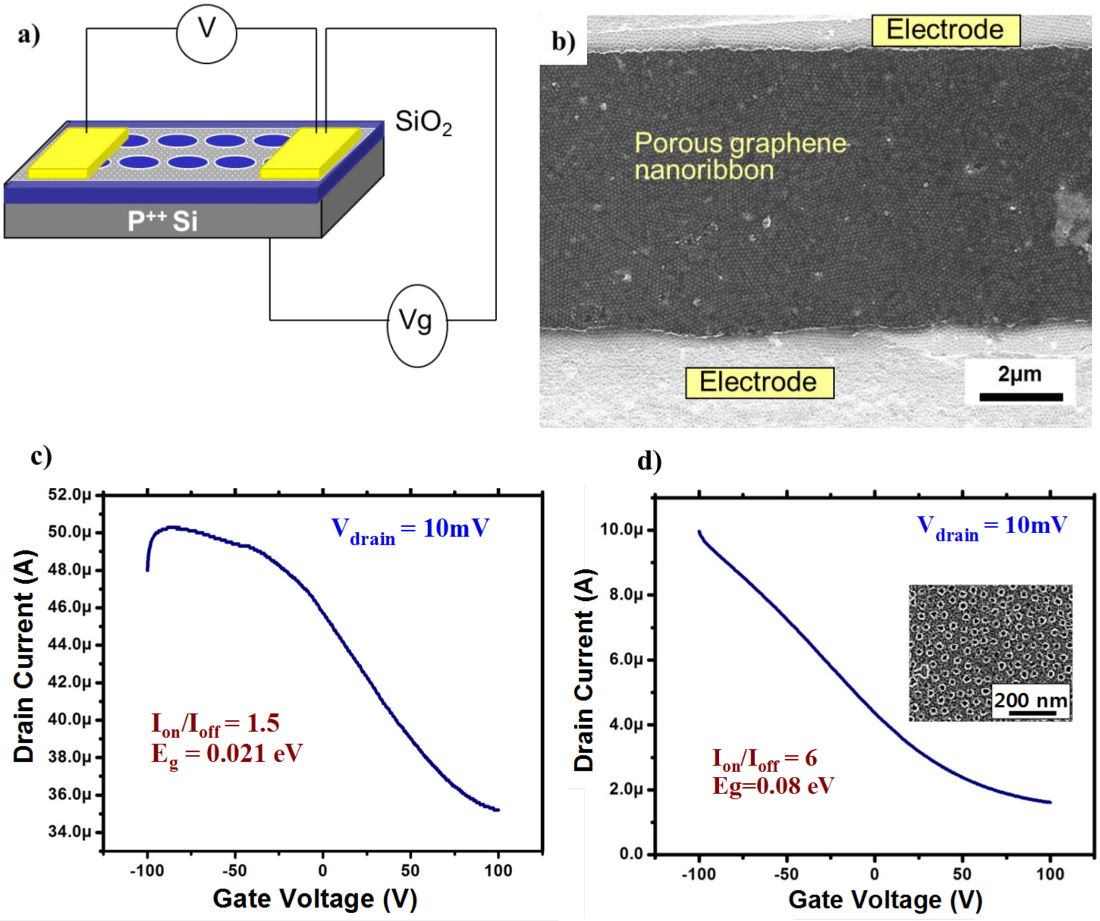

Figure 3.5: Electrical properties of nanopatterned graphene. (a) shows the schematic illustration of the FET device fabricated using the NPG. (b) SEM image shows the top-view of a nanopatterned FLG based FET device. (c) drain current (I_d) versus gate voltage (V_g) for a FET device of NP FLG. (The electronic measurement was carried out in ambient conditions at room temperature). (d) drain current (Id) versus gate voltage (V_g) for a device and Inset shows the SEM image of NP SLG.

In Figure 3.5c, this NP FLG transistor exhibits a typical ambipolar transport behavior with the minimum drain current (I_{off}) at the neutral point ($V_g = V_0$) and a relative low on/off current ratio (I_{on}/I_{off} ~1.5 measured). The ability to control the NPG periodicity and neck width is very important for controlling their electronic properties because charge transport properties are highly dependent on the width of the critical current pathway. In the case of graphene nanoribbons, both theoretical and experimental works have shown that the size of the electronic bandgap is inversely proportional to the ribbon width [30, 139, 140]. For the estimation of approximate bandgap, the NPG can be viewed as a highly interconnected network of GNRs. Therefore, we expect that the electronic bandgap of NPG inversely scales with the average ribbon width (i.e., $E_g \sim \alpha/w$, and α is a coefficient with 0.95 nm eV for nanomesh) [31, 141]. Furthermore, the on/off current ratio of a FET device exponentially scales with the bandgap (i.e., ($I_{on}/I_{off} \cdot \exp(E_g/kT)$, where k is Boltzmann constant and T is the absolute temperature) [141]. So the I_{on}/I_{off} value of NPG transistor is expected to inversely scale with the average neck width, as expressed in eq 1, where C is a dimensionless constant. Eq 1 can be simplified to eq 2 related to bandgap energy.

$$I_{on}/I_{off} \approx e^{\alpha/kT(1/w)} = Ce^{\alpha/kT(1/w)} \tag{3-1}$$

$$E_g = kT[\ln(I_{on}/I_{off}) - \ln(C)] \tag{3-2}$$

The expected bandgap from the relation of $E_g \sim \alpha/w$ by averaged neck width of ~19 nm was 0.05eV. In Figure 3.5c, however the estimated one is 0.021eV from eq 2 with measured I_{on}/I_{off} of 1.5. There is a difference between the calculated values from the relations with neck width by averaged neck width of ~19 nm and with on/off current ratio measured. Although this equation does not take into account of the entire complex physics occurring in nanostructured graphene, it is still appropriate as it meets experimental data of various NPG well [142].

While extensive studies have been carried out on the physical properties of single layer graphene (SLG), less is known about the electrical properties of FLG structures. Even we find that the electrical property in graphene nanoscale transistors is strongly affected by the number of graphene layers, the channel width, and the trapped charge in the SiO_2 substrate, consistent with the findings by Lin et al. and Sui et al. [143, 144]. Their work presented the scaling impact of the graphene thickness on the device performance and proposed a resistor network model describing the coupling between graphene layers including the impact of interlayer screening. They showed that the I_{on}/I_{off} ratio of FLG FET with respect to the graphene thickness. The I_{on}/I_{off} ratio indicates thickness^{-1} dependence and reaches unity at around 10 layers of graphene. As apparent from their work, while I_{on} decreases with thickness, I_{off} increased slowly. Thus, the I_{on}/I_{off} ratio decreased rapidly with increasing thickness of graphene and approaches to unity at or around 10 layers of graphene. This is the combined effect of the Coulomb interaction and the interlayer coupling that are responsible for the particular thickness dependence of the I_{on}, I_{off}, and on-off ratio for the FLG FETs. For NP single layer graphene (Figure 3.5d), the device also exhibits an ambipolar transport behavior and has a much higher on/off current ratio ($I_{on}/I_{off} = 6$ measured) compared to the control NP FLG transistor. Obviously, both screening and interlayer coupling is able to be considered to account for our experimental findings of the I_{on}/I_{off} dependence on the numbers of graphene layers. There are six consecutive current on/off ratio values achieved with same or a little higher than the previously reported FET devices of GNRs and GNMs [22, 145, 146]. In NP SLG FET, the calculated bandgap is 0.08 eV by eq. 3-2 and it is roughly corresponds to an expectation and the reports.

Figure 3.5d demonstrated I_D-V_g plot for the NPG devices with ~19 nm of neck width, the calculated mobility is14 $cm^2/(V·s)$, which is dramatically lower than pristine graphene. Prior to patterning, pristine CVD graphene FET devices showed a hole mobility of 500-1000 $cm^2/(V·s)$, which is typical for CVD grown graphene [147]. We calculated the hole mobility (μ) of fabricated FETs using a standard transistor model as shown in equation 3, where d_{ox} is the thickness of the gate oxide, ε_{ox} is permittivity of silicon dioxide, L is the channel length, and W is the channel width.

$$\mu = \frac{d_{ox}}{\varepsilon_{ox}} \frac{L}{W} \frac{1}{V_d} \frac{dI_d}{dV_g} \tag{3-3}$$

The reactive ion etching process is known to degrade the mobility of NPG. Moreover, because of the inherent crystal grain boundary in the CVD grown graphene as well as variations in growth directions along the crystal lattice of the catalytic metal substrate, the mobility of CVD grown graphene is typically 1-2 orders of magnitude lower than that of mechanically exfoliated graphene [147, 148]. We also observed that the grain boundaries in CVD grown graphene are essentially retained in the lattice of patterned graphene, possibly contributing to significant mobility degradation. More importantly, the mobility of NPG is limited by charge carrier scattering caused by several possible factors which include, line edge roughness, interior defects, disordered edges, ionized impurities and acoustic and optical phonons [149].

3.3.2 NPG FET using AAO

The AAO membrane prepared by two step anodization of high-purity aluminum foil exhibited locally periodic array of pores with the neck width(*w*) being ca. 29.7 nm ± 2.6 nm (Figure 3.6a). As shown in the tilted image of an AAO membrane in Figure 3.6b, the membrane thickness is ca. 200~250 nm (Figure 3.6b). This self-assembly fabricated AAO membrane was used as a mask during the oxygen plasma etching of graphene for nanopore array formation.

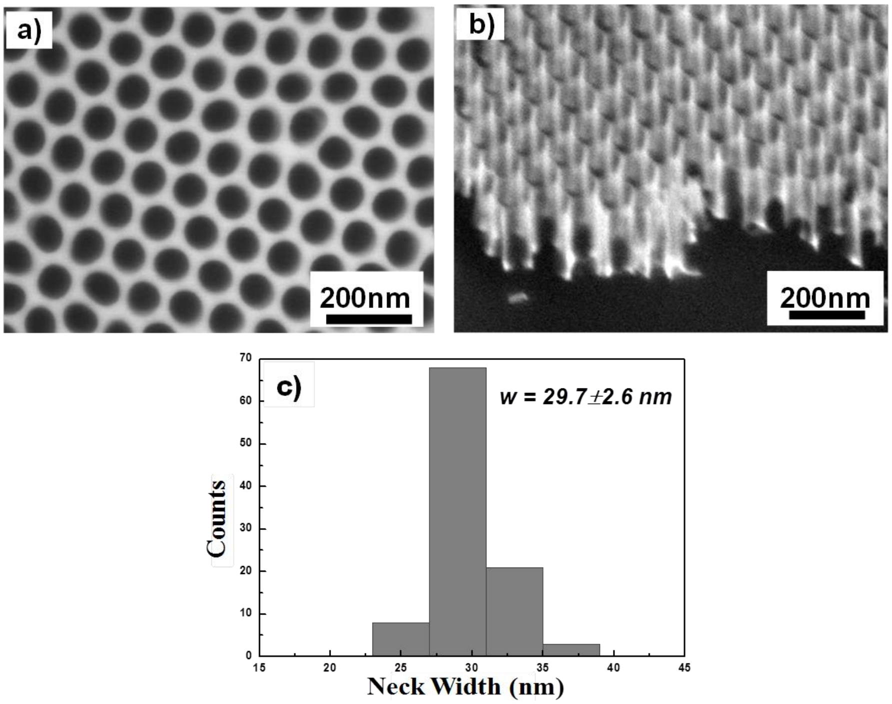

Figure 3.6: Scanning electron microscopy (SEM) images. (a) an AAO template (top view), (b) a tilted AAO membrane with ~200 nm thickness, (c) Histogram of the neck width(*w*) between AAO pores with average neck width of 29.7 nm (*std. dev. ±2.6 nm*).

Figure 3.7 schematically illustrates the present approach for fabricating NPG. The CVD grown graphene on Cu foil was used as the starting material. The copper layer was removed by chemical reaction with aqueous 0.1M ammonium persulfate solution, $(NH_4)_2S_2O_8$. The floating graphene in water was transferred onto a Si/SiO_2

substrate. We used the SiO_2-coated Si (Si/SiO_2) substrate for electrical measurements of FET device. The AAO membrane was placed on graphene and the transferred AAO membrane was used as the etch mask for fabrication of NPG. After the oxide template was placed on top of graphene, O_2 plasma etching was employed to generate nanopores in the graphene layer. Finally, the AAO mask was etched away by NaOH solution and the sample was washed with acetone.

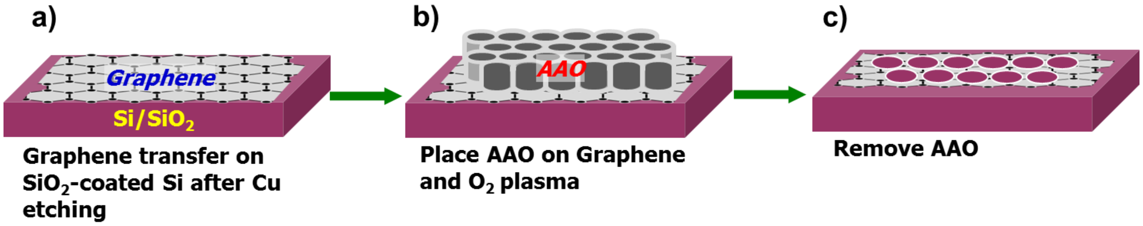

Figure 3.7: Schematic of nanopatterned graphene fabrication. (a) CVD grown graphene was transferred onto a Si/SiO_2 substrate (b) a AAO template was placed on top of graphene. (c) Graphene in the exposed area was etched away by O_2 plasma through the AAO pores and then the AAO was removed. Finally, porous graphene on SiO_2 was obtained.

Raman spectroscopy was used as a nondestructive tool for probing the edge structure and the crystallinity of sp^2-bonded graphene. Figure 3.8 demonstrates the Raman spectra of pristine graphene, and NPG. The Raman data was taken from different spots on graphene to check the uniformity. Prior to patterning, the G (～1586 cm^{-1}) and 2D (～2682 cm^{-1}) bands were prominent. The D peak at ~1341 cm^{-1} is related to defects and disorder. This is forbidden in perfect graphitic systems and requires a defect for its activation, and so is observed at the edges of graphene samples [128, 129, 132, 136]. The integrated intensity ratio of the D band and G band (I_D/I_G) is a parameter sensitive to defect density [129, 136]. In Figure 3.8a, the high D peak was observed on porous graphene with the value of I_D/I_G increased by a factor of 3, which suggests that defects in our sample are significantly formed by nanopatterning and pore edge formation. After nanopatterning, there is a systematic upshift in the position of G band. The G band position for porous graphene was observed at ～1594 cm^{-1}, which can be compared with the G position of pristine graphene (～1586 cm^{-1}) in our sample. This upshift in the G band position further confirms the hole-doping in the NPG by the formation of oxygen dangling bonds with graphene, as reported by previous research [128]. We also note that there is an increase in intensity ratio of the I_G/I_{2D} with more defects. The increase in I_G/I_{2D} in NPG is due to the alteration of its electronic transformation from semi-metallic to semiconducting with successive opening of band-gap [136].

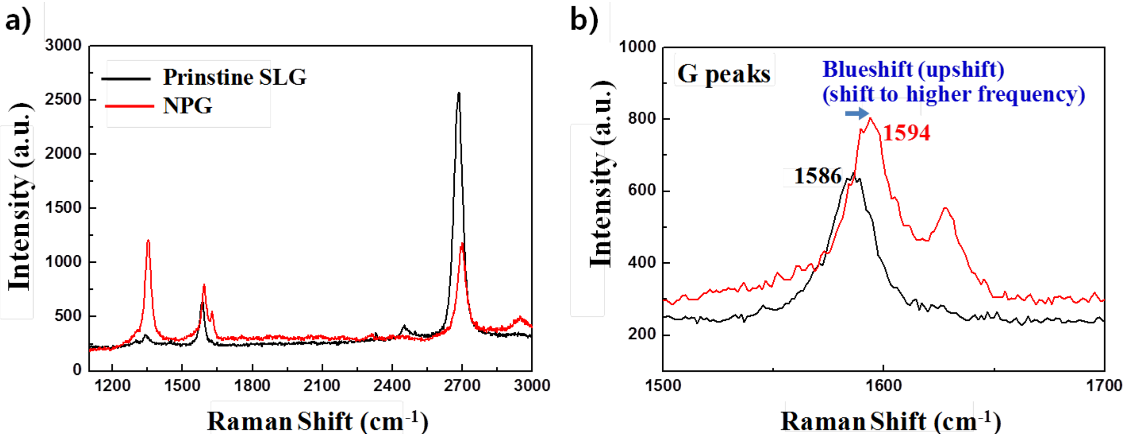

Figure 3.8: Comparison of Raman spectra, (a) before vs after patterning (b) NPG showing ~8 cm^{-1} blueshift on G band due to nanopatterning (11-13 nm neck width).

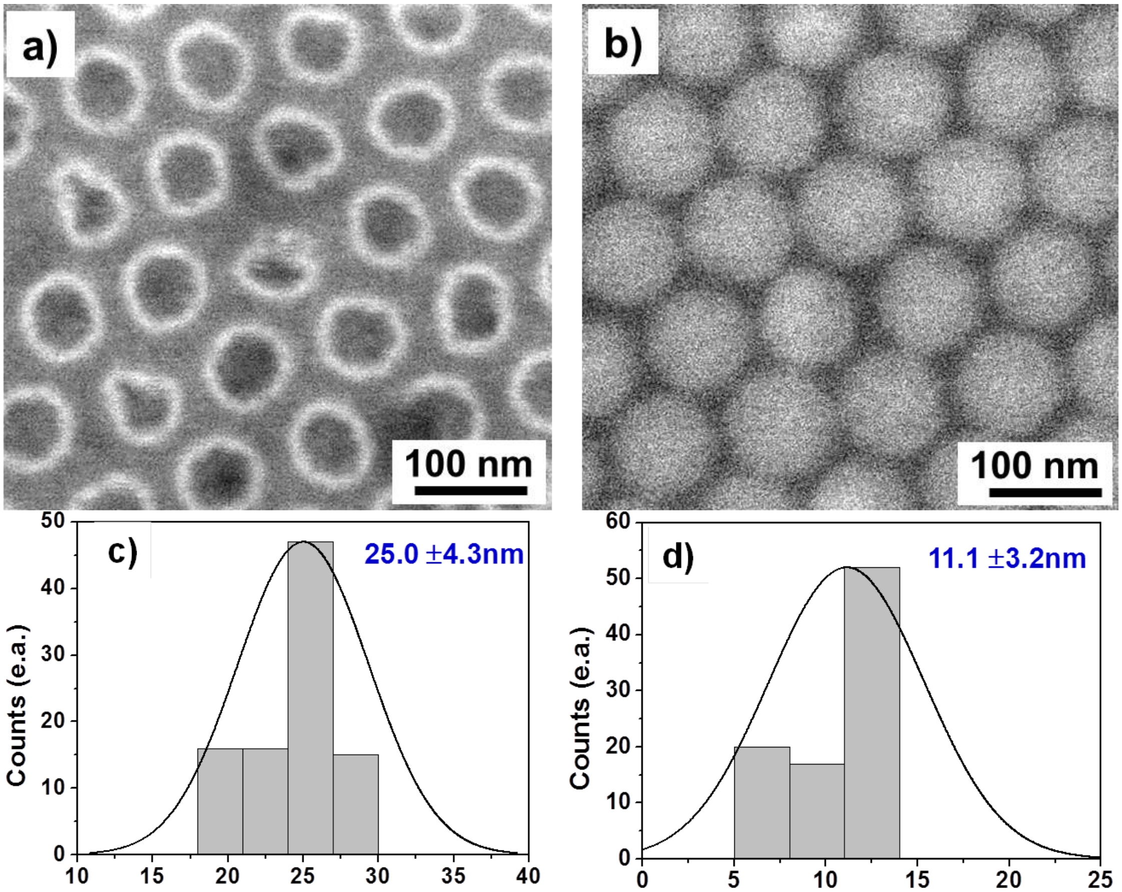

Figure 3.9: Example SEM images of the NPG surface after removing the AAO mask. (a) NPG with 30 sec etching time, (b) NPG with 40 sec etching time, (c) The neck width in (a) is 25.0 ± 4.3nm. (d) The neck width in (b) is 11.1 ± 3.2nm.

Figure 3.9 shows some example SEM images of NPGs with different average neck widths with different etching time from 30 sec to 40 sec. Furthermore, it is possible to tune the coverage areas of NPG by controlling etching time. As the neck width represents the smallest dimension that controls charge transport through the system, we have carried out statistical analysis of the neck widths of the NPG obtained after O_2 etching (Figures 3.9c and 3.9d). The histograms resulting from the statistical analysis show that the average neck width on graphene after controlled etching for 30 sec is 25.0 ± 4.3 nm (Figure 3.9c). It is expected that a neck width reducing process, such as utilizing a controlled oxygen plasma etch, could be utilized, which can lead to a substantially reduced neck width and associated interesting change in the degree of bandgap opening, creating further enhanced quantum confinement effect. Figure 3.9d shows a NPG with a smaller average *w* of 11.1 ± 3.2 nm, which is achieved through an intentional slight over-etching by exposing to 40 sec oxygen plasma. These SEM analyses on our graphene layer agreed with previous studies which clearly demonstrate that highly uniform porous graphene can be obtained with controllable etching time by the template approach.

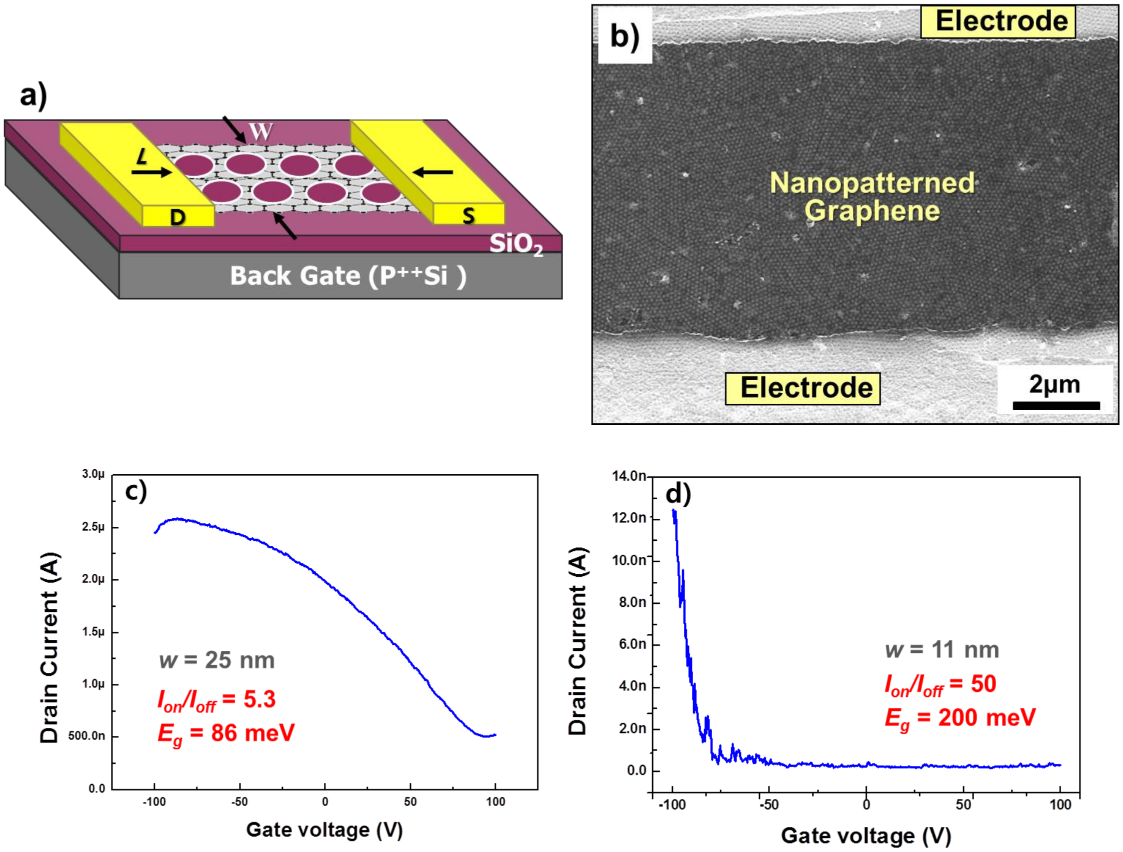

Figure 3.10: FET structure and electrical properties. (a) Schematic illustration of the FET device fabricated using the NPG, (b) SEM image showing the top-view of the NPG based FET device. (c) Drain current (I_d) versus gate voltage (V_g) for a FET device with *w* = 25.0±4.3nm. (The electronic measurement was carried out in ambient conditions at room temperature). (d) I_d versus V_g for a device with *w* = 11.1 ± 3.2nm.

Figure 3.10 displays the electrical characteristics of field effect transistors (FETs) containing the NPG structure at room temperature. Figure 3.10a schematically illustrates the structure of patterned graphene FET device, in which a rectangular-shaped NPG with total channel width *W*, and channel length *L* serves as the conduction channel. A pair of metallic pads (Ti/Au) serves as drain and source contacts. The 300-nm thick thermal oxide SiO_2 layer and degenerated (p^{++}) Si wafer are used as the gate dielectric and the back gate, respectively. Figure 3.10c and d show the electrical transport characteristics of a typical patterned graphene transistor with averaged neck width of ~25 nm. Drain current (I_d) versus gate voltage (V_g) characteristics for the transistor shows a typical p-channel transistor behavior (Fig. 3.10c and d). The increase in p-doping is likely due to increase in oxygen plasma exposure, resulting in dangling bonds on the edges of the holes [21]. The hole doping observed in the NPG is similar to that of graphene nanoribbon devices, and can be attributed to edge oxidation in the O_2 plasma process or physisorbed oxygen from the ambient and other species during the nanofabrication process.

The expected bandgap from the relation of $E_g \sim \alpha/w$ by averaged neck width of ~10 nm was 95 meV. In Figure 3.10d, however the actual bandgap in our FET device with 11 nm neck-width NPG is estimated to be ~200 meV from Eq (2) with our measured I_{on}/I_{off} value of 50. By contrast, the FET device with a larger 25 nm neck-width NPG exhibits an order of magnitude smaller I_{on}/I_{off} ratio of ~5.3 with much less bandgap opening as shown in Figure 3.10. There is a difference between the calculated bandgap values from the relations with neck width for our FET having average neck width of ~11 nm and the on/off current ratio experimentally measured, with the actual measured ratio being higher. Further detailed study is in progress to understand the mechanism behind this observation of surprisingly high effective bandgap in our NPG samples. We assume that the unusually high on/off ratio in our more extensively patterned graphene affected bandgap opening, possibly due to the highly dense and uniform NPG nanostructure throughout the large area samples. Such results point to a possibility of utilizing the properly and highly uniformly nanopatterned large area graphene as promising electronic devices.

Electrical characterization of NPG confirmed that the current on-off ratio is inversely proportional with neck width, indicating the formation of an effective gap due to the confinement effect. We have shown that both electronic transport and Raman characteristics change in a concerted manner on graphene patterning. The availability of such well controlled NPG structure will provide an interesting possibility for more in-depth fundamental investigation of transport behavior in the highly interconnected graphene network, and will enable exciting opportunities in sensitive electronics and sensor devices.

3.4 Summary and future work

We have successfully fabricated and characterized NPG with neck width of ~19 nm. This semiconducting graphene structure was first fabricated using PS-*b*-P4VP block copolymer template and a process that used a buffer layer of SiO_2 on graphene. We also presented the first experimental study on current distribution in single and multilayer NPG FETs. The NPG allowed experimental confirmation of the relationship between electrical conductance and bandgap. Electrical characterization of NPG confirmed that the current on/off ratio is inversely proportional with neck width, indicating the formation of an effective gap due to a confinement effect. We showed a difference of the I_{on}/I_{off} ratio with thickness dependence, which is enabled to explain by the interlayer coupling. We need to study experimentally more that the interaction between layers and the stacking sequence affect the topology of the π bands as well as an electronic transition from two-dimensional (2D) to bulk (3D) character when going from one layer to multilayer graphene. From these comprehensive studies, we have shown that both electronic transport and Raman characteristics change in a concerted manner as graphene patterning. The availability of such NPG will provide an interesting system for fundamental investigation of transport behavior in the highly interconnected graphene network, and will enable exciting opportunities in sensitive biosensors and a new generation of devices. We also believe that the process is scalable and relatively ease, by which BCP lithography can be implemented and scaled to large areas by either phase separation process of thermal or solvent annealing, and its effectiveness at controlling the electronic properties of graphene will enable practical large-area, commercializable applications of graphene in thin film electronics, flexible electronics, optoelectronics, and sensing.

We demonstrate a successful fabrication of very fine dimension NPG using a thin floating anodic aluminum oxide (AAO) membrane etching mask. The membrane was directly transferred onto a hydrophobic graphene surface for well adhered and stacked manner on the graphene due to the van der Waals force, thus allowing a high-density, small-neck NPG structure fabrication, without using any intermediate buffer/adhesion polymer which could adversely affect the resolution of plasma etching patterning of graphene. The NPG so produced exhibits homogeneous mesh structures with an average neck width as small as ~11 nm. Electronic characterization of single layer NPG FET structure with 11 nm neck-width creates a quantum confinement in

NPG, which has led to an impressive bandgap opening of ~200 meV. The NPG structures with different neck-width allowed experimental confirmation of the relationship between electrical conductance and bandgap. Electrical characterization of NPG-based FET device confirmed that the current on/off ratio is inversely proportional with neck width, indicating the formation of an effective gap due to a confinement effect. The availability of such NPG will provide an interesting system for more in-depth fundamental investigation of transport behavior in the highly interconnected, small-width graphene network, and will enable exciting opportunities in sensitive electronic or sensor devices. This work also demonstrates that self-assembled mask lithography is a pathway for low-cost, high throughput, large scale nanomanufacturing of NPG with critical dimensions down to nanometer regime.

Chapter 3, in full, is a reprint of the material as it appears in Materials Research Letters, 2(3) 131-139 (2014) written by Duyoung Choi and Sungho Jin. The dissertation author was the primary investigator and author of this work.

CHAPTER 4:
Unusually high optical transparency in hexagonal nano-patterned graphene with enhanced conductivity by chemical doping

4.1 Introduction

The transparent conductor, indium tin oxide (ITO), is widely utilized in displays, touch-panels, light emitting diodes and solar cells[2, 48, 117]. Although the ITO exhibits desirably high optical transparency (*T*) and low sheet resistance (R_s), the limited supply of indium with increasing price has raised concerns on long-term supply of ITO material. Therefore, it is desirable to find potential replacement materials based on less critical elements[2, 48]. In addition, the trend is such that future displays are likely to become larger and many of them will probably be based on a flexible plastic substrate material. Thus, prospective displays would require more flexible transparent electrodes that can be produced at low temperature and over large areas at low cost. [48] There are several novel materials for alternative transparent conductive electrodes, for example, carbon nanotubes (CNTs)[21], metallic nanowires[150], thin metal films[139], and graphene[1, 39, 41] Compared with commercial ITO layer, these new candidates make some compromises between optical transparency and electric conductivity.[39]

Graphene has recently emerged as a new material due to its remarkable properties including high charge mobility, high optical transmittance, mechanical strength and flexibility[3, 9, 15, 39] These attractive properties can make graphene a promising candidate for a transparent flexible electrode with low sheet resistance and high transparency, which can also be synthesized on a large scale.[9, 15, 34, 45]

Potential applications of graphene as electrodes in a wide range of devices including field-effect transistors[127], touch sensitive screens[39], liquid crystal displays[52], light-emitting diodes[2], flexible field emission display[150], dye sensitized solar cells [22] and organic solar cells[23] have been reported. However, to ensure viable applications, the optical vs. electrical characteristics of graphene films need to be further improved and tuned by engineering of two critical parameters, i.e., sheet resistance and optical transparency.[50]

Graphene films having high conductivity and low optical loss may be engineered by doping or surface modifications. As the graphene quality is strongly dependent on the growth conditions, low sheet resistance has not been reproducibly obtained partly because of the poor crystallinity, formation of wrinkles, and small domain sizes of graphene layers.[11, 148] Chemical doping or functionalization has been shown to modulate the conductivity of graphene by controlling the charge carrier density[61, 62], band gap[36, 145], or work function.[1, 117] An alternative approach for reducing the sheet resistance is to stack or synthesize a few layers of graphene (FLG). Lee et al. and Blake et al. prepared higher-temperature- and longer-time-grown, thicker graphene films, which, as expected, exhibited reduced sheet resistance but also reduced optical transmittance as the number of graphene layers is increased.[34, 127] Günes et al. proposed a new method of layer-by-layer (LbL) doping to decrease the sheet resistance of graphene films. With this method, sheet resistance was significantly decreased by up to ~80% with some sacrifice in optical transmittance.[151]

To solve the drawback of low optical transmittance in FLG, we have introduced a nano-hole array in the graphene layer so as to increase the area fraction of graphene-free regions. In order to increase the graphene-free area, ordered nano-hole array has been achieved by UV/e-beam lithography and nanoimprint lithography.[122, 139] Although optical, electron or related lithographic methods can provide precisely located nanoarrays, the overall size of the area that can be patterned into nano-dimensions (e.g., below ~100 nm feature size) in an industrially viable way is often limited due to the delicate handling, expensive and time-consuming nature of such processes.[119, 142, 145]

To advance a facile process technique for nanopatterned graphene (NPG), we have specifically utilized an anodic aluminum oxide (AAO) mask lithography as it can be scaled to large-area substrates with high-fidelity of patterning, which can be compatible with conventional lithographic processes.[120, 121] With an array of nanoholes introduced, the sheet resistance obviously becomes deteriorated (increased) due to the lost material pathway. However, a substantial portion of the lost electrical conductivity in the nanopatterned graphene formed by facile AAO technique could be recovered by doping, as is demonstrated in this work. Liu et al. proposed that nanopatterned graphene can provide large number exposed edges of holes for effective doping sites[152] indicating a possibility of tuning electrical transport properties of graphene. In this report, we have demonstrated a new approach of controlling a transmittance and conductivity in a sheet of FLG. We have carried out experimental investigations on the optical and electrical performances in FLG before vs after chemical doping. In this work, nitric acid (HNO_3) was used as a molecular adsorbate to reduce the sheet resistance of graphene films.[28, 151] A facile patterning of the graphene has been accomplished by using a self-assembled, free-standing AAO template which is directly transferred onto FLG. To the best of our knowledge, this is the first time that such convenient AAO nano-patterning of graphene has been demonstrated without resorting to a buffer layer like polymer. The fabrication of NPG using the AAO approach can be employed as a novel method for engineering transmittance and conductance of graphene, which can open up other electronics and optoelectronics applications.[38]

4.2 Methods

4.2.1 Preparation of Isolated Graphene and Transfer Process

Graphene layer was synthesized by thermal chemical vapor deposition (CVD) using methane (CH_4) gas at 1000°C. A thin Cu foil (25 μm thickness) was purchased from Alfa-AESAR, USA, cut into 20 mm × 13 mm size and annealed at 1000℃ for 1 h in an inert gas atmosphere followed by hot acid treatment and cleaning. The Cu foil was placed inside a thermal CVD system and the temperature was increased up to 1000℃ with a heating rate of 120℃ min^{-1}. The atmosphere of the CVD furnace was maintained at 0.8 atm in the presence of an inert gas (Ar), and CH_4 : H_2 (1 : 4) mix was used as a precursor gas mixture for graphene growth. After the CVD growth on both surfaces of Cu foil, the back side graphene was removed by oxygen plasma. The top side graphene was protected by a Poly methyl methacrylate (PMMA) layer during the O_2 plasma etching. The graphene film was then transferred onto a SiO_2-coated Si substrate (300 nm thick SiO_2 layer) using a chemical process to etch away the Cu foil substrate and then transferring the floating graphene onto a Si/SiO_2 substrate by lifting up the substrate, followed by washing with water, acetone, and isopropyl alcohol as described elsewhere.[38] The surface of the Quartz was cleaned using piranha solution (60% sulfuric acid+40%hydrogen peroxide). The Quartz substrates were soaked in freshly prepared piranha solution for 1 h, followed by a thorough rinse with deionized (DI) water, followed by acetone, and then blown dry with argon gas.[127] In addition, a rapid thermal annealing was carried out for graphene sample on the Si/SiO_2 substrate by heating at 400℃ under a N_2 atmosphere to remove the residual PMMA and promote the adhesion of graphene onto the Si oxide layer underneath.

4.2.2 Preparation of AAO Membrane

A 0.5mm thick annealed Al foil purchased from Alfar aesar (99.99%) was used as the starting material. The Al foil was successively degreased by acetone and isopropyl alcohol with ultrasonication followed by deionized (D.I.) water rinse and nitrogen gas blow. The Al foil was slightly etched in 1M NaOH aqueous solution to remove any possible surface contaminations prior to surface smoothing electropolishing process conducted at 20V in a solution of perchloric acid (70%) and ethanol (99.9%) (1:4 volume ratio) at 5℃ for 15 minutes, using a Pt counter electrode. Then, a two-step anodization process of the Al foil was carried out by incorporating the Al foil as the working electrode and Pt as the counter electrode, immersed in 0.3 m oxalic acid. The electrolyte temperature was maintained at 1℃ during anodization process using a powerful refrigeration bath (RTE7, Thermo Scientific) in which the coolant circulates double-wall glass chamber. After the first anodizing process, which took about 3 hours at an operating voltage of 40 V, the anodized Al foil was immersed for 1 hour in a mixed solution of phosphoric acid (6 wt%) and chromic acid (1.8 wt%) kept at 75℃ to remove the alumina layer formed in the first anodizing step. The second anodizing step was implemented for 10 minutes while other experimental conditions were unchanged compared with the first anodizing step, in order to form an ordered porous alumina membrane on the Al foil. Then, the Al substrate was selectively removed with a mixed HCl and $CuCl_2$ solution for 10 minutes. Any residual Cu debris adhered to the bottom of the AAO barrier layer was removed by placing in nitric acid for a few seconds and washed in D.I. water immediately after. The barrier layer in the bottom of the AAO holes was then removed by 5 wt% phosphoric acid etching for 10 minutes to two hours.

4.2.3 Fabrication of NPG

The prepared AAO template floating in water was placed on the graphene as an etch mask by lifting up the Si/SiO_2 substrate from underneath. Then another Si/SiO_2 wafer (SiO_2 coated Si) was placed on the AAO membrane, so that the AAO/graphene assembly was pressed between two Si/SiO_2 wafers. After that, this sandwich structure was annealed in vacuum at 180℃ for 2 h, in order to allow the AAO membrane to stick tightly on the graphene surface. After removal of the top Si/SiO_2 substrate piece, O_2 plasma (35 W, 160 mTorr) was applied through the AAO template (mask) holes to create pores on the graphene. The O_2 plasma etching was applied with various times of 30, 40 and 50 seconds. Finally, the AAO mask was etched away by NaOH and the sample washed with acetone. The chemical doping of the pristine and nano-patterned graphene (NPG) samples were conducted by exposing the samples to a 63 wt% HNO_3 solution for 6 minutes.

4.2.4 Graphene Characterization.

The sample microstructure was characterized by ultra-high resolution scanning electron microscopy (UHR SEM; FEI XL30). Raman spectroscopy was used as a nondestructive tool for probing the edges and the crystalline sp^2-bonded structure of the graphene.[128] Raman Spectra were collected using a Renishaw Raman Spectrometer inbuilt with Ar^+ laser of wavelength of 514 nm for quantifying the degree of structural order and charge transfer characteristics. To measure the sheet resistance of graphene nano mesh (GNM), Jandel Four Point Probe was employed for the four point measurement. The optical property of the graphene samples was characterized by UV/Vis spectrophotometer (UNICO SQ-4802).

4.3 Results and Discussion

The AAO membrane prepared by two step anodization of high-purity aluminum foil exhibited locally periodic array of pores with the pore size being ca. 77.2±2.7 nm (Figure 4.1a). As shown in the tilted image of an AAO membrane in Figure 4.1b, the membrane thickness is ca. 200~300 nm. This self-assembly fabricated AAO membrane was used as a mask during the oxygen plasma etching of graphene for nanohole array formation.

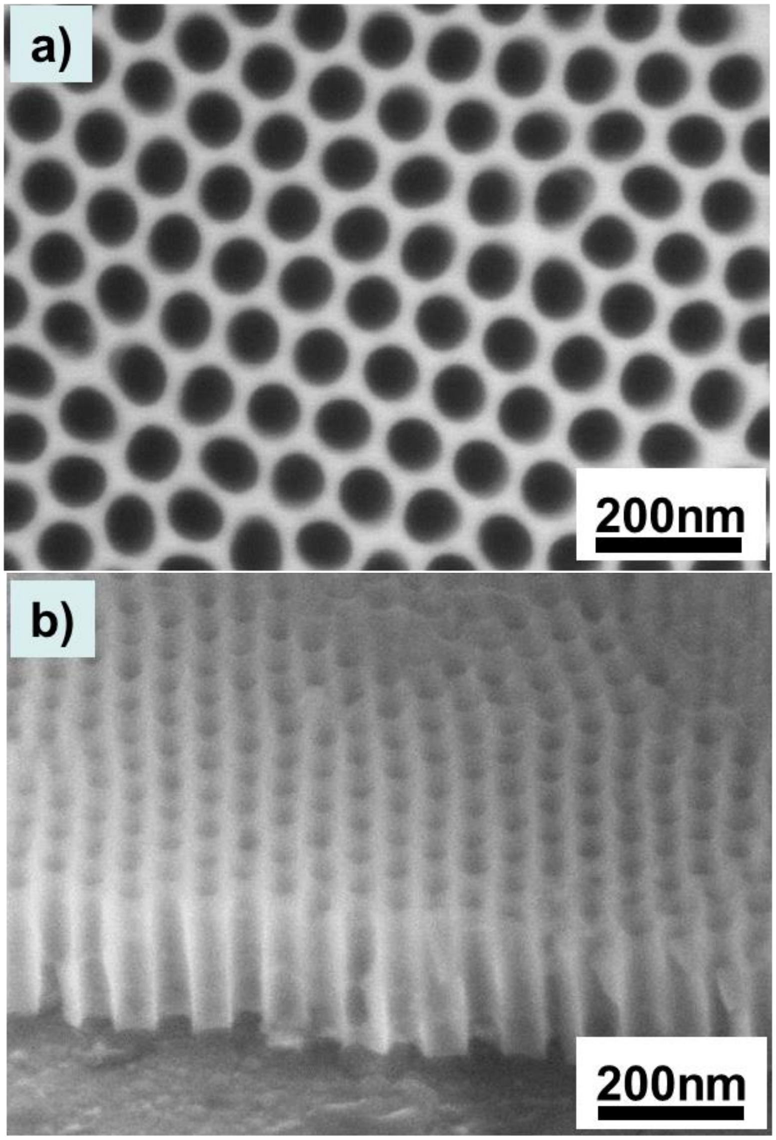

Figure 4.1: Scanning electron microscopy (SEM) images. (a) AAO template (top view), (b) tilted view AAO membrane with <300 nm thickness (c) Histogram of the AAO pore size with average pore size of 77.2 nm (*std. dev. ±2.7 nm*).

4.3.1 Fabrication of Nano-patterned (NP) Graphene

Figure 4.2 schematically illustrates the present approach for fabricating NPG. For initial demonstrations, the CVD grown graphene layer on Cu foil was used as the starting material. The copper layer underneath was removed by electrochemical reaction with aqueous 0.1M ammonium persulfate solution, $(NH_4)_2S_2O_8$. The floating graphene was transferred onto a Si/SiO_2 or quartz substrate. We used the Si/SiO_2 substrate for electrical measurements of sheet resistance and the quartz substrate to measure the optical transmittance. Silicon and quartz substrates were cleaned by piranha solution to remove any organic contamination and the surface was treated with oxygen plasma to introduce hydrophilic surface. The AAO membrane was placed on graphene and the transferred AAO membrane was used as an etching mask for fabrication of NPG.

Zeng et al reported that nanometer-sized features on graphene cannot be achieved simply by directly placing the AAO membrane on rGO because of the rigid nature of AAO. Thus, PMMA was employed in their experiment as an adhesion layer between the AAO and graphene. To minimize the void space between graphene and AAO interface, they also annealed graphene/PMMA/AAO in a high temperature vacuum oven.[153] However, we were able to overcome the issue by fabricating a less rigid and thin AAO template (<300nm-thick), and successfully demonstrated fabrication of nanoholes patterned graphene using this oxide template without polymer buffer layer thus avoiding such complicated processes. The key to this success was the thinness and uniformity of the AAO membrane that we fabricated. After the oxide template was placed on top of graphene, O_2 plasma etching (25 W, 150 mTorr) was employed to generate nanoholes in the graphene layer. Finally, the AAO template was removed using a NaOH solution.

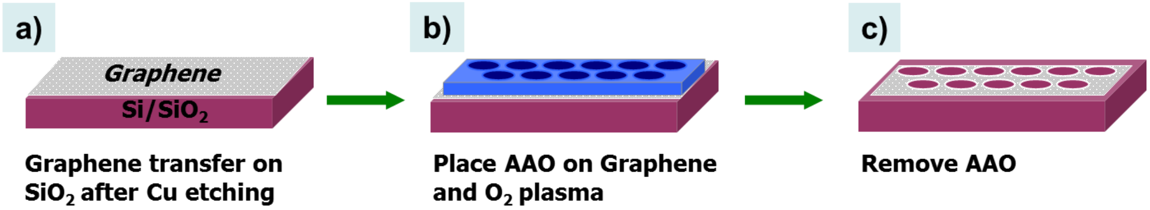

Figure 4.2: Schematic of nanopatterned graphene fabrication. (a) CVD grown graphene was transferred onto a Si/SiO$_2$ substrate, (b) an AAO template was placed on top of graphene, (c) graphene in the exposed area was etched away by O$_2$ plasma through the AAO pores in the template and then the AAO was removed. Finally, porous graphene on SiO$_2$ was obtained. (The inset is an SEM image, the scale bar is 200 nm.)

4.3.2 Raman Studies for Few Layer and NP Graphene

Raman spectroscopy was used as a non-destructive tool for probing the edge structure and the crystallinity of the sp^2-bonded graphene samples. Figure 4.3 demonstrates the compasrative Raman spectra of pristine graphene and NPG. The Raman data was taken from different spots on the graphene samples and were found to be uniform. Prior to patterning, the G (~1580 cm^{-1}) and 2D (~2680-2700 cm^{-1}) bands were prominent. Raman spectroscopy can also be utilized to determine the number of layers in multilayer graphene and to discriminate between single layer graphene (SLG) vs few layers graphene (FLG) using the intensity ratios of G band and 2D band. For a single layer graphene, I_G/I_{2D} intensity ratio is known to be ~0.24 which increases with the number of graphene layers thus making it possible to estimate the thickness of graphene layers.[52] Figure 4.3 shows that the ratio of I_G/I_{2D} in our graphene is around 0.7 and it can be estimated to be approximately 4~8 layers of graphene.[127] The peak related to the 2D band also provides additional support for relative graphene layer thickness. The 2D peak in our NPG is located at ~2703 cm^{-1}, which corresponds to ~4-8 layers of graphene, which is consistent with the literature; for example, Rafiee *et al.* have reported that, as the number of layers in graphene films is increased, the 2D peak shifts towards a upper frequency range from ~2,680 cm^{-1} for monolayer graphene to ~2,715 cm^{-1} for the >10 layers graphene.[154] In addition to the difference in the intensity of 2D peak, the full width half maxima (FWHM) of 2D band also increases as the number of graphene layers increases.[28, 129] As the 2D band peak originates from a two phonon double resonance process, it is closely related to the band structure of graphene layers. Ferrari *et al*.[128] have successfully used the splitting of the electronic band structure of multilayer graphene to explain the broadening of the 2D band.

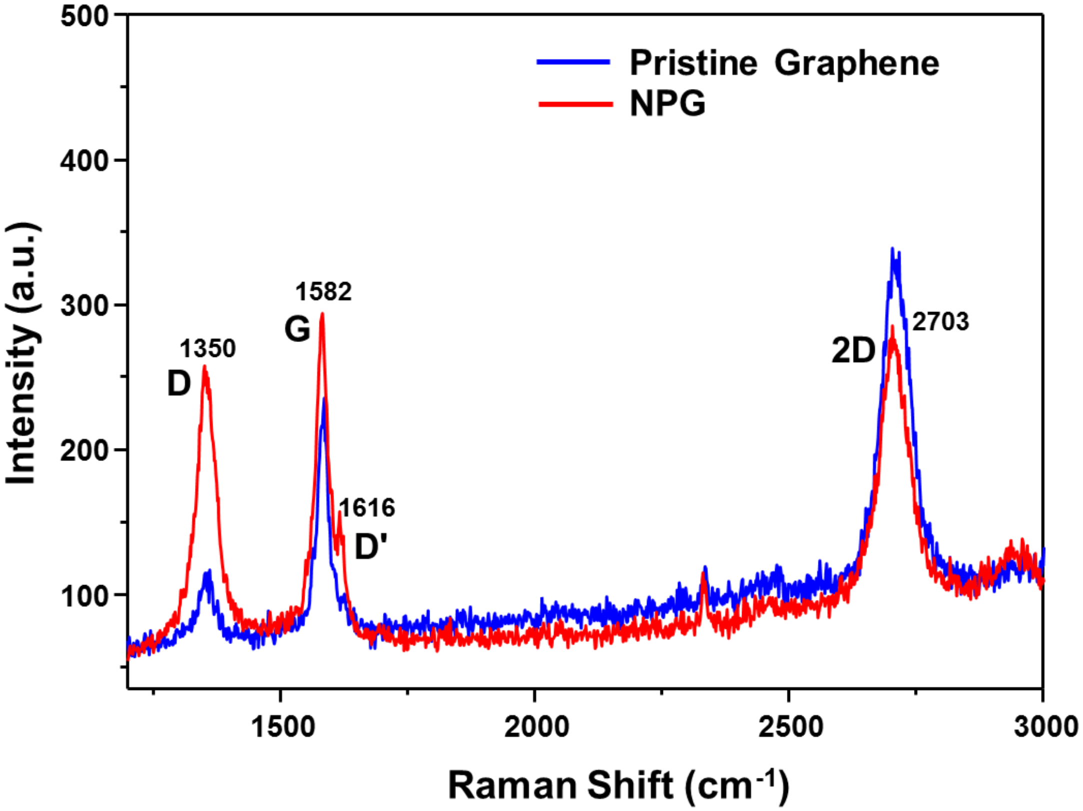

Figure 4.3: Comparison of Raman spectra of pristine and nano-patterned graphene (NPG) with their characteristic D, G, and 2D bands shown at the respective positions.

For mono and bi layer graphene, the FWHM of 2D band is ~30 cm^{-1}[28] and for the FLG in our data, it is ~63.24 cm^{-1}. We believe that the 2D peak broadening can be attributed to the number of layer increases in graphene structure.[2] In this work, the transferred graphene consists of about 4-8 layers of graphene sheets, as known in Raman, hence our samples can be referred to as FLG of few layers graphene. The D peak at ~1330 cm^{-1} is related to defects and disorder. This peak is forbidden in perfect graphitic systems and requires a defect for its activation, and so it is observed by the presence of the edges in graphene samples.[50] The integrated intensity ratio of the D band and G band (I_D/I_G) is a parameter sensitive to defect density.[136]

Previous studies have revealed that the intensity of the D band is related to the basal plane disorder[140] and thus, the increased D band (see Figure 4.3) in our NPG sheets may represent formation of disorders or defects caused by nano-patterning. We also note that there is an increase in intensity ratio of the I_D/I_G with more plasma etching time for nano-patterning. The intensity ratio of 0.35, 0.55, and 0.77 has been obtained (shown in Table 1) with increasing etching time from 30 sec to 40 sec then to 50 sec respectively. This trend agrees with the previous report that for lithographically patterned graphene nanoribbons (GNR), I_D/I_G increases with an increase in defect density and decrease in neck width.[21] After nano-patterning of our samples, there was a systematic upshift in the position of G band. The G band position for porous graphene was observed at ～1582 cm^{-1}, which can be compared with the G position of pristine graphene (～1580 cm^{-1}) in our sample. This upshift in the G band position further confirms the hole-doping in the NPG by the formation of oxygen dangling bonds with graphene, as reported by previous research.[151, 152]

4.3.3 Change in R_S as a Function of Etching Time

Figure 4.4 shows SEM images of the NPG obtained using our AAO templates with a periodicity of 106.11.8 nm. The histograms resulting from the statistical analysis show that a series of NPG samples with adjustable pores diameter have been achieved. The average diameter of pores (D_p) on graphene after controlled etching for 30 sec is 75.4±6.9 nm. Figure 4.4d shows a NPG with a larger average D_p of 85.2±7.2 nm, achieved through an intentional slight over-etching of 40 sec. Here, it is demonstrated that the remaining area of networked graphene can be trimmed to 45.9 % and 31.1 % by adjusting the processing time to 30 sec and 40 sec, respectively under identical plasma etching condition (O_2 flow 50 sccm, pressure 150 mTorr, power 25 W). It is therefore possible to tune the coverage of graphene (remaining area of graphene) through etching time and other process parameters during the fabrication process. A control of plasma power can allow a slower plasma etching rate and an improved control of the degree of etching. It is envisioned that a pore widening process such as the controlled oxygen plasma etch could also be utilized to substantially reduce the graphene area and provide an additional control of the sheet resistance and optical properties. These SEM analyses on our graphene layer together with previous studies on graphene oxide samples [153] clearly demonstrate that highly uniform, porous graphene can be obtained with controllable pore size and coverage by the template approach. A histogram was constructed for our samples (see Figure 4.4) with all the measured values from the 0.5 µm × 0.5 µm area SEM image. The average mode values of nanoconstriction width with corresponding standard deviations were calculated and reported based on the histogram generated in Figure 4.4 (e) and (f).

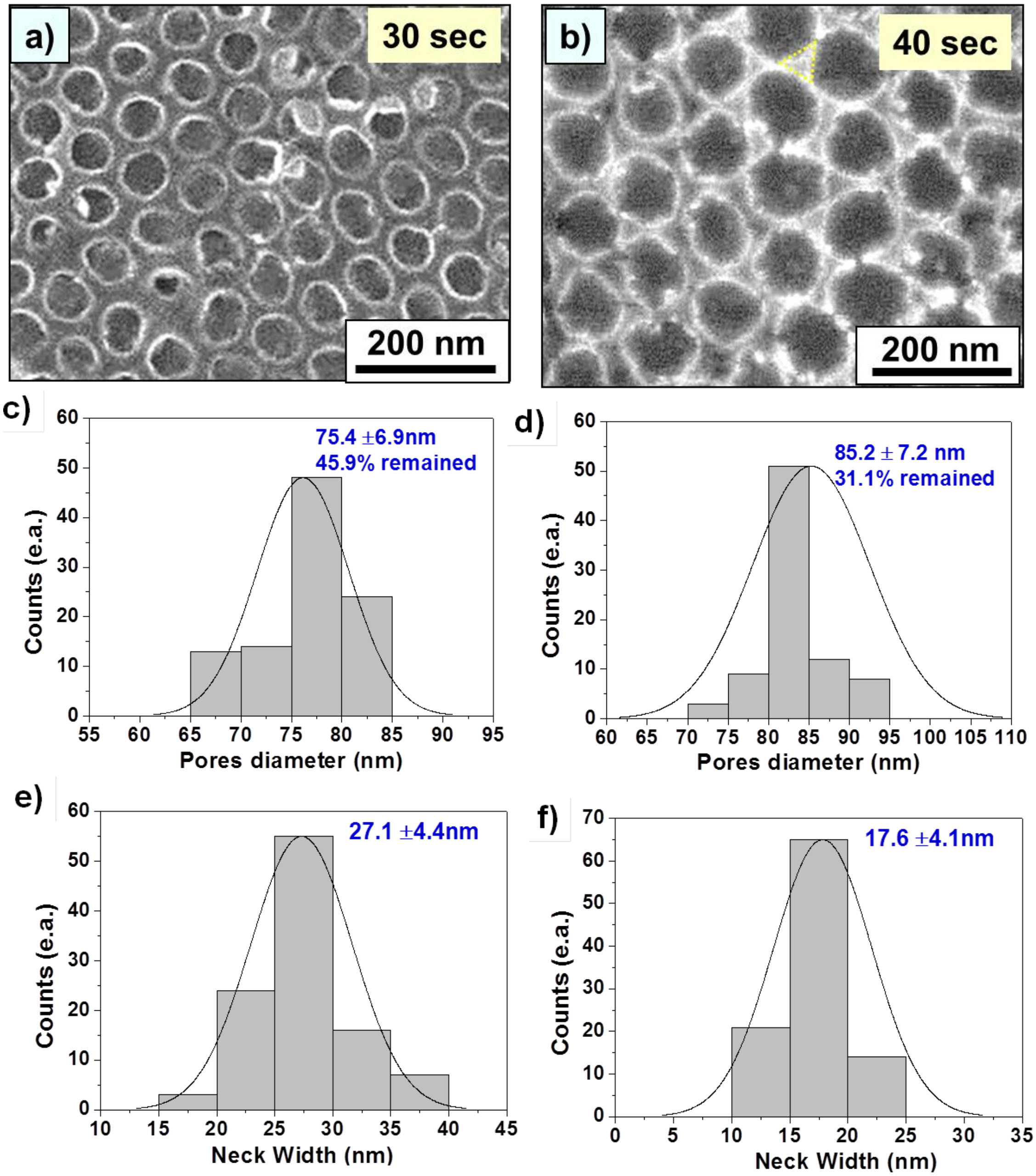

Figure 4.4: (a), (b) SEM images of the NPG surface after removing the AAO mask by 30 sec and 40 sec etching, respectively. The histogram in (c) shows that the average pore diameter in (a) is 75.4 ±6.9nm with ca. 46 % graphene area remained, while (d) shows that the average pore diameter in (b) is 85.2 nm ±7.2 nm with ca. 31% graphene area remained (the average hole periodicity is 106.1 ± 1.8 nm in both cases). The histogram in (e) shows the neck width in the (a) sample of 27.1 ±4.4nm, and (f) shows the neck width in the (b) sample of 17.6 ±4.1nm.

The electrical properties of graphene are most likely affected by patterning of graphene, as was actually observed in this study for the nano-patterned graphene (NPG) samples prepared by AAO template masking. The sheet resistance values, R_S, of the samples were measured in a four-probe configuration. Even though the sheet resistance can vary depending on the size of grains and amount of grain boundaries in graphene, as well as on defects/impurities generated during graphene synthesis or transfer, the measured R_S of 1208 Ω/sq for unpatterned graphene is generally consistent with those reported by Li et al.[15] and Verma et al.,[117]. The R_S of NPG samples increases considerably compared to the unpatterned graphene sample as shown in Figure 4.5 which plots the change of R_S according to the etching time and doping of NPG. These data show that the creation of NPG does in fact considerably increase the resistance of graphene by a factor of ~15, well above the level of the original unpatterned graphene samples. R_S increases by 1380 %, 1492 %, and 1741 % as compared to that of the unpatterned graphene for the etching time of 30, 40 and 50 sec, respectively, as shown by green upward arrows in Figure 4.5. This ability to control pore size in NPG is very important for controlling electronic properties, because charge transport properties are highly dependent on the width of the critical current pathway. In the case of graphene nanoribbons (GNRs), both theoretical and experimental work have shown that the size of the conduction bandgap or sheet resistance is inversely proportional to the ribbon width.[38,57,58] Therefore, a narrow pathway width and a denser mesh structure can enable lower current delivery. Our fabrication process shows great versatility in controlling both the neck width and the coverage of graphene which can be tuned through controlled plasma etching or over-etching during the fabrication process.

4.3.4 Improvement of R_S by doping.

The unique electronic property of graphene can be modulated by the charge carrier concentrations, which is dependent on introducing of gate bias and chemical doping[39], resulting in an improvement (reduction) of sheet resistance. Other novel approaches may also be introduced to further improve the optical transmittance and the sheet resistance of graphene, such as electrostatic doping method as was recently reported. With an introduction of electrostatic potential, various device junctions can be constructed by connecting GNRs of different width and orientation with perfect atomic interface, and more importantly device units can be selectively doped by manipulating the edge terminations of GNRs.[30] In the present research, the electrical resistance of the graphene increases significantly by a factor of ~15 by removal of substantial graphene regions via nano-patterning into hexagonal array pores. However, our use of chemical doping on the nanopatterned graphene almost completely recovers the lost electrical conductivity, thus leading to a desirably much more optically transparent conductor having ~7 fold reduced light blockage by the nanopatterned graphene material without much loss of electrical conductivity. It is likely that the availability of large number of edges created in the NPG provides ideal sites for chemical dopant attachment, leading to a significant reduction of the R_S. The results indicate that the NPG approach can be a promising route for simultaneously tuning the optical and electrical properties of graphene to make it more light-transmissible and suitable as a new generation of flexible transparent conductors.

The electrical sheet resistance of the graphene increases significantly by a factor of ~15 by removal of substantial graphene regions via nano-patterning into hexagonal array pores as shown in Figure 4.5 (green upwatrd arrows). In order to reduce the sheet resistance increase by nano-patterning, we employed chemical doping of NPG with an exposure to nitric acid (HNO_3) for ~6 minutes. HNO_3 is one of molecular adsorbates that can be used to effectively p-dope graphene films[39], which can reduce the sheet resistance of graphene films and where an electron is transferred from the graphene to the nitric acid as a charge-transfer complex is formed according to the reaction. Bae and co-workers investigated that the electrical properties of graphene films can be enhanced with various types of chemical dopants. The results indicate that the enhanced sheet carrier density is obtained in principle by multiplying the film thickness to the bulk carrier density and by doping with nitric acid. [39] The sheet resistance was reduced after a 63 wt% HNO_3 treatment for several minutes. However, the extent of resistance reduction upon chemical doping of pristine graphene sheet resistance was meager, only by 1.4 times as shown in Table 4.1. The recovery in sheet resistance of unpatterned graphene is consistent with the previously reported 2-4 times increase of conductivity accompanying p-doping of graphene by nitric acid treatment.[49] However, for the case of the nano-patterned graphene, an entirely different behavior is observed. The electrical conductivity recovery (sheet resistance recovery) by chemical doping is by a factor of ~13(!) as shown in Figure 4.5, much larger than the conductivity recovery for the case of non-patterned graphene layer (by ~1.4 in our graphene sample).

Such a pronounced electrical conductivity increase by chemical doping seen only in NPG samples is attributed to the availability of large number of edges created in the NPG structure which can provide ideal sites for chemical dopant attachment, thus leading to a significant reduction of the R_S. In principle, the edges of nanopatterned holes provide active sites, where the carbon atoms are much more chemically reactive than that in the plane of the perfect graphene.[155] Liu et al reported that the graphene nanomesh structure serves as a source of chemical enhancement for Raman intensity of adsorbed molecules. The edges in the nanomesh can act as chemical sites to quickly trap molecules for chemical modification of graphene.[152] If a similar doping mechanism applies to NPG, the large number of edges created on the nanohole arrays could facilitate attachment of HNO_3, which explains the very large enhancement in sheet conductivity observed in our doped NPG samples.

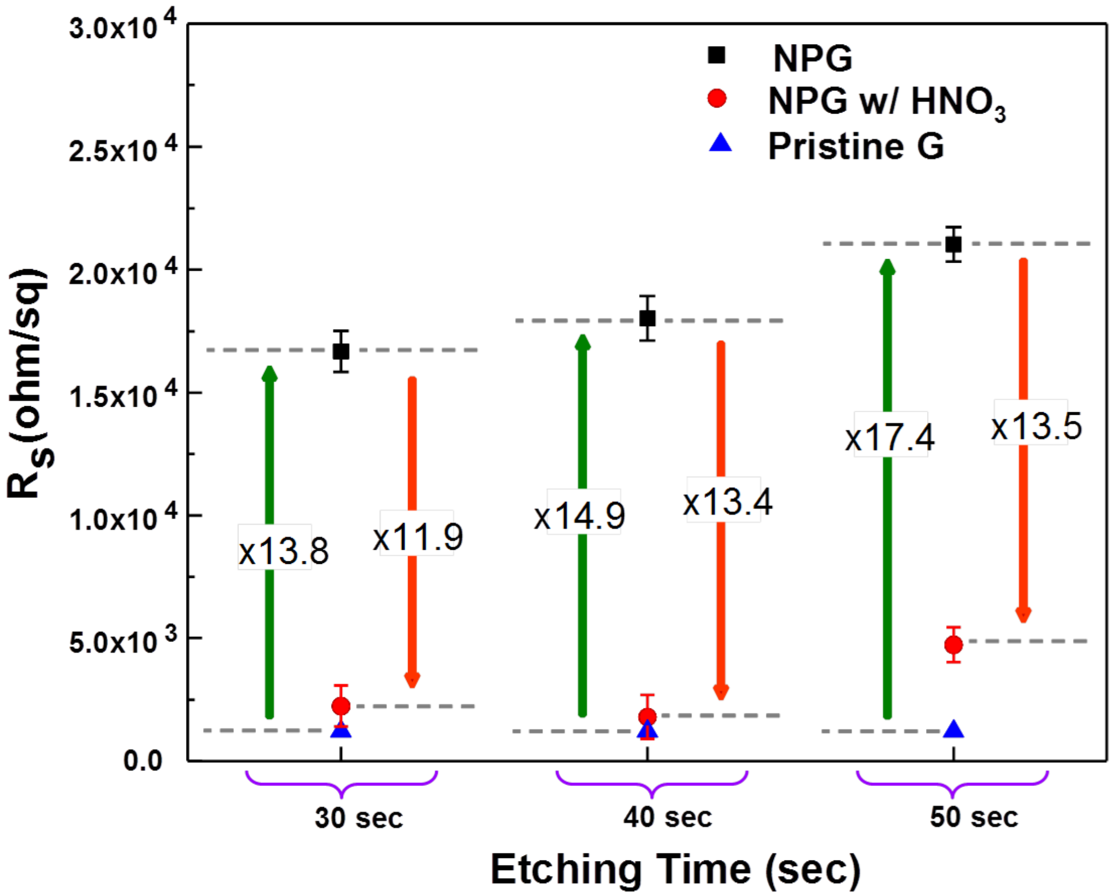

Figure 4.5: Sheet resistance (R_s) increase by nano-patterning of graphene (green arrows) and near-complete recovery of the electrical conductivity by chemical doping (red arrows), especially for the 40 sec etched sample. The R_s values are plotted for three different etching times (30, 40 and 50 sec).

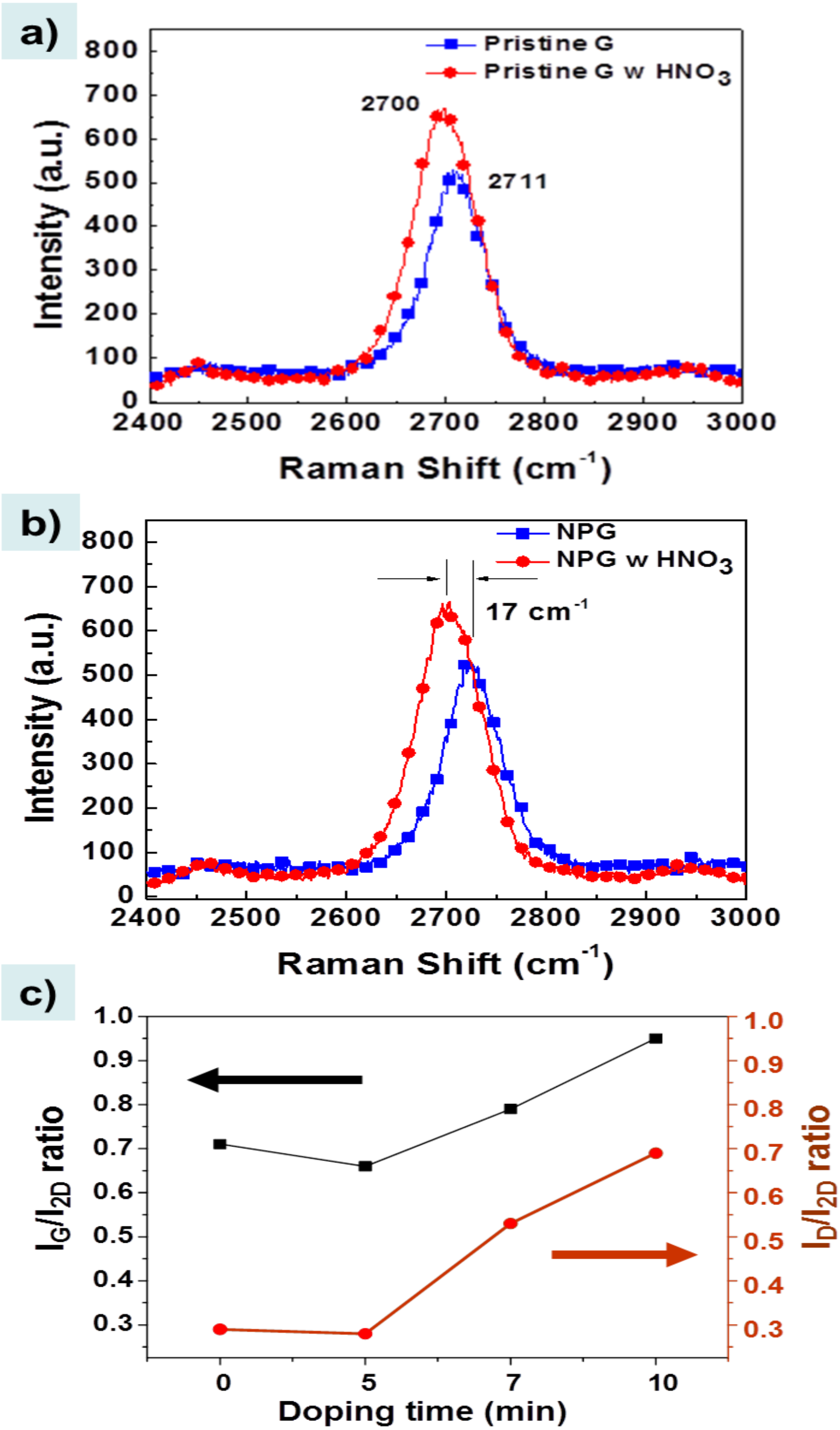

Figure 4.6: Comparison of Raman spectra before and after HNO_3 doping (a) pristine graphene of ~11 cm^{-1} blue shift (b) NP graphene showing ~17 cm^{-1} blue shift on 2D band (c) comparison of the intensity ratio for G and 2D bands by doping time.

To understand the effect of acid treatment, we carried out a Raman spectroscopy analysis of the as-prepared NPG as well as nitric-acid-treated (doped) NPG. Figure 4.6 shows Raman spectra of the graphene films before vs. after doping with 63 wt% HNO_3 for 10 min. There is some blue shift ($\Delta\nu = {\sim}11\ cm^{-1}$) in the 2D band peak for the pristine graphene, which is already known in p-doped graphene film. The increased peak shift in the position of the 2D band with acid doping of NPG sample ($\Delta\nu = {\sim}17\ cm^{-1}$) indicates that the HNO_3 carriers were doped in the NPG graphene lattice, which clearly indicates that the number of edge-plane-like active carbon sites in FLGs are increased compared with that in pristine graphene.[49] The position of 2D band is very sensitive to the local doping level in graphene.[52] Typically, a 2D band of undoped pristine graphene appears at 2700 cm^{-1}. After doping, there is a systematic upshift in the position of 2D band. The further enhanced upshift in the 2D band by acid treatment on NPG with increasing hole-doping is also confirmed by the analysis of the sheet resistance as well as the 2D band shifts of patterned graphene via O_2 plasma etching[136], and also corresponds to the previously reported Raman spectra of HNO_3-doped graphene showing a blueshift both for G and 2D peaks.[39] The ratio of the intensities of G- and 2D-bands (I_G/I_{2D}) is also considered to be sensitive to doping.[117] Figure 4.6c shows the ratios of the G/2D intensity of graphene with various doping time. The intensity ratio shows a marked increase with the increase in doping time.

4.3.5 Changes of Transmittance *vs.* Etching Time.

The optical transmittance spectra for FLG and NPG samples are shown in Figure 4.7. Unlike the ITO film, which provides a relatively good optical transmittance mostly for wavelength window from ~450 to ~600 nm, the FLG film maintains good transmittance throughout the entire range of wavelengths of ~400 to ~800 nm studied in this investigation. The unpatterned graphene by itself was found to reduce transmittance at 550 nm by ~15 % in our graphene sample. These results are relatively consistent with previously reported transmittance on stacked CVD-grown graphene layers in which an attenuation coefficient of 2.6 % per layer is extracted by fitting the data to Beer's law. As is demonstrated in Figure 4.7, the transmittance of the NPG with 85.2 nm dia. pores has been found to be quite high, 97.8 % at 550 nm, for 40 sec etching time, which represents almost ×7 times reduced light blockage than that for the pristine graphene counterpart. The transmittance of the NPG with 50 sec etching time was similar with that for the 40 sec sample (Table 4.1). Interestingly, only a slight decrease in transmittance (from 94.2% to 94.0%) was observed by doping of the NPG by HNO_3, while it induced a significant reduction in electrical resistance by an order of magnitude (from 16,670 to 2,200 Ω/sq) for the 40 sec etched sample. In other words, the transmittance was less affected by doping than the electrical properties (Table 4.1). Geometrically, the nanohole array in the 40 sec sample decreases the area of graphene by a factor of 0.689 (see Fig. 4.4(d)), which is based simply on the decrease in the coverage of NPG on the substrate compared to pristine graphene, while the increase in optical transmission is by a factor of x6.86, obtained by comparing the light blockage of the pristine graphene (100 - 84.9% =15.1%) vs. the 40 sec plasma etched NPG hexagonal patterned graphene (100% - 97.8% = 2.2%). Further detailed study is in progress to understand the mechanism behind this observation of surprisingly high optical transmittance in the doped NPG samples. Such a phenomenon points to a possibility of utilizing the properly nanopatterned and doped graphene as promising transparent conducting electrodes for display and other optoelectronic devices operating over a wide range of wavelengths. The starting graphene material utilized in this study was not the highest quality FLG graphene having lowest possible electrical sheet resistance, as compared to previously reported graphene samples, so the absolute value of the sheet resistance of our samples may not seem very low, however, the relative improvements obtained by nano-patterning and chemical doping, with the resultant optical transmission improvement is quite impressive, which is likely to be similarly applicable to other graphene starting material having different electrical sheet resistance values.

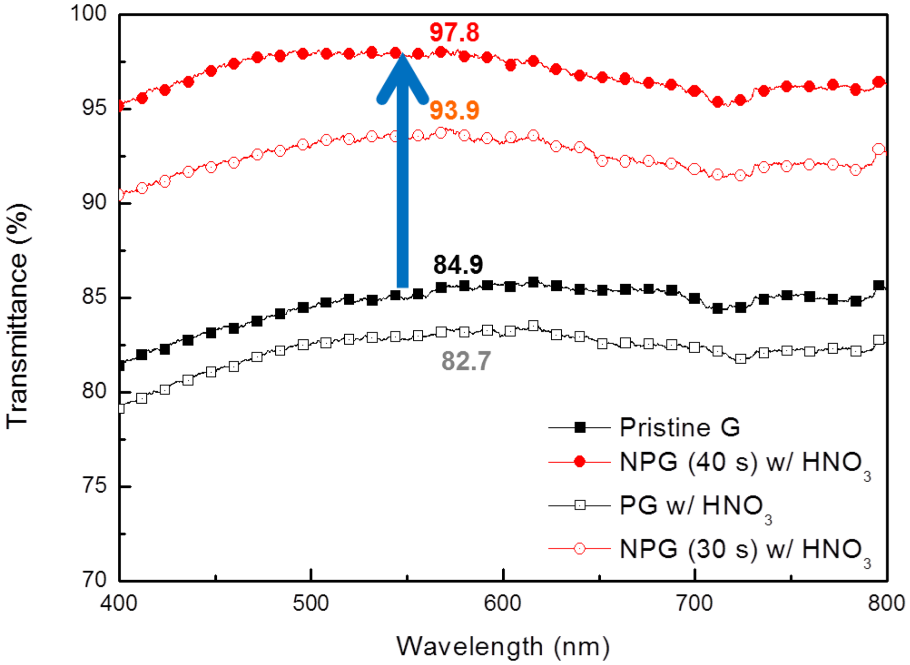

Figure 4.7: UV – vis spectra of pristine and NP graphene films on quartz substrates.

For display type applications of transparent conductors, a proper combination of low electrical sheet resistance and high optical transmittance is essential. De et al.[50] have correlated the figure merit of transparent conductors to the ratio of the DC conductivity to optical conductivity, with high values of the ratio representing the desirable high transmission and low sheet resistance. The optical transmittance of graphene layer can be calculated by

$$T = \left(1 + \frac{Z_0}{2R_S}\frac{\sigma_{OP}}{\sigma_{DC}}\right)^{-2} \tag{4-1}$$

where Z_0 is impedance of free space and R_S is the sheet resistance. [50] The ratio of DC conductivity over optical conductivity (σ_{DC}/σ_{OP}) was calculated for our pristine and nanopatterned graphene as shown in Table 4.1. From the calculated ratio of $_{DC}/_{OP}$, the ratio of 1.8 was obtained for our pristine graphene (without patterning and doping). The (σ_{DC}/σ_{OP}) figure-of-merit ratio for the 40 second plasma etch nanopatterned graphene (NPG) sample which was subsequently acid-doped is particularly high, increased to 10.2 as shown in Table 4.1, which is comparable to the reported values.[15, 20] This value is 5.7 times higher than the ($\sigma_{DC}/\sigma_{OP} = 1.8$) value for pristine graphene, which is also shown in Table 4.1. Because this (σ_{DC}/σ_{OP}) value has a higher correlation with the transmittance change than the sheet resistance, it is important to achieve a high transmittance for the transparent conductor applications. It is noted that the (σ_{DC}/σ_{OP}) ratio for our doped NPG samples is the highest for the 40 sec optimally etched and doped nanostructure as compared to 30 sec and 50 sec plasma etched and doped NPG. The 50 second plasma etch turned out to be an overetch as the hexagonal array nanohole pattern begins to get locally collapsed, which results in undesirable increase of electrical resistance in the NPG sample as shown in Table 4.1. Most of the previously reported data show a trend of increased sheet resistance as the transmittance is increased[15], however our approach demonstrated that reducing the sheet resistance is possible while enhancing optical transmittance. The self-assembly type patterning of graphene using floating membrane of anodized aluminum oxide (AAO) is convenient, versatile and should be of low cost. The dimensions of the AAO holes, spacing and neck width are all controllable, from ~20 nm regime to ~300 nm regime. However, care should be taken in handling and deposition of the fragile AAO membrane in water, minimizing inadvertent membrane folding, wrinkling or tearing. For large-scale manufacturing, some automated or robotic-type handling of the membrane processing, rather than manual handling, would be more desirable.

Table 4.1: Numerical values of optical transmittance T and sheet resistance R_s at 550 nm wavelength for the pristine vs. doped NP graphene (See Figures 4.5 and 4.7), and estimated figure-of-merit values.

Plasma Etch Patterned	**Before doping**			**After HNO_3 doping**			I_D/I_G
	T **(%)**	R_S **(ohm/sq)**	σ_{DC}/σ_{OP}	T **(%)**	R_S **(ohm/sq)**	σ_{DC}/σ_{OP}	
Pristine	**84.9**	**1206**	**1.8**	**82.8**	**859**	**2.2**	**0.26**
30 sec **(54% area open)**	**94.2**	**16670**	**0.4**	**94.0**	**2200**	**2.7**	**0.35**
40 sec **(69% area open)**	**98.6**	**18020**	**0.9**	**97.8**	**1823**	**10.2**	**0.55**
50 sec **(not measured)**	**98.1**	**21030**	**0.6**	**97.3**	**4739**	**3.1**	**0.77**

Based on the trend seen in our results, we can calculate a possible figure-of-merit ratio to be as high as 130 if our starting material graphene were of high quality, which would be far over the industrially desired of figure-of-merit value (σ_{DC}/σ_{OP} =35). For example, if a four-layer stacked high purity graphene (each having 240 Ω/sq sheet resistance[151]) is nano-patterned and doped similarly as our Fig. 4.4(b) and (d) sample, the final sheet resistance of the doped NPG sample is expected to be ~150 Ω/sq sheet resistance and 98% transmittance. Desirable conductive transparent films in general require the sheet resistance to be 10 ~ 100 Ω/sq. It is worthwhile trying to use several layer graphene sheets to get the lower sheet resistance for transparent conductive films. However, there will be a compromise of optical transparency, so to the extent we can live with some loss of transparency in thicker graphene layer, the use of thicker layer can be considered, which will be explored in our follow-up research. Also, we will in the future try to utilize a better starting material of lower sheet resistance graphene (a few hundred ohms/sq as reported by other researchers), which should produce improved final end results.

The present research clearly demonstrates a combined nano-pattering and doping approach to drastically alter the optical and electrical conductivity properties simultaneously toward unusually high optical transmission characteristics, which, if adopted properly for the high-quality graphene, can be a promising route for a new generation of flexible transparent conductors.

4.4 Summary and future work

Successful fabrication of optically highly transparent (~98%) graphene layer has been demonstrated by a proper combination of nano-patterning and chemical doping. This result has important implications for tuning electrical and optical properties of graphene simultaneously, as the two properties were previously controlled in an opposite way- e. g. increasing transmittance by scarifying resistivity. Our ability to control and manipulate the nanoholes in graphene sheets by AAO nano-patterning represents the first step towards graphene transmittance enhancement, and conductivity enhancement by means of defect creation and hydrogenation (or oxygenation). By converting the H- (or O-) termination to HNO_3 termination, the sheet resistance has been reduced to the level of pristine graphene, thus leading to a desirably much more optically transparent conductor having as much as ~seven fold reduced light blockage by graphene material without much loss of electrical conductivity. It is likely that the availability of large number of edges created in the nano-patterned graphene provides ideal sites for chemical dopant attachment, leading to a significant reduction of the R_S while minimally affecting the transmittance. The results indicate that the nano-patterned graphene approach can be a promising route for simultaneously tuning the optical and electrical properties of graphene to make it more light-transmissible and suitable as a new generation of flexible transparent conductors.

Chapter 4, in full, is a reprint of the material as it was accepted in Small written by Duyoung Choi and Sungho Jin. The dissertation author was the primary investigator and author of this work.

CHAPTER 5:
Novel graphene nanostructure network for bio and chemical sensor

5.1 Introduction

For environmental, industrial and military applications detection of toxic gases in ppm levels is important. In this regard gas sensors with high sensitivity, fast response and good reversibility are essential. Carbon based nanostructured materials such as carbon nanotubes (CNT) and graphene are promising for gas sensing owing to their high surface to volume ratio and their electrical conductivity. CNT gas sensors based on conductance change due to adsorbed gas molecules have been explored widely. Many types of CNT based gas sensors such as an isolated CNT [156], CNT networks [157, 158] and functionalized CNTs [159] have been demonstrated. Proposed mechanisms for the CNT gas sensing include charge transfer, and modulation of Schottky barrier at CNT/metal contact [160, 161]. Recently, graphene based gas sensors have been studied by many groups. Single molecule detection was claimed to be possible by using high quality mechanically exfoliated graphene [6]. The ability to detect single molecules is attributed to low noise in graphene as graphene has small number of defects [6]. Yavari used three-dimensional graphene foam network to detect ammonia and nitrogen dioxide [162, 163]. High surface area of graphene foam network enabled high sensitivity for gas sensing. Reduced graphene oxide has also been shown to be a good candidate for gas sensing [162, 163]. Hydrazine hydrate reduced graphene oxide films could detect gas molecules in part-per-billion concentrations [162].

It was also shown that both sensitivity and noise are affected by the level of reduction [162]. In addition, nano-structured graphene materials such as graphene-nanomesh (GNM) and graphene-nanoribbons (GNR) are good candidates for gas sensing due to their highly reactive edges. Paul et al tested GNM and showed that GNM has a sensitivity of 4.32%/ppm for NO_2 and 0.71%/ppm for NH_3 with detection limits of 15 ppb and 160 ppb, respectively [164]. Also, adsorption of gas molecules on GNR was studied and found that GNRs with armchair edges are extremely sensitive to NH_3 molecules and can be used as gas sensors [165, 166].

In this work, we have studied the fabrication of large scale GNR network and its application for ammonia sensing. We take advantage of the large surface area GNRs and their highly reactive edges for gas sensing. Large area GNR network was fabricated by employing Silver nanowires as a mask and subsequent O_2 plasma etching to etch away graphene layers except the regions underneath the Ag NWs. GNR network shows enhanced sensitivity to ammonia gas compared to pristine graphene. Sensitivity is further improved by decorating GNR network with Pd nanoparticles. Pd decorated GNR network sensor shows 65 % sensitivity to 50 ppm of ammonia (NH_3) in nitrogen (N_2) at room temperature as well as good reversibility in air.

5.2 Experimental Details

5.2.1 Palladium decorated graphene-nanoribbon network

Single layer graphene by Chemical Vapor Deposition (CVD) was purchased from ACS Materials. Raman spectroscopy analysis shown in figure 5.1 indicates that graphene is predominantly single layer. Silver nanowires (Ag NWs) with an average diameter of 40 nm and 90 nm, respectively, having 10 um and 25 um lengths were purchased from Blue Nano. Graphene with 1cm^2 area was transferred onto 300 nm thick SiO_2 on p-doped (boron) silicon wafer by conventional PMMA transfer method [16]. There is no restriction in the area of graphene that can be network-patterned by this method.

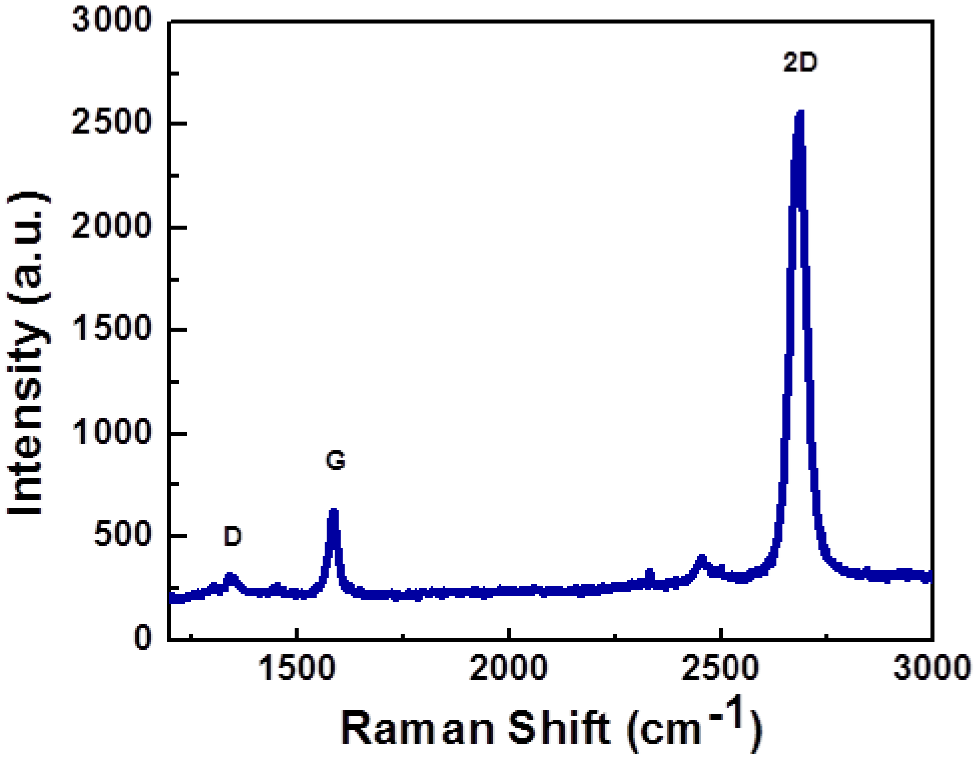

Figure 5.1: Raman data of chemical vapor deposition grown graphene.

Figure 5.2 schematically illustrates the fabrication process of Pd decorated GNR network sensor. Ag NWs in ethanol with a concentration of 10mg/mL was coated on graphene by dip coating method. 10 nm thick Ti adhesion layer and 150 nm thick Au thin film contacts were sputtered on Ag NWs/graphene sample by employing a shadow mask. Channel width and length of the device is 3mm and 10mm respectively. Subsequently, O_2 plasma etching at 25 W and 15°C with a 50 sccm O_2 flow rate was performed in a Trion Reactive Ion Etching system for 30 sec to form the GNR network. RF power was kept as low as possible to avoid any damage to the Ag NWs as they easily break down at higher powers. Ag NWs were removed by etching with 0.5 M ammonium persulfate for 2 hours and cleaned in deionized (DI) water for an hour. Finally, samples were annealed in flowing N_2 at 300°C for 2 hours to remove any residual chemicals and to reduce the contact resistance. In order to decorate GNR network with palladium (Pd) or platinum (Pt) nanoparticles 1 nm thick Pd or Pt was evaporated on GNR network by Temescal Electron Beam Evaporation system.

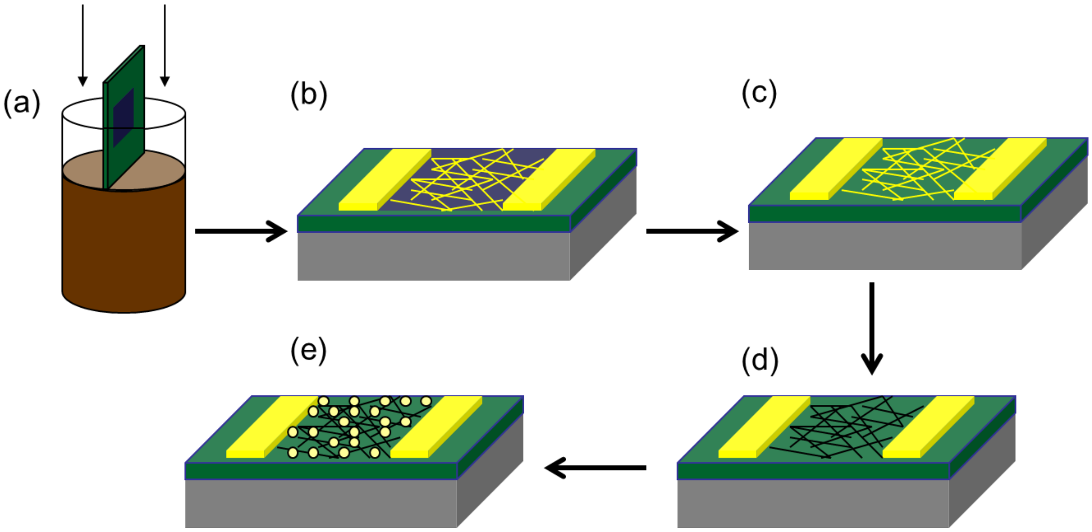

Figure 5.2: Schematic depiction of the fabrication process of Pd-decorated graphene-nanoribbon network. (a) Dip coating of graphene with Ag NWs, (b) Sputter deposition of contacts. (c) O_2 plasma etching of unprotected graphene regions. (d) Removal of Ag NWs by ammonium per sulfate and subsequent cleaning in DI water and annealing at 300C for 2 h. (e) Evaporation of 1nm thick Pd on GNR network.

5.2.2 Gas sensing measurement

Gas sensing measurements were performed with certified 50 ppm NH_3 gas in N_2, which was procured from Praxair. The GNR network gas sensor was mounted on a chip carrier and placed inside a 50 cm^3 glass chamber with a gas inlet and outlet. During the measurements 50 ppm NH_3 in N_2 was flowed with 200 sccm flow rate, which was controlled by a gas flow meter. The gas mixture was purged into chamber with 10 minutes intervals followed by recovery in air for 10 minutes. Resistance was monitored and recorded by a digital multimeter (Keithley, 2100) in combination with software obtained from the company website.

5.3 Results and Discussion

Figure 5.3 show the SEM images of Ag NWs coated graphene, GNR network and Pd-decorated GNR network. Average diameter of Ag NWs is 90 nm and the length is around 25 um. After dip coating, Ag NWs form a continuous network shape structure on graphene (Fig. 5.3a). The coverage density of NWs can be adjusted by changing the density of NWs in ethanol or repeating the dip coating process many times. Shown in of Figure 5.3(b) and 3(c) are the final GNR network pattern with low magnification and high magnification, respectively. After the removal of Ag NWs mask by chemical etching, a network of GNR with an average width of ~90 nm remains. This approach of using straight and rigid metal nanowires placement as a reliable mask to pattern graphene into nanoribbon network, as is demonstrated in this work, is a convenient and fast technique. We were able to produce as small as 40 nm width graphene nanoribbons using this technique (see Figure 5.4). For the gas sensors, we deliberately chose somewhat larger diameter of Ag nanowires (~90 nm) as a mask material for the GNR network because GNRs with smaller width tend to have higher noise since small diameter GNRs are more susceptible to edge defects [141]. Figure 5.3(d) shows GNR network after 1 nm Pd deposition. At this thickness it is seen that Pd is deposited as nanoparticles by decorating GNR network.

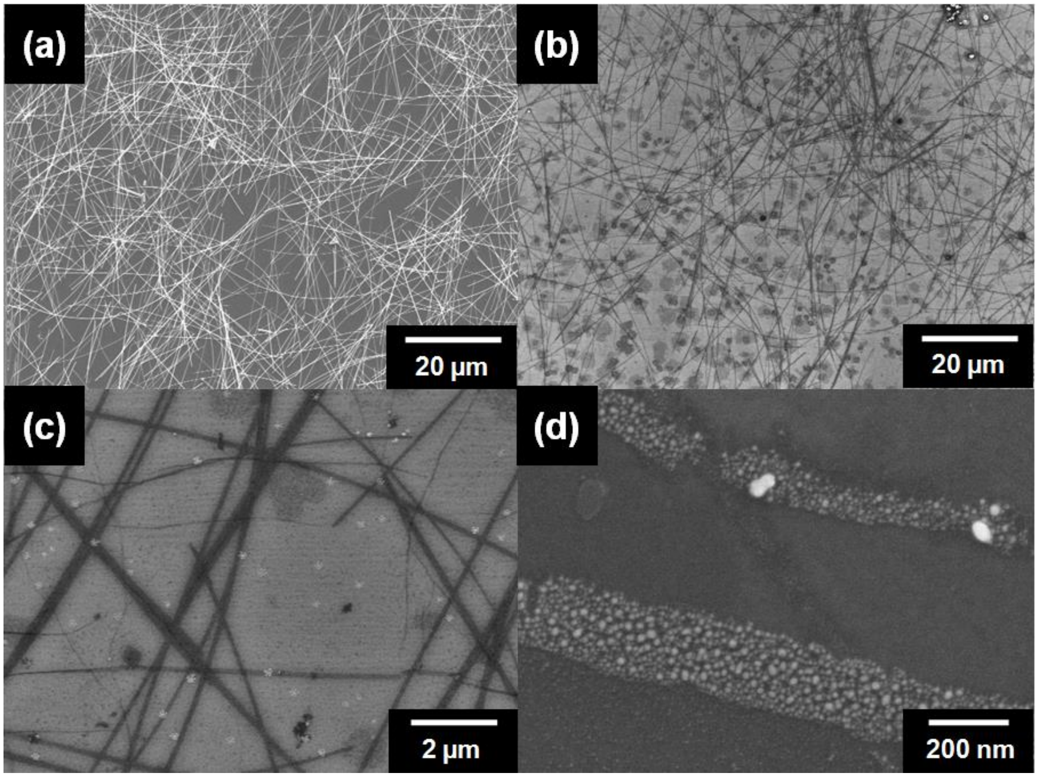

Figure 5.3: Scanning electron microscope images of (a) coated 90 nm Ag NWs (b) GNR network with low magnification (c) GNR network with high magnification (d) Pd decorated GNR network.

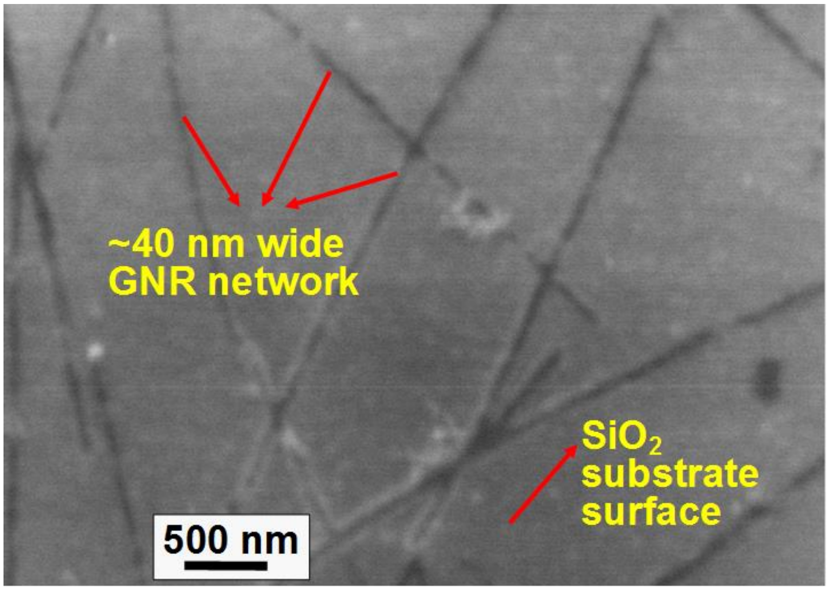

Figure 5.4: ~40 nm width graphene nanoribbon network created by random placement of Ag metal nanowires as a mask. The density of the nanoribbons can be controlled by metal wire concentration in the dip-coating solution.

Figure 5.5 illustrates the comparative gas sensing properties of pristine (unpatterned) graphene layer, GNR network, Pt decorated GNR network and Pd decorated GNR network. The sensitivity of a gas sensor is defined as the relative change in the resistance or conductance. Pd decorated GNR network exhibited the highest sensitivity followed by Pt decorated GNR network, GNR network and pristine graphene. The increase in resistance is attributed to the decrease in the number of charge carriers in graphene. Pristine graphene, GNR network and metal decorated GNR network samples are initially p-doped. As the ammonia molecules adsorb on graphene they transfer electrons into the graphene channel by decreasing the net doping. The GNR network sample exhibited 3 fold improved sensitivity as compared to pristine graphene. The improved sensitivity is most likely due to the highly reactive edges of GNRs. It is known that the edges of GNRs are oxidized during the O_2 plasma etching process [139]. Zanolli investigated the sensing ability of oxygenated defects in carbon nanotubes towards various gases (NO_2, NH_3, CO, and CO_2) and found the presence of oxygenated defects in carbon nanotubes results in an increase in binding energies and charge transfer between carbon nanotubes and gas molecules leading to an increase in sensitivity [167]. The enhanced sensitivity in GNR network is attributed to the existence of oxygenated edge defects in GNRs. The gas sensitivity was further improved upon decoration of GNR network with Pd or Pt nanoparticles. While Pt decorated GNR network showed 45 % sensitivity in 10 minutes Pd decorated GNR network showed 65 % sensitivity towards NH_3. Additionally, metal nanoparticle decorated GNR sensors showed fast response to NH_3. The electrical resistance of Pd decorated GNR network, Pt decorated GNR network, GNR network and pristine graphene increased 29 %, 26 %, 13 % and 4 % in 1 minute, respectively. The high sensitivity of Pd decorated GNR network could be explained by the contribution of highly reactive oxidized edges of GNR as well as Pd nanoparticles. Pd decorated CNTs and graphene have been demonstrated as hydrogen sensors [168-170]. It is known that hydrogen molecules dissociate around Pd nanoparticles and lower the work function of Pd giving rise to more efficient electron transfer into the CNTs or graphene [168-170]. Similarly, NH_3 molecules lower the work function of Pd favoring the electron transfer from Pd into graphene GNR network leading to a decrease in net carrier density. Figure 5.6 illustrates the energy band diagram of Pd/graphene. Initially, Pd has higher work function ($W_m \approx 5.4$ eV) than graphene ($Wg \approx 4.5$ eV) [171]. This leads to electron transfer from GNR network into Pd nanoparticles until equilibrium occurs inducing more holes into GNR network. This is consistent with the resistance measurements of Pd decorated GNR network sample.The resistance of the GNR network itself decreased from 269 KΩ to 162 KΩ upon Pd decoration. That implies that Pd induces more holes into GNR network. As the NH_3 molecules lower the work function of Pd below that of GNR network, electron transfer occurs into the GNR network channel, thus decreasing the net charge carriers and increasing the resistance. All sensor devices in Figure 5.4 showed good repeatability and reversibility in air. After flowing NH_3/N_2 gas mixture for 10 minutes, gas flow was stopped and air was allowed to get into the chamber. All samples exhibited around 50% recovery after 10 minutes and returned to 95% of their initial resistance in an hour.

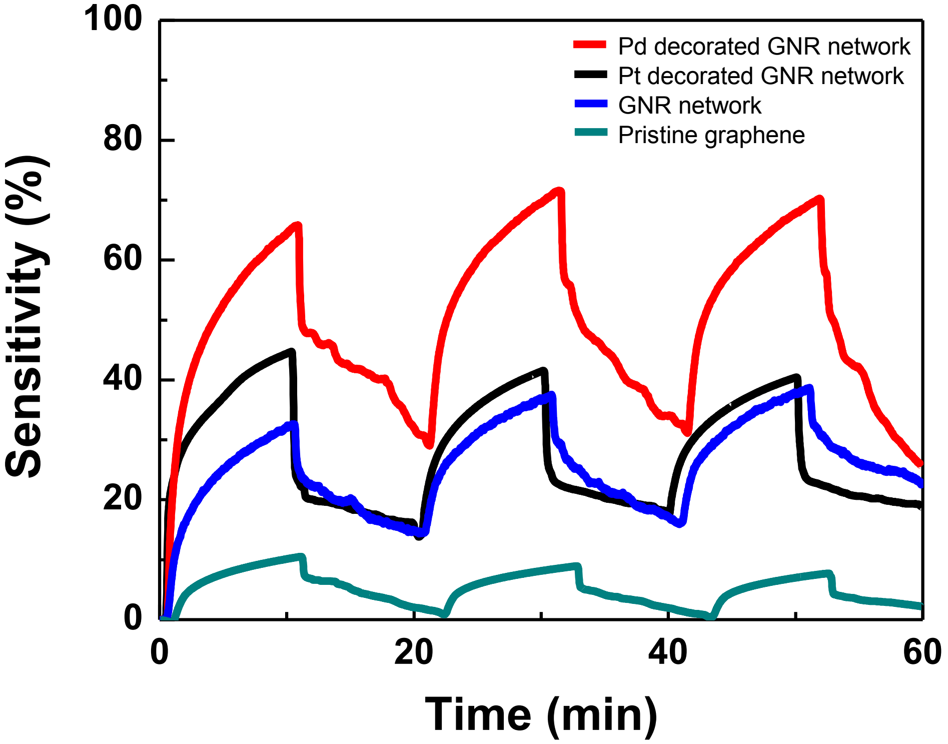

Figure 5.5: 50 ppm NH_3 detection at room temperature of pristine graphene (green solid line), GNR network (blue solid line), Pt decorated GNR network (black solid line), Pd decorated GNR network (red solid line).

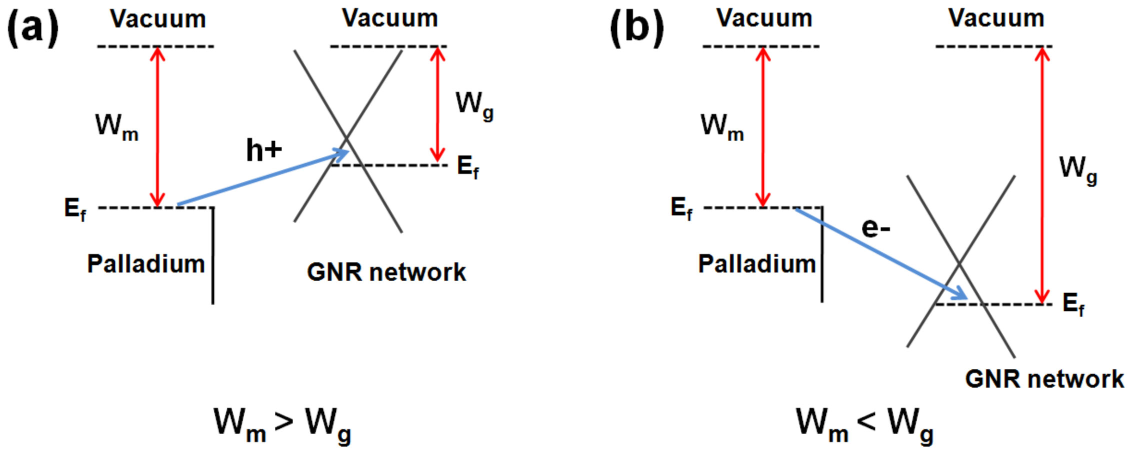

Figure 5.6: Energy band diagram of Pd/ GNR network (a) before NH_3 exposure (b) during NH_3 exposure.

5.4 Summary and future work

In summary, we have demonstrated that a large area graphene-nanoribbon network can be created by a facile method of using randomly positioned metal nanowires as a graphene nano patterning mask. GNR network sensors so prepared exhibited a significant increase (by 3 faold) increase in gas detecting sensitivity to NH_3 gas in compared to pristine graphene. Sensitivity was even further enhanced by decorating GNR network with Pd nanoparticles. The enhanced sensitivity could be explained by the contributions of both highly reactive oxidized edges of GNRs and dissociation of NH_3 molecules near the surface of Pd lowering the work function of Pd below that of GNR network and favoring the electron transfer from Pd into graphene GNR network which results in a decrease in net carrier density.

Chapter 5, in full, is a reprint of the material as it appears in Journal of Nanoscience and Nanotechnology 15(3), 2464-2467 (2015) written by Cihan Kuru, Duyoung Choi, Chulmin Choi, Young Jin Kim, and Sungho Jin. The dissertation author was the primary investigator and author of this work.

CHAPTER 6:

Biodegradably coated magnetic nanocapsules for on-off switchable drug release with reduced leakage

6.1 Introduction

Biomedical utilization of nanomaterial and nanotechnology is an exciting and rapidly advancing field with potentially significant impacts on diagnosis as well as therapeutics for treatment of various human diseases. Such approaches led to the emergence of a new biotech area called “nanomedicine”. Nanoparticle-based [171] or nanocapsule-based [172-175] drug delivery approaches are of particular interest for treatment of various diseases such as cancer since desirably prolonged circulation half-life and reduced nonspecific uptake of the drug can be achieved by active targeting and controlled release. Controlled drug release from nanoparticle drug carriers by external stimuli such as temperature, electric or magnetic fields, light radiation, and changes in pH [176] has attracted much attention for its potential in regulating and maintaining drug delivery of a desired therapeutic concentration range at a disease site. Localized, controlled drug release improves the efficacy of the delivered drugs and minimizes toxic side effects. However, the much needed on-off switchable release using remote, external activation and subsequent de-activation on-demand at any given moment has only recently been fully addressed with substantial progress being made. A technique for switchable drug release based on maneuverable drug-cargo systems without leakage-type loss of drug prior to activation is highly desirable for safe and reliable drug delivery therapeutics.

Hollow spheres have received much attention in recent years for a variety of technical applications including potential controlled-release, drug vehicles. Some of the hollow nanospheres (~50 – 150 nm diameters) have porous shells. Silica coating drastically increases the cargo carrying capability due to its porous structure, whereby the vast functionalization procedures developed for silica allow for further modification of the particle surface. Though the geometry of the capsule shells and porosity of the SiO_2 wall can be adjusted to become minimally permeable to the loaded drug-carrying solutions in the absence of externally magnetic field, it is hard to completely suppress the diffusional leakage of untriggered drug that can cause low efficacy of drug and side effects. While the silica matrixes can also biodegrade to some extent in an aqueous environment, substantial drug leakage can still be expected. Coating of the drug delivery carriers with an organic polymer layer significantly influences the cellular uptake and prevents dispensable loss of drug. Flexible organic surface functionalization thus broadens the enormous potential of the developed new platform for therapeutic applications [177]. Among different polymers, poly (lactide-*co*-glycolide) (PLGA), aliphatic polyester, has been extensively used as an important material of carriers in controlled-release delivery systems for many bioactive molecules due to their low toxicity, good bioavailability and biocompatibility, and FDA approval status [178].

In this work, we successfully demonstrate triggerable nanocapsules which contain magnetic nanoparticles responsive to external radio frequency (RF) magnetic field and PLGA polymer coating on their surface that can reduce the involuntary seepage of drug. This is in contrast to the regular hollow nanospheres for slow passive release of drugs. The new nanocapsule that consists of bio-inert, bio-compatible or bio-degradable material is modified from the nanocapsule previously reported by our lab.

6.2 Experimental details

6.2.1 Chemicals and devices

All reagents were purchased from Sigma-Aldrich, Inc. and Alfa Aesar, and used without further purification unless otherwise stated. The microscopy characterization of synthesized nanoparticles and magnetic nanocapsules were carried out using a transmission electron microscope (FEI Tecnai G2 Sphera with 200 kV accelerated voltage). Various chemical, magnetic and optical measurements were performed using FT-IR (Nicolet 6700 analytical MCT FT-IR Spectrometer), and UV/VIS spectrophotometer (Thermo BioMate3). For the generation of RF magnetic field, Lepel LSS-2.5 RF power supply equipped with a water cooled solenoid was used. Dynamic Light scattering were performed on Nano Zetasizer from Malvern Instruments Ltd. (Malvern Worcestershire, UK).

6.2.2 Synthesis of Fe_3O_4 nanoparticles/PS composite nanospheres

Polystyrene nanospheres with trapped magnetic nanoparticles (as a precursor component for synthesis of silica coated magnetic nanocapsules (SiMNC)) were prepared by combining mini-emulsion/emulsion polymerization and the sol-gel technique according to Kong et al [18]. Briefly, a mixture of 24g $FeCl_3 \cdot 6H_2O$ and 9.82g $FeCl_2 \cdot 4H_2O$ was reacted with 50 ml of ammonium hydroxide under nitrogen gas at 80°C, and then the solution was allowed to react for 1.5 hours after the addition of 3.76 g of oleic acid. The magnetite nanoparticles so fabricated were washed with deionized water until neutral pH and then were transferred in situ into octane.

6.2.3 Nanocapsule formation

Magnetite mini emulsion and styrene mini emulsion were prepared using ultrasound and microporous glass membrane. With these emulsions, mono disperse Fe_3O_4/polystyrene nanospheres were synthesized with 40 mg potassium peroxydisulfate (KPS) at 80^{o}C for 20 h processing. The synthesized Fe_3O_4/polystyrene nanospheres were centrifuged and then were redispersed into 0.5 wt% polyoxyethylene sorbitan monolaurate aqueous solution. The suspension was added into 20 $\mu\ell$ TEOS with 20 ml 2-propanol, and 0.5 ml ammonium hydroxide. The silica encapsulation reaction was performed at room temperature for 48h. The resultant silica magnetic nanospheres were collected and washed by ethanol and water. For fabrication of hollow SiMNCs, the polystyrene (PS) nanosphere material within the silica shell was burnt out at 400-500℃ for 3-6 hours.

6.2.4 Preparation of the PLGA-coated nanocapsules of Cpt-loaded SiMNCs

To prepare a solution containing a hydrophobic anticancer drug, 2.3mg Camptothecin (Cpt) was dissolved in 1.5 ml THF (tetrahydrofuran). In a tube, the Cpt solution was loaded into 4mg of SiMNCs made of hollow nanocapsules containing only Fe_3O_4 magnetic nanoparticles. Insertion of liquid into SiMNCs with several angstrom pores was not easy as the surface tension of the liquid has to be overcome. Therefore a vacuum suction processing was utilized. At room temperature, the SiMNCs samples were placed in a vacuum (~10^{-3} torr) for approximately 20 - 40 minutes to rid nanopores of any trapped air. After drug solution was loaded into the vacuum processed nanocapsules, the drug-containing capsules were washed by de-ionized (DI) water 3-5 times and centrifuged to remove excess drug remaining on the nanocapsule surface. The supernatant was then removed completely. The washing process was repeated until the supernatant was clear. After the supernatant was removed, a supercritical CO_2 drying process was carried out in order to remove the solvent. For supercritical drying, the wet samples were quickly transferred to a critical point drier (EMS-850, Electron Microscopy Sciences, Hatfield, PA). The chamber was pre-cooled to allow samples to be readily filled with liquid CO_2 from a gas cylinder and then heated to just above the critical temperature (>35℃) with subsequent critical pressure (1250 psi) applied. After that, CO_2 gas was vented slowly through a needle valve to avoid the loss of Cpt-loaded SiMNC capsules.

For PLGA coating of the SiMNCs surface without loss of inserted Camptothecin drug (as the solvent tetrahysrofuran (THF) was use for both Cpt dissolution and PLGA dissolution), the following procedure was employed utilizing some excess Cpt in the solvent together with PLGA. In order to prepare saturated PLGA solution in THF, 1.2mg Cpt is added into 1.5 mL of the PLGA solution. After Cpt-loaded SiMNCs were dried, the Cpt-saturated PLGA solution was coated onto the surface of Cpt-loaded SiMNCs. The capsules so processed were dried by supercritical CO_2 dryer system to remove solvent. To prevent the nanocapsules from agglomerating, the Cpt-loaded and PLGA-coated nanocapsules (Cpt-SiMNC-PLGA) were rinsed by THF (pre-saturated with Cpt to minimize undesirable loss of the stored Cpt from inside the capsules by diffusion and washing). In order to remove excess Cpt remaining on the surface of the nanocapsules or in the PLGA coated layer, the PLGA-coated SiMNCs were rinsed by THF.

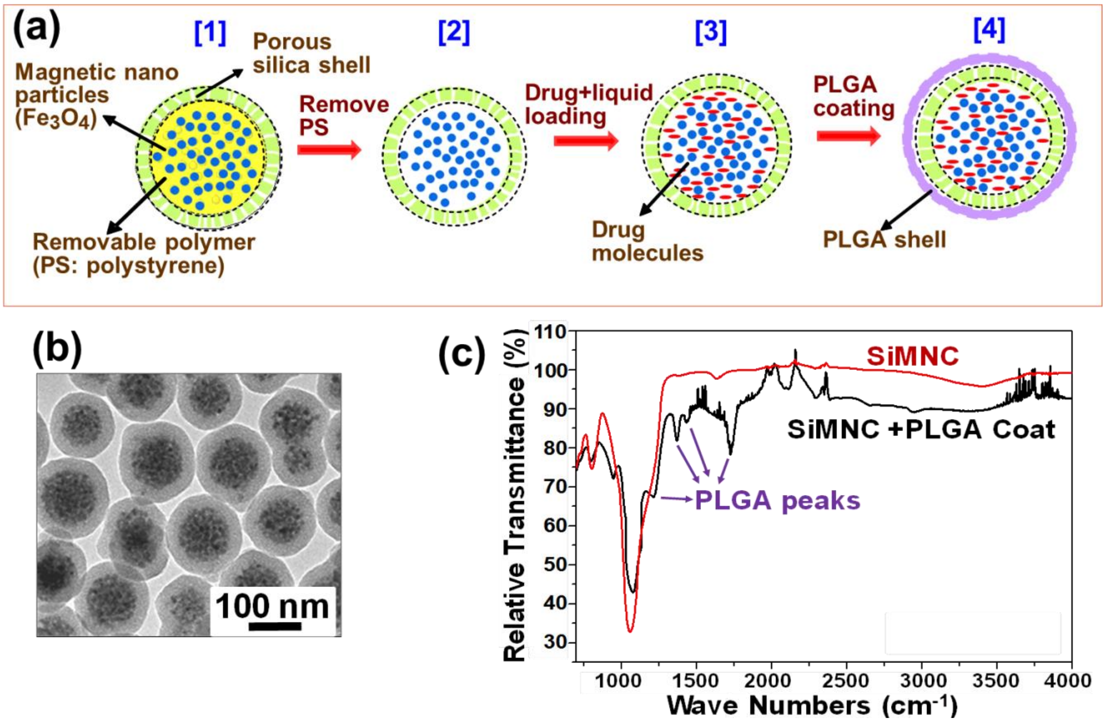

Figure 6.1: Synthesis of hollow SiMNCs as a drug carrier. (a) Schematic illustration showing the preparation steps of drug containing hollow, PLGA-coated SiMNCs with high saturation magnetization. (b) TEM micrograph showing trapped magnetic nanoparticles in SiMNCs, (c) A portion of the FT-IR data showing the presence of PLGA on the nanocapsules.

The sizes of nanoparticles were measured by dynamic light scattering systems (DLS) analysis, using a Zetasizer-ZS apparatus (Malvern, U.K). DLS measures hydrodynamic diameter and charge of particles. We also measured the zeta potential of the nanoparticles at pH 8 to detect the protonation of PLGA coated on the nanocapsule surface. Zeta potential measurements using DLS gives us the charge on these nanocapsules and thus can help elucidate the status of PLGA. The PLGA-coated SiMNCs prepared as described above were quickly washed using THF. A 100 $\mu\ell$

suspension of nanocapsules was dispersed in phosphate buffer with pH 8. The amounts of Cpt drug leakage from the SiMNCs vs. PLGA-coated SiMNCs were measured as a function of time for up to 50 hours using a UV-VIS spectrophotometer, which showed slow diffusional leakage of the drug at different rates.

6.2.5 In vitro remote activated drug release measurement

The PLGA-coated, Cpt-loaded SiMNCs were dispersed in water and subjected to an RF magnetic field. Drug concentration released by RF processing was determined by measuring the absorbance of the fluid using a UV-VIS spectrophotometer at $\lambda = 350$ nm (Biomate3, Thermo Electron, Madison, WI). The assay was calibrated by use of DI water blanks. For actual therapeutic applications, appropriately programmed on-off magnetic field cycles may be utilized, for example, to enable controlled release over extended periods of time with suitably minimized toxic side effects, and also to minimize possible nanocapsule overheating damage. Therefore an on-off cyclic release experiments were conducted. Three replicates per experimental sample for each time point were measured and the average values ± standard error (SE) was graphed to obtain release and on-off cyclic profiles.

For each data point time of activation and inactivation, the emulsion containing 500 $\mu\ell$ water was left still without applied RF field to get the nanocapsules settle to the bottom of the container and then the amount of Cpt released was measured from the solution by standard UV/VIS absorption spectrophometry method. After measuring the released amount of Cpt, the emulsion was exposed to RF field activation (at 100 KHz) for 2 min. After the Cpt supernatants were cleared of floating particles, the Cpt content of the solution was measured using UV/VIS absorption for drug contents dissolved in the solution. After the switch “ON” measurement is done, the solution was left still for 5 min without RF field, and the drug content in the solution was measured by UV/VIS spectrophotometry. The switch “ON-OFF” measurements were taken alternately and the release profile was graphed.

6.3 Results and discussion

We have substantially improved the process by first incorporating ~10 nm Fe_3O_4 nanoparticles into a polystyrene sphere which was then encapsulated in a silica shell, followed by dissolving away or burning away the polymer material present within the capsule, thus creating a hollow capsule configuration yet with magnetic nanoparticles trapped within. The shell material of the hollow capsules was constructed with a known biocompatible material, silica (SiO_2). The details of the capsule synthesis were described in the previous report [174]. Fig. 6.1 shows a schematic illustration of the processes utilized for fabrication of such hollow silica magnetic nanocapsules (SiMNC) with the inside polystyrene removed (Fig. 6.1a-[1]) but retaining the magnetic nanoparticles (Fig. 6.1a-[2]). After preparing SiMNC with trapped magnetic nanoparticles inside, the Camptothecin (Cpt), one of the anticancer drugs chosen for this study, and poly(lactic-*co*-glycolic acid) (PLGA) were loaded into the 100-150 nm diameter hollow capsules, Fig. 6.1a-[3], followed by coating with surface coating of the nanocapsule with PLGA, Fig. 6.1a-[4]. The TEM micrograph showing the trapped magnetic nanoparticles is presented in Fig. 6.1b. The spectra obtained by FTIR for the PLGA-coated SiMNC and uncoated SiMNC are presented in Fig. 6.1c. One can observe, in the spectra, strong bands in the region between 1760 and 1750 cm^{-1}, due to stretch of the carbonyl groups present in PLGA polymer. There are also stretching bands due to asymmetric and symmetric C-C(=O)-O vibrations between 1300 and 1150 cm^{-1}. The bands in these regions are useful in the characterization of esters. These spectra agree with those given in the literature for PLGA copolymers [32]. These FTIR results indicate that the PLGA copolymers have successfully been coated onto the nanocapsule surface. The uncoated Cpt-loaded hollow silica magnetic nanocapsules (Cpt-SiMNCs), and PLGA-coated SiMNC (Cpt-SiMNC-PLGA) were remotely activated by applied RF field for on-demand release.

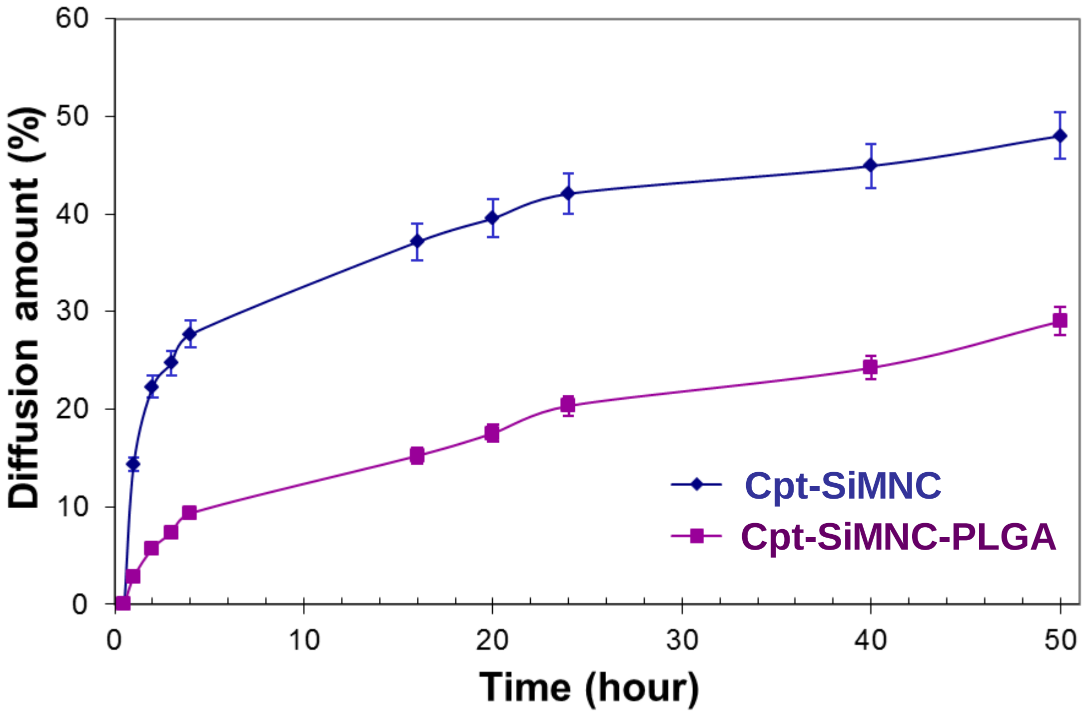

Figure 6.2:The comparison of diffusion rate from Cpt containing SiMNCs vs. PLGA-coated SiMNC (marked as Cpt-SiMNC-PLGA) without applying RF field.

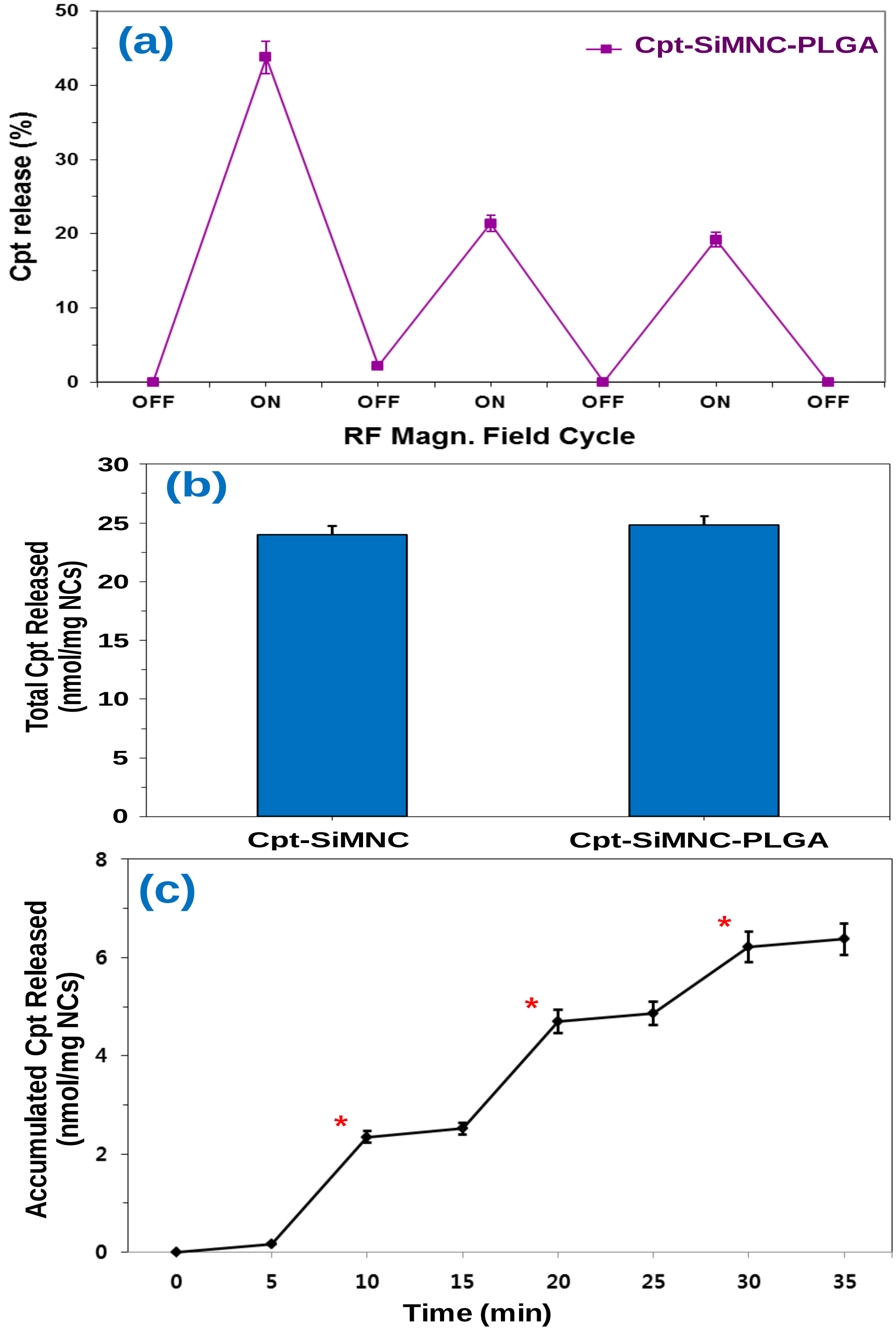

Figure 6.3: On-off switchable release from the PLGA-coated SiMNC nanocapsules (Cpt-SiMNC-PLGA). (**a**) Release of hydrophobic camptothecin by RF magnetic field on-off cycling (switch-on period of 10 s, switch off period of 5 min), (**b**) The comparison of total amounts of Cpt release from hollow SiMNCs vs. PLGA-coated SiMNCs, (**c**) Cumulative amount of Cpt by repeated switchable release (switch-on period of 2 min, switch-off period of 5 min), shown up to 3 cycles.

Shown in Fig. 6.2 is the measured drug release data (diffused out drug) without applying RF field to SiMNCs and PLGA-coated SiMNCs. While the diffusional leakage of the hydrophobic Cpt drug is observed to be relatively slow, the total amount of leakage amounts to be substantial after many hours of time. The leakage rate from the PLGA-coated SiMNC to the PBS solution environment tends to be noticeably less than the case for the uncoated SiMNC. The total amount of drug diffused out after 50 hours was 48% vs. 29% for SiMNC vs. PLGA-coated SiMNC respectively. The uncoated hollow SiMNC capsules allowed diffusing out of much more Cpt as compared to the case of PLGA-coated, surface protected SiMNC. The PLGA coating on silica surface could prevent/minimize the drug from leaking to outside by blocking the nano-sized pores in the silica nanocapsule. Therefore the trapped hydrophobic drugs in the interior of SiMNCs are not permitted to be easily spilled out of the nanocapsule without external stimuli. Depending on the intended delay time to minimize/prevent the leakage of drug molecules from the nanocapsule before drug-release-activation, the thickness and the type of biodegradable coating can be adjusted. For longer intended delay of drug leakage, a thicker PLGA coating may be utilized.

Fig. 6.3a shows the experimental results representing the amount of released drug vs. on-off switch cycles of applied RF magnetic field (at 100 kHz). A dramatic change in the amount of released drug is evident when the remote magnetic field is switched “on” and “off”. The release of the hydrophobic drug to the PBS environment after the initial release tends to slow down as the concentration gradient would be somewhat reduced on successive cycling. The rate of drug release during the “ON” demand of drug release is controllable by the degree and duration of magnetic heating. Cpt was loaded into the hollow capsule vehicle using vacuum loading process and then remotely activated for drug release by applied radio frequency (RF) field. Possible release mechanism for the observed on-off switchable drug release most likely involves the heating of magnetic nanoparticles trapped within the nanocapsules. The remote high-frequency radio frequency (RF) magnetic field, at the frequency used (100 KHz) selectively heats the magnetic nanoparticles in the hollow shell interior to induce a temperature gradient and stimulate accelerated drug release (further details of the discussions on the release mechanism is found in our prior studies). For actual therapeutic applications, appropriately programmed on-off magnetic field cycles may be utilized, for example, to enable controlled release over extended periods of time with suitably minimized toxic side effects, and also to minimize possible nanocapsule overheating damage.

The SiMNCs were negatively charged at pH 8 with a mean zeta potential of -17.3±0.817 mV, as expected for silica surfaces, (Table 6.1). The particle size (SiMNCs) of Z-average was ~200 nm as analyzed by Zetasizer-ZS. The surface PLGA-coated SiMNC yields an overall just slightly negative charge on the nanocapsule surface, and the size of the particle (PLGA-coated capsule) was ~225 nm which is ~10% larger than the size of PLGA-free SiMNC due to the thin coating of PLGA surrounding the nanocapsule surface. If an extended period of delay time to prevent or minimize the leakage of drug molecules from the nanocapsule is needed before drug-release-activation (for example, hours vs. days vs. weeks), the thickness and the type of biodegradable coating can be altered as needed so as to take longer time to dissolve away the biodegradable polymer coating and enable rapid drug release on RF field activation. When the biodegradable PLGA is eventually dissolved away in human body (the rate of which is dependent on the composition of PLGA polymer (as the poly(lactic-co-glycolic acid consists of lactic acid component and glycolic acid component, with a higher content of glycolide units reduces the time for degradation), as well as the thickness/amount of the PLGA coating to be dissolved. The remaining, PLGA-free hollow SiMNC after biodegradation removal of PLGA can release hydrophobic drugs by demonstrated process and mechanism. If the PLGA-coated hollow SiMNC is RF magnetically activated without allowing sufficient time to dissolve away the PLGA, the drug release can still occur as shown in Fig. 6.3. One of the possible reasons may be that the magnetic nanoparticles in capsules heated using RF field also cause some temperature rise of PLGA, thus heating the PLGA material toward the glass transition temperature (T_g) (~40-60℃ depending on the PLGA composition). The heated matrix of PLGA polymer is likely to become somewhat loosened to allow easier passage of drug molecules, and may also cause accelerated degradation/dissolution of PLGA. A more detailed study for understanding of the mechanisms involved in the drug release from the PLGA-coated hollow capsules will be carried out in the future. Considering the total amount of released drug (as shown in Fig. 6.3b), the hollow SiMNC stored similar amount of Cpt per mg of magnetic nanocapsules (NCs) as compared to the case of PLGA-coated SiMNCs indicating that the amount of Cpt in the outside PLGA coating layer was either negligible or very little.

Knowledge of the sign and value of the zeta potential is important since the surface charge governs the stability or state of dispersion. This parameter need to be determined as a function of pH. The extent and the sign of this surface charge depend on the H^+ and OH^- concentrations in the solution. The surface charge appears during immersion as silanol surface sites become hydrated. They can then be ionized, depending on pH [179]. Many authors have reported that the surface charge of silica is strongly negative for a very wide range of pH values [178]. Zeta potentials reported for PLGA based nanoparticles were found to vary from −3.54 mV to −4.04 mV [180]. From the data it is evident that the unexpectedly reduced negative charge density of PLGA-coated SiMNC indicates that the PLGA placed on the outside surface of nanocapsules contribute to the charging of silica surface.

Table 6.1: Comparison of particle size and zeta potential of SiMNC vs. PLGA-coated SiMNC.

	Particle Size (d, nm)	Zeta Potential (mV)
SiMNC	200	-17.3±0.817
PLGA-coated SiMNC	225	-0.379±1.14

In addition to the measurement of the PLGA-coated SiMNC size by dynamic light scattering (DLS) analysis, the Zeta potential surface charge measurements also indicate that SiMNC is coated by PLGA as shown in Table 6.1. A more detailed study for understanding of the mechanisms involved will be carried out in the future.

6.4 Summary and future work

The synthesis, magnetic remote, on-off switchable drug delivery of magnetic nanocapsules, as well as possible prevention from involuntary diffusion by polymer have been investigated in this research. The use of thin biodegradable polymer coating like PLGA on the surface of hollow magnetic nanocapsules can be utilized to reduce or prevent the diffusional leakage of stored drug molecules when the nanocapsules are not activated. The results in this dissertation clearly show a simple but powerful way of targeted drug delivery with incorporated leakage-reducing surface coating, by using remotely activated, drug-loaded magnetic nanocapsules to the desired site without leakage of drug. Our on-off switchable, nanocapsules have the advantages of allowing defined insertion of hydrophobic or hydrophilic anti-cancer drugs, exhibit a powerful magnetic vector, followed by remotely activated, on-demand release of anti-cancer drugs, thus offering a promise of overcoming the well-known problem of limited access of anti-cancer drugs to the desired location in the interior of tumor tissues.

Chapter 6, in full, has been submitted for publication, “Biodegradably Coated Magnetic Nanocapsules for On-Off Switchable Drug Release with Reduced Leakage”, by Duyoung Choi, Seong Deok Kong and Sungho Jin. The dissertation author was the primary investigator and author of this work.

CHAPTER 7: Overall Summary, Conclusions, and Future Work

In this thesis, various aspects of graphene have been discussed including novel preparations, properties and applications of nanopatterned graphene by using self-assembly techniques.

First, the successfully fabricated NPG using a PS-*b*-P4VP polymer and AAO template was never used previously for the graphene patterning. The NPG exhibits homogeneous mesh structures with an average neck width of ~ 19 nm. Electronic characterization of single and few layers NPG FETs were performed at room temperature. The NPG allowed experimental confirmation of the relationship between electrical conductance and bandgap. Electrical characterization of NPG confirmed that the current on/off ratio is inversely proportional with neck width, indicating the formation of an effective gap due to a confinement effect. The availability of such NPG will provide an interesting system for more in-depth fundamental investigation of transport behavior in the highly interconnected, small-width graphene network, and will enable exciting opportunities in sensitive electronic or sensor devices.

Second, graphene has received appreciable attention for its potential applications in flexible conducting film due to its exceptional optical, mechanical and electrical properties. Anodized aluminum oxide nanomask prepared by facile and simple self-assembly technique was utilized to produce an essentially hexagonally nano-patterned graphene (NPG). This result has important implications for tuning electrical and optical properties of graphene simultaneously, as the two properties were previously controlled in an opposite way- e. g. increasing transmittance by scarifying resistivity. Our ability to control and manipulate the nanoholes in graphene sheets by AAO nano-patterning represents the first step towards graphene transmittance enhancement, and conductivity enhancement by means of defect creation and hydrogenation (or oxygenation).

Third, the fabrication of large-scale graphene-nanoribbon (GNR) network and its application for gas sensing are reported. The gas detection sensitivity of the nanoscale GNR network is even further improved by decorating GNR network with palladium (Pd) nanoparticles, which shows a relative resistance response of 65 % to 50 ppm of ammonia (NH_3) in nitrogen (N_2) at room temperature as well as good reversibility in air.

Finally, PLGA-coated nanocapsules allow a switchable drug release on remote RF magnetic field actuation, and are capable of tumor penetration with their powerful magnetic vector. The addition of thin, biodegradable PLGA-polymer-coating on the nanocapsule surface intentionally delays the diffusional leakage of the therapeutic drugs through the nanopores in the wall of the hollow capsules that contain the magnetic nanoparticles and the desired therapeutic drugs. Our on-off switchable, nanocapsules have the advantages of allowing defined insertion of hydrophobic or hydrophilic anti-cancer drugs, exhibit a powerful magnetic vector, followed by remotely activated, on-demand release of anti-cancer drugs, thus offering a promise of overcoming the well-known problem of limited access of anti-cancer drugs to the desired location in the interior of tumor tissues.

REFERENCES

1. Pang, S.P., *Graphene as Transparent Electrode Material for Organic Electronics.* Advanced Materials, 2011. **23**(25): p. 2779-2795.
2. Wang, X., L.J. Zhi, and K. Mullen, *Transparent, conductive graphene electrodes for dye-sensitized solar cells.* Nano Letters, 2008. **8**(1): p. 323-327.
3. Novoselov, K.S., *A roadmap for graphene.* Nature, 2012. **490**(7419): p. 192-200.
4. Novoselov, K.S., *Electric field effect in atomically thin carbon films.* Science, 2004. **306**(5696): p. 666-669.
5. Zhu, Y.W., *Graphene and Graphene Oxide: Synthesis, Properties, and Applications (vol 22, pg 3906, 2010).* Advanced Materials, 2010. **22**(46): p. 5226-5226.
6. Schedin, F., *Detection of individual gas molecules adsorbed on graphene.* Nature Materials, 2007. **6**(9): p. 652-655.
7. Gupta, A., *Raman scattering from high-frequency phonons in supported n-graphene layer films.* Nano Letters, 2006. **6**(12): p. 2667-2673.
8. Gupta, A.K. and M. Gupta, *Synthesis and surface engineering of iron oxide nanoparticles for biomedical applications.* Biomaterials, 2005. **26**(18): p. 3995-4021.
9. Geim, A.K. and K.S. Novoselov, *The rise of graphene.* Nature Materials, 2007. **6**(3): p. 183-191.
10. Mattevi, C., H. Kim, and M. Chhowalla, *A review of chemical vapour deposition of graphene on copper.* Journal of Materials Chemistry, 2011. **21**(10): p. 3324-3334.
11. Li, X., *Graphene films with large domain size by a two-step chemical vapor deposition process.* Nano Letters, 2010. **10**(11): p. 4328-34.
12. Obraztsov, A.N., *Chemical vapor deposition of thin graphite films of nanometer thickness.* Carbon, 2007. **45**(10): p. 2017-2021.
13. Yu, Q.K., *Graphene segregated on Ni surfaces and transferred to insulators.* Applied Physics Letters, 2008. **93**(11).
14. Preobrajenski, A.B., *Controlling graphene corrugation on lattice-mismatched substrates.* Physical Review B, 2008. **78**(7).

15. Li, X.S., *Transfer of Large-Area Graphene Films for High-Performance Transparent Conductive Electrodes.* Nano Letters, 2009. **9**(12): p. 4359-4363.

16. Hwang, J.H., *Epitaxial growth of graphitic carbon on C-face SiC and sapphire by chemical vapor deposition (CVD).* Journal of Crystal Growth, 2010. **312**(21): p. 3219-3224.

17. Rummeli, M.H., *Direct Low-Temperature Nanographene CVD Synthesis over a Dielectric Insulator.* Acs Nano, 2010. **4**(7): p. 4206-4210.

18. Rummeli, M.H., *On the graphitization nature of oxides for the formation of carbon nanostructures.* Chemistry of Materials, 2007. **19**(17): p. 4105-4107.

19. Gautam, M. and A.H. Jayatissa, *Gas sensing properties of graphene synthesized by chemical vapor deposition.* Materials Science & Engineering C-Materials for Biological Applications, 2011. **31**(7): p. 1405-1411.

20. Li, X.S., *Large-Area Synthesis of High-Quality and Uniform Graphene Films on Copper Foils.* Science, 2009. **324**(5932): p. 1312-1314.

21. Chen, Z.H., *Graphene nano-ribbon electronics.* Physica E-Low-Dimensional Systems & Nanostructures, 2007. **40**(2): p. 228-232.

22. Castro Neto, A.H., *The electronic properties of graphene.* Reviews of Modern Physics, 2009. **81**(1): p. 109-162.

23. Wallace, P.R., *The Band Theory of Graphite.* Physical Review, 1947. **71**(9): p. 622-634.

24. Dubois, S.M.M., *Electronic properties and quantum transport in Graphene-based nanostructures.* European Physical Journal B, 2009. **72**(1): p. 1-24.

25. Feldman, B.E., J. Martin, and A. Yacoby, *Broken-symmetry states and divergent resistance in suspended bilayer graphene.* Nature Physics, 2009. **5**(12): p. 889-893.

26. Gonzalez, J.W., *Electronic transport through bilayer graphene flakes.* Physical Review B, 2010. **81**(19).

27. Ohta, T., *Controlling the electronic structure of bilayer graphene.* Science, 2006. **313**(5789): p. 951-954.

28. Casiraghi, C., *Rayleigh imaging of graphene and graphene layers.* Nano Letters, 2007. **7**(9): p. 2711-2717.

29. Murali, R., *Resistivity of Graphene Nanoribbon Interconnects.* Ieee Electron Device Letters, 2009. **30**(6): p. 611-613.

30. Jiao, L.Y., *Narrow graphene nanoribbons from carbon nanotubes.* Nature, 2009. **458**(7240): p. 877-880.

31. Li, X.L., *Chemically derived, ultrasmooth graphene nanoribbon semiconductors.* Science, 2008. **319**(5867): p. 1229-1232.

32. Nakada, K., *Edge state in graphene ribbons: Nanometer size effect and edge shape dependence.* Physical Review B, 1996. **54**(24): p. 17954-17961.

33. Han, M.Y., *Energy band-gap engineering of graphene nanoribbons.* Physical Review Letters, 2007. **98**(20).

34. Cai, J.M., *Atomically precise bottom-up fabrication of graphene nanoribbons.* Nature, 2010. **466**(7305): p. 470-473.

35. Brey, L. and H.A. Fertig, *Electronic states of graphene nanoribbons studied with the Dirac equation.* Physical Review B, 2006. **73**(23).

36. Son, Y.W., M.L. Cohen, and S.G. Louie, *Energy gaps in graphene nanoribbons.* Physical Review Letters, 2006. **97**(21).

37. Lin, Y.M., *Electrical observation of subband formation in graphene nanoribbons.* Physical Review B, 2008. **78**(16).

38. Son, Y.W., M.L. Cohen, and S.G. Louie, *Half-metallic graphene nanoribbons.* Nature, 2006. **444**(7117): p. 347-349.

39. Bae, S., *Roll-to-roll production of 30-inch graphene films for transparent electrodes.* Nature Nanotechnology, 2010. **5**(8): p. 574-578.

40. Balandin, A.A., *Superior thermal conductivity of single-layer graphene.* Nano Letters, 2008. **8**(3): p. 902-907.

41. Kim, K.S., *Large-scale pattern growth of graphene films for stretchable transparent electrodes.* Nature, 2009. **457**(7230): p. 706-710.

42. Novoselov, K.S., *Two-dimensional gas of massless Dirac fermions in graphene.* Nature, 2005. **438**(7065): p. 197-200.

43. Zhang, Y.B., *Experimental observation of the quantum Hall effect and Berry's phase in graphene.* Nature, 2005. **438**(7065): p. 201-204.

44. Blake, P., *Making graphene visible.* Applied Physics Letters, 2007. **91**(6).

45. Nair, R.R., *Fine structure constant defines visual transparency of graphene.* Science, 2008. **320**(5881): p. 1308-1308.

46. Mak, K.F., J. Shan, and T.F. Heinz, *Electronic Structure of Few-Layer Graphene: Experimental Demonstration of Strong Dependence on Stacking Sequence.* Physical Review Letters, 2010. **104**(17).

47. Wang, F., *Gate-variable optical transitions in graphene.* Science, 2008. **320**(5873): p. 206-209.

48. Minami, T., *Transparent conducting oxide semiconductors for transparent electrodes.* Semiconductor Science and Technology, 2005. **20**(4): p. S35-S44.

49. Geng, H.Z., *Effect of acid treatment on carbon nanotube-based flexible transparent conducting films.* Journal of the American Chemical Society, 2007. **129**(25): p. 7758-+.

50. De, S. and J.N. Coleman, *Are There Fundamental Limitations on the Sheet Resistance and Transmittance of Thin Graphene Films?* Acs Nano, 2010. **4**(5): p. 2713-2720.

51. Gong, H., *Interaction between thin-film tin oxide gas sensor and five organic vapors.* Sensors and Actuators B-Chemical, 1999. **54**(3): p. 232-235.

52. Blake, P., *Graphene-based liquid crystal device.* Nano Letters, 2008. **8**(6): p. 1704-1708.

53. Nagashio, K. and A. Toriumi, *Density-of-States Limited Contact Resistance in Graphene Field-Effect Transistors.* Japanese Journal of Applied Physics, 2011. **50**(7).

54. Matyba, P., *Graphene and Mobile Ions: The Key to All-Plastic, Solution-Processed Light-Emitting Devices.* Acs Nano, 2010. **4**(2): p. 637-642.

55. Moser, J., A. Barreiro, and A. Bachtold, *Current-induced cleaning of graphene.* Applied Physics Letters, 2007. **91**(16).

56. Fang, T., *Mobility in semiconducting graphene nanoribbons: Phonon, impurity, and edge roughness scattering.* Physical Review B, 2008. **78**(20).

57. Fang, T., *Carrier statistics and quantum capacitance of graphene sheets and ribbons.* Applied Physics Letters, 2007. **91**(9).

58. Meric, I., *Current saturation in zero-bandgap, topgated graphene field-effect transistors.* Nature Nanotechnology, 2008. **3**(11): p. 654-659.

59. Wang, H., *Compact Virtual-Source Current-Voltage Model for Top- and Back-Gated Graphene Field-Effect Transistors.* Ieee Transactions on Electron Devices, 2011. **58**(5): p. 1523-1533.

60. Hwang, E.H. and S. Das Sarma, *Acoustic phonon scattering limited carrier mobility in two-dimensional extrinsic graphene.* Physical Review B, 2008. **77**(11).

61. Chen, J.H., *Charged-impurity scattering in graphene.* Nature Physics, 2008. **4**(5): p. 377-381.

62. Chen, J.H., *Diffusive charge transport in graphene on SiO2.* Solid State Communications, 2009. **149**(27-28): p. 1080-1086.

63. Kim, S., *Realization of a high mobility dual-gated graphene field-effect transistor with Al2O3 dielectric.* Applied Physics Letters, 2009. **94**(6).

64. Wang, X. and H. Dai, *Etching and narrowing of graphene from the edges.* Nat Chem, 2010. **2**(8): p. 661-5.

65. Barsan, N., D. Koziej, and U. Weimar, *Metal oxide-based gas sensor research: How to?* Sensors and Actuators B-Chemical, 2007. **121**(1): p. 18-35.

66. Comini, E., *Metal oxide nano-crystals for gas sensing.* Analytica Chimica Acta, 2006. **568**(1-2): p. 28-40.

67. Wang, L., *Nanosensor Device for Breath Acetone Detection.* Sensor Letters, 2010. **8**(5): p. 709-712.

68. Chang, Y.C., S.W. Chang, and D.H. Chen, *Magnetic chitosan nanoparticles: Studies on chitosan binding and adsorption of Co(II) ions.* Reactive & Functional Polymers, 2006. **66**(3): p. 335-341.

69. Jain, K.K., *Drug delivery systems - an overview.* Methods Mol Biol, 2008. **437**: p. 1-50.

70. Allen, T.M. and P.R. Cullis, *Drug delivery systems: entering the mainstream.* Science, 2004. **303**(5665): p. 1818-22.

71. Allen, T.M., *Ligand-targeted therapeutics in anticancer therapy.* Nat Rev Cancer, 2002. **2**(10): p. 750-63.

72. Huwyler, J., D. Wu, and W.M. Pardridge, *Brain drug delivery of small molecules using immunoliposomes.* Proc Natl Acad Sci U S A, 1996. **93**(24): p. 14164-9.

73. Chowdhary, R.K., I. Shariff, and D. Dolphin, *Drug release characteristics of lipid based benzoporphyrin derivative.* J Pharm Pharm Sci, 2003. **6**(1): p. 13-9.

74. Maeda, H., *Tumor vascular permeability and the EPR effect in macromolecular therapeutics: a review.* J Control Release, 2000. **65**(1-2): p. 271-84.

75. LaVan, D.A., T. McGuire, and R. Langer, *Small-scale systems for in vivo drug delivery.* Nat Biotechnol, 2003. **21**(10): p. 1184-91.

76. Guo, X. and F.C. Szoka, Jr., *Chemical approaches to triggerable lipid vesicles for drug and gene delivery.* Acc Chem Res, 2003. **36**(5): p. 335-41.

77. Farokhzad, O.C. and R. Langer, *Impact of Nanotechnology on Drug Delivery.* Acs Nano, 2009. **3**(1): p. 16-20.

78. Dave, S.R. and X.H. Gao, *Monodisperse magnetic nanoparticles for biodetection, imaging, and drug delivery: a versatile and evolving technology.* Wiley Interdisciplinary Reviews-Nanomedicine and Nanobiotechnology, 2009. **1**(6): p. 583-609.

79. Krishnan, K.M., *Nanomagnetism and spin electronics: materials, microstructure and novel properties.* Journal of Materials Science, 2006. **41**(3): p. 793-815.

80. Thorek, D.L.J., *Superparamagnetic iron oxide nanoparticle probes for molecular imaging.* Annals of Biomedical Engineering, 2006. **34**(1): p. 23-38.

81. Lopez-Quintela, M.A., *Microemulsion dynamics and reactions in microemulsions.* Current Opinion in Colloid & Interface Science, 2004. **9**(3-4): p. 264-278.

82. Brazel, C.S., *Magnetothermally-responsive nanomaterials: combining magnetic nanostructures and thermally-sensitive polymers for triggered drug release.* Pharm Res, 2009. **26**(3): p. 644-56.

83. Gilchrist, R.K., *Selective inductive heating of lymph nodes.* Ann Surg, 1957. **146**(4): p. 596-606.

84. Liu, T.Y., *Magnetic-sensitive behavior of intelligent ferrogels for controlled release of drug.* Langmuir, 2006. **22**(14): p. 5974-5978.

85. Hu, S.H., *Controlled pulsatile drug release from a ferrogel by a high-frequency magnetic field.* Macromolecules, 2007. **40**(19): p. 6786-6788.

86. Butoescu, N., *Co-encapsulation of dexamethasone 21-acetate and SPIONs into biodegradable polymeric microparticles designed for intra-articular delivery.* Journal of Microencapsulation, 2008. **25**(5): p. 339-350.

87. Dobson, J., *Principles and design of a novel magnetic force mechanical conditioning Bioreactor for tissue engineering, stem cell conditioning, and dynamic in vitro screening.* Ieee Transactions on Nanobioscience, 2006. **5**(3): p. 173-177.

88. Discher, D.E., *Emerging applications of polymersomes in delivery: From molecular dynamics to shrinkage of tumors.* Progress in Polymer Science, 2007. **32**(8-9): p. 838-857.

89. Osulliva.Jp and G.C. Wood, *Morphology and mechanism of formation of porous anodic films on aluminium.* Proceedings of the Royal Society of London Series a-Mathematical and Physical Sciences, 1970. **317**(1531): p. 511-&.

90. Li, F.Y., L. Zhang, and R.M. Metzger, *On the growth of highly ordered pores in anodized aluminum oxide.* Chemistry of Materials, 1998. **10**(9): p. 2470-2480.

91. Jessensky, O., F. Muller, and U. Gosele, *Self-organized formation of hexagonal pore arrays in anodic alumina.* Applied Physics Letters, 1998. **72**(10): p. 1173-1175.

92. Lei, Y., W.P. Cai, and G. Wilde, *Highly ordered nanostructures with tunable size, shape and properties: A new way to surface nano-patterning using ultra-thin alumina masks.* Progress in Materials Science, 2007. **52**(4): p. 465-539.

93. Sun, Z.J. and H.K. Kim, *Growth of ordered, single-domain, alumina nanopore arrays with holographically patterned aluminum films.* Applied Physics Letters, 2002. **81**(18): p. 3458-3460.

94. Masuda, H. and K. Fukuda, *Ordered metal nanohole arrays made by a 2-step replication of honeycomb structures of anodic alumina.* Science, 1995. **268**(5216): p. 1466-1468.

95. Masuda, H., F. Hasegwa, and S. Ono, *Self-ordering of cell arrangement of anodic porous alumina formed in sulfuric acid solution.* Journal of the Electrochemical Society, 1997. **144**(5): p. L127-L130.

96. Masuda, H., K. Yada, and A. Osaka, *Self-ordering of cell configuration of anodic porous alumina with large-size pores in phosphoric acid solution.* Japanese Journal of Applied Physics Part 2-Letters, 1998. **37**(11A): p. L1340-L1342.

97. Li, A.P., *Hexagonal pore arrays with a 50-420 nm interpore distance formed by self-organization in anodic alumina.* Journal of Applied Physics, 1998. **84**(11): p. 6023-6026.

98. Lee, W., K. Nielsch, and U. Gosele, *Self-ordering behavior of nanoporous anodic aluminum oxide (AAO) in malonic acid anodization.* Nanotechnology, 2007. **18**(47).

99. Lee, W., *Fast fabrication of long-range ordered porous alumina membranes by hard anodization.* Nature Materials, 2006. **5**(9): p. 741-747.

100. Lee, W., *Structural engineering of nanoporous anodic aluminium oxide by pulse anodization of aluminium.* Nature Nanotechnology, 2008. **3**(4): p. 234-239.

101. Lee, W., R. Scholz, and U. Gosele, *A continuous process for structurally well-defined Al2O3 nanotubes based on pulse anodization of aluminum.* Nano Letters, 2008. **8**(8): p. 2155-2160.

102. Schwirn, K., *Self-ordered anodic aluminum oxide formed by H2SO4 hard anodization.* Acs Nano, 2008. **2**(2): p. 302-310.

103. Keller, F., M.S. Hunter, and D.L. Robinson, *Structural features of oxide coatings on aluminium.* Journal of the Electrochemical Society, 1953. **100**(9): p. 411-419.

104. Lohrengel, M.M., *Thin anodic oxide layers on aluminum and other valve metals- high-field regime.* Materials Science & Engineering R-Reports, 1993. **11**(6): p. 243-294.

105. Ono, S., *Controlling factor of self-ordering of anodic porous alumina.* Journal of the Electrochemical Society, 2004. **151**(8): p. B473-B478.

106. Shingubara, S., *Self-organization of a porous alumina nanohole array using a sulfuric/oxalic acid mixture as electrolyte.* Electrochemical and Solid State Letters, 2004. **7**(3): p. E15-E17.

107. Nielsch, K., *Self-ordering regimes of porous alumina: The 10% porosity rule.* Nano Letters, 2002. **2**(7): p. 677-680.

108. Jessensky, O., F. Muller, and U. Gosele, *Self-organized formation of hexagonal pore structures in anodic alumina.* Journal of the Electrochemical Society, 1998. **145**(11): p. 3735-3740.

109. Chu, S.Z., *Fabrication of ideally ordered nanoporous alumina films and integrated alumina nanotubule arrays by high-field anodization.* Advanced Materials, 2005. **17**(17): p. 2115-+.

110. Fredrickson, G.H. and F.S. Bates, *Dynamics of block copolymers: Theory and experiment.* Annual Review of Materials Science, 1996. **26**: p. 501-550.

111. Bates, F.S., *Polymer-Polymer Phase-Behavior.* Science, 1991. **251**(4996): p. 898-905.

112. Leibler, L., *Theory Of Microphase Separation In Block Co-Polymers.* Macromolecules, 1980. **13**(6): p. 1602-1617.

113. Fredrickson, G.H. and E. Helfand, *Fluctuation Effects In The Theory Of Microphase Separation In Block Copolymers.* Journal of Chemical Physics, 1987. **87**(1): p. 697-705.

114. Ruiz, R., *Density multiplication and improved lithography by directed block copolymer assembly.* Science, 2008. **321**(5891): p. 936-939.

115. Park, S., *Macroscopic 10-Terabit-per-Square- Inch Arrays from Block Copolymers with Lateral Order.* Science, 2009. **323**(5917): p. 1030-1033.

116. Park, C.H., *Anisotropic behaviours of massless Dirac fermions in graphene under periodic potentials.* Nature Physics, 2008. **4**(3): p. 213-217.

117. Das, S., *Amplifying Charge-Transfer Characteristics of Graphene for Triiodide Reduction in Dye-Sensitized Solar Cells.* Advanced Functional Materials, 2011. **21**(19): p. 3729-3736.

118. Lu, W. and C.M. Lieber, *Nanoelectronics from the bottom up.* Nat Mater, 2007. **6**(11): p. 841-50.

119. Sinitskii, A. and J.M. Tour, *Patterning graphene through the self-assembled templates: toward periodic two-dimensional graphene nanostructures with semiconductor properties.* J Am Chem Soc, 2010. **132**(42): p. 14730-2.

120. Park, M., *Block copolymer lithography: Periodic arrays of similar to 10(11) holes in 1 square centimeter.* Science, 1997. **276**(5317): p. 1401-1404.

121. Liang, X.G., *Formation of Bandgap and Subbands in Graphene Nanomeshes with Sub-10 nm Ribbon Width Fabricated via Nanoimprint Lithography.* Nano Letters, 2010. **10**(7): p. 2454-2460.

122. Kim, M., *Fabrication and Characterization of Large-Area, Semiconducting Nanoperforated Graphene Materials.* Nano Letters, 2010. **10**(4): p. 1125-1131.

123. Harris, M., G. Appel, and H. Ade, *Surface morphology of annealed polystyrene and poly(methyl methacrylate) thin film blends and bilayers.* Macromolecules, 2003. **36**(9): p. 3307-3314.

124. Ton-That, C., A.G. Shard, and R.H. Bradley, *Surface feature size of spin cast PS/PMMA blends.* Polymer, 2002. **43**(18): p. 4973-4977.

125. Rancatore, B.J., *Small Molecule-Guided Thermoresponsive Supramolecular Assemblies.* Macromolecules, 2012. **45**(20): p. 8292-8299.

126. Korhonen, J.T., *Self-Assembly and Hierarchies in Pyridine-Containing Homopolymers and Block Copolymers with Hydrogen-Bonded Cholesteric Side-Chains.* Macromolecules, 2010. **43**(3): p. 1507-1514.

127. Choi, D., *Nanopatterned Graphene Field Effect Transistor Fabricated Using Block Co-polymer Lithography.* Materials Research Letters, 2014. **2**(3): p. 131-139.

128. Ferrari, A.C., *Raman spectroscopy of graphene and graphite: Disorder, electron-phonon coupling, doping and nonadiabatic effects.* Solid State Communications, 2007. **143**(1-2): p. 47-57.

129. Ferrari, A.C., *Raman spectrum of graphene and graphene layers.* Physical Review Letters, 2006. **97**(18).

130. Berger, C., *Electronic confinement and coherence in patterned epitaxial graphene.* Science, 2006. **312**(5777): p. 1191-1196.

131. Wang, Y.Y., *Interference enhancement of Raman signal of graphene.* Applied Physics Letters, 2008. **92**(4).

132. Malard, L.M., *Raman spectroscopy in graphene.* Physics Reports-Review Section of Physics Letters, 2009. **473**(5-6): p. 51-87.

133. Zhang, Y.B., *Direct observation of a widely tunable bandgap in bilayer graphene.* Nature, 2009. **459**(7248): p. 820-823.

134. Cancado, L.G., *Quantifying Defects in Graphene via Raman Spectroscopy at Different Excitation Energies.* Nano Letters, 2011. **11**(8): p. 3190-3196.

135. Luo, Z.Q., *Electronic Structures and Structural Evolution of Hydrogenated Graphene Probed by Raman Spectroscopy.* Journal of Physical Chemistry C, 2011. **115**(5): p. 1422-1427.

136. Ryu, S., *Raman Spectroscopy of Lithographically Patterned Graphene Nanoribbons.* Acs Nano, 2011. **5**(5): p. 4123-4130.

137. Xu, T., *The influence of molecular weight on nanoporous polymer films.* Polymer, 2001. **42**(21): p. 9091-9095.

138. Ozyilmaz, B., *Electronic transport in locally gated graphene nanoconstrictions.* Applied Physics Letters, 2007. **91**(19).

139. Bai, J.W., *Graphene nanomesh.* Nature Nanotechnology, 2010. **5**(3): p. 190-194.

140. Kosynkin, D.V., *Longitudinal unzipping of carbon nanotubes to form graphene nanoribbons.* Nature, 2009. **458**(7240): p. 872-U5.

141. Wang, X.R., *Room-temperature all-semiconducting sub-10-nm graphene nanoribbon field-effect transistors.* Physical Review Letters, 2008. **100**(20).

142. Safron, N.S., *Barrier-Guided Growth of Micro- and Nano-Structured Graphene.* Advanced Materials, 2012. **24**(8): p. 1041-1045.

143. Lin, Y.M. and P. Avouris, *Strong suppression of electrical noise in bilayer graphene nanodevices.* Nano Letters, 2008. **8**(8): p. 2119-2125.

144. Sui, Y. and J. Appenzeller, *Screening and Interlayer Coupling in Multilayer Graphene Field-Effect Transistors.* Nano Letters, 2009. **9**(8): p. 2973-2977.

145. Bai, J.W., X.F. Duan, and Y. Huang, *Rational Fabrication of Graphene Nanoribbons Using a Nanowire Etch Mask.* Nano Letters, 2009. **9**(5): p. 2083-2087.

146. Pedersen, T.G., *Graphene antidot lattices: Designed defects and spin qubits.* Physical Review Letters, 2008. **100**(13).

147. Reina, A., *Large Area, Few-Layer Graphene Films on Arbitrary Substrates by Chemical Vapor Deposition.* Nano Letters, 2009. **9**(1): p. 30-35.

148. Li, X.S., *Graphene Films with Large Domain Size by a Two-Step Chemical Vapor Deposition Process.* Nano Letters, 2010. **10**(11): p. 4328-4334.

149. Betti, A., G. Fiori, and G. Iannaccone, *Atomistic Investigation of Low-Field Mobility in Graphene Nanoribbons.* Ieee Transactions on Electron Devices, 2011. **58**(9): p. 2824-2830.

150. De, S., *Silver Nanowire Networks as Flexible, Transparent, Conducting Films: Extremely High DC to Optical Conductivity Ratios.* Acs Nano, 2009. **3**(7): p. 1767-1774.

151. Gunes, F., *Layer-by-Layer Doping of Few-Layer Graphene Film.* ACS Nano, 2010. **4**(8): p. 4595-4600.

152. Liu, J.W., *Doped graphene nanohole arrays for flexible transparent conductors.* Applied Physics Letters, 2011. **99**(2).

153. Zeng, Z.Y., *Fabrication of Graphene Nanomesh by Using an Anodic Aluminum Oxide Membrane as a Template.* Advanced Materials, 2012. **24**(30): p. 4138-4142.

154. Rafiee, J., *Wetting transparency of graphene.* Nature Materials, 2012. **11**(3): p. 217-222.

155. Wang, X.R., *N-Doping of Graphene Through Electrothermal Reactions with Ammonia.* Science, 2009. **324**(5928): p. 768-771.

156. Kong, J., *Nanotube molecular wires as chemical sensors.* Science, 2000. **287**(5453): p. 622-625.

157. Cantalini, C., *NO2 gas sensitivity of carbon nanotubes obtained by plasma enhanced chemical vapor deposition.* Sensors and Actuators B-Chemical, 2003. **93**(1-3): p. 333-337.

158. Li, J., *Carbon nanotube sensors for gas and organic vapor detection.* Nano Letters, 2003. **3**(7): p. 929-933.

159. Zhang, T., *Electrochemically functionalized single-walled carbon nanotube gas sensor.* Electroanalysis, 2006. **18**(12): p. 1153-1158.

160. Bradley, K., *Charge transfer from ammonia physisorbed on nanotubes.* Physical Review Letters, 2003. **91**(21).

161. Peng, N., *Sensing Mechanisms for Carbon Nanotube Based NH3 Gas Detection.* Nano Letters, 2009. **9**(4): p. 1626-1630.

162. Lu, G.H., *Toward Practical Gas Sensing with Highly Reduced Graphene Oxide: A New Signal Processing Method To Circumvent Run-to-Run and Device-to-Device Variations.* Acs Nano, 2011. **5**(2): p. 1154-1164.

163. Yavari, F., *High Sensitivity Gas Detection Using a Macroscopic Three-Dimensional Graphene Foam Network.* Scientific Reports, 2011. **1**.

164. Lu, G.H., L.E. Ocola, and J.H. Chen, *Reduced graphene oxide for room-temperature gas sensors.* Nanotechnology, 2009. **20**(44).

165. Huang, B., *Adsorption of gas molecules on graphene nanoribbons and its implication for nanoscale molecule sensor.* Journal of Physical Chemistry C, 2008. **112**(35): p. 13442-13446.

166. Paul, R.K., *Graphene Nanomesh As Highly Sensitive Chemiresistor Gas Sensor.* Analytical Chemistry, 2012. **84**(19): p. 8171-8178.

167. Zanolli, Z. and J.C. Charlier, *Defective carbon nanotubes for single-molecule sensing.* Physical Review B, 2009. **80**(15).

168. Johnson, J.L., *Hydrogen Sensing Using Pd-Functionalized Multi-Layer Graphene Nanoribbon Networks.* Advanced Materials, 2010. **22**(43): p. 4877-+.

169. Kumar, M.K. and S. Ramaprabhu, *Nanostructured Pt functionlized multiwalled carbon nanotube based hydrogen sensor.* Journal of Physical Chemistry B, 2006. **110**(23): p. 11291-11298.

170. Mubeen, S., *Palladium nanoparticles decorated single-walled carbon nanotube hydrogen sensor.* Journal of Physical Chemistry C, 2007. **111**(17): p. 6321-6327.

171. Giovannetti, G., *Doping graphene with metal contacts.* Physical Review Letters, 2008. **101**(2).

172. Kong, S.D., *Magnetic targeting of nanoparticles across the intact blood-brain barrier.* Journal of Controlled Release, 2012. **164**(1): p. 49-57.

173. Kong, S.D., *Magnetic field activated lipid-polymer hybrid nanoparticles for stimuli-responsive drug release.* Acta Biomaterialia, 2013. **9**(3): p. 5447-5452.

174. Kong, S.D., *Magnetically Vectored Nanocapsules for Tumor Penetration and Remotely Switchable On-Demand Drug Release.* Nano Letters, 2010. **10**(12): p. 5088-5092.

175. Kong, S.D., *Externally triggered on-demand drug release and deep tumor penetration.* Journal of Vacuum Science & Technology B, 2012. **30**(2).

176. Beduneau, A., P. Saulnier, and J.P. Benoit, *Active targeting of brain tumors using nanocarriers.* Biomaterials, 2007. **28**(33): p. 4947-4967.

177. Loo, S.C.J., C.P. Ooi, and Y.C.F. Boey, *Influence of electron-beam radiation on the hydrolytic degradation behaviour of poly(lactide-co-glycolide) (PLGA).* Biomaterials, 2005. **26**(18): p. 3809-3817.

178. Bolt, G.H., *Determination of the Charge Density of Silica Sols.* Journal of Physical Chemistry, 1957. **61**(9): p. 1166-1169.

179. M. Bizi, *Stability and flocculation of nanosilica by conventional organic polymer*, Natural Science, 2012. **4**: p. 372-385.

180. C. Gómez-Gaetea, N. Tsapisa, M. Besnarda, A. Bochota, and E. Fattal, *Encapsulation of dexamethasone into biodegradable polymeric nanoparticles*, Int’l. J. Pharm., 2007. **331**: p. 153-159.